

การวิเคราะห์การแจกแจงกระแสของเครื่องปฏิกรณ์ซูบไลหะและ
แบบจำลองเชิงคณิตศาสตร์ของการซูบไลหะผสมสังกะสี-นิกเกิล



นางสาวมานิดา ธีระธนานนท์

สถาบันวิทยบริการ

วิทยานิพนธ์นี้เป็นส่วนหนึ่งของการศึกษาตามหลักสูตรปริญญาวิทยาศาสตรดุษฎีบัณฑิต

สาขาวิชาเคมีเทคนิค ภาควิชาเคมีเทคนิค

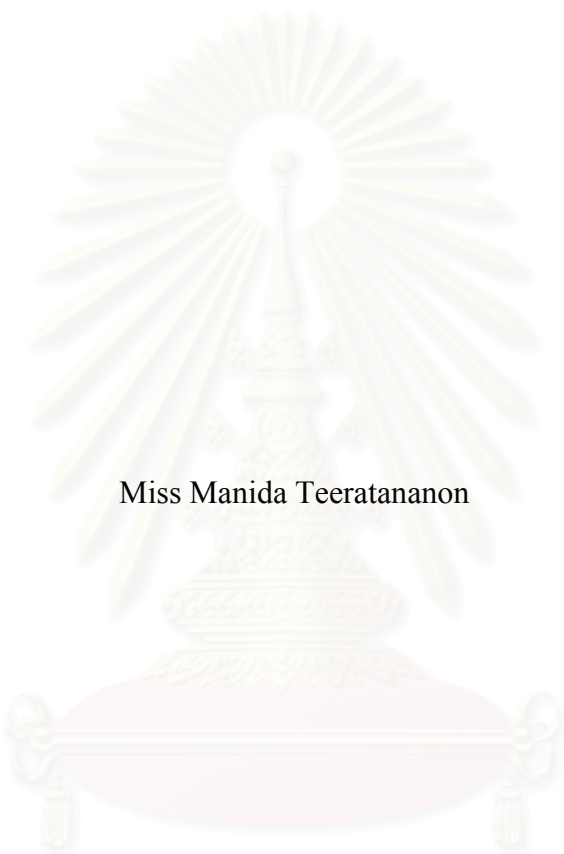
คณะวิทยาศาสตร์ จุฬาลงกรณ์มหาวิทยาลัย

ปีการศึกษา 2547

ISBN 974 – 17-5940-1

ลิขสิทธิ์ของจุฬาลงกรณ์มหาวิทยาลัย

CURRENT DISTRIBUTION ANALYSIS OF ELECTROPLATING REACTORS
AND MATHEMATICAL MODELING OF THE ELECTROPLATED
ZINC-NICKEL ALLOY



Miss Manida Teeratananon

สถาบันวิทยบริการ
จุฬาลงกรณ์มหาวิทยาลัย

A Dissertation Submitted in Partial Fulfillment of the Requirements
for the Degree of Doctor of Philosophy in Chemical Technology
Department of Chemical Technology
Faculty of Science
Chulalongkorn University
Academic Year 2004
ISBN 974 – 17-5940-1

Thesis Title CURRENT DISTRIBUTION ANALYSIS OF ELECTROPLATING
REACTORS AND MATHEMATICAL MODELING OF THE
ELECTROPLATED ZINC-NICKEL ALLOY
By Manida Teeratananon
Filed of study Chemical Technology
Thesis Advisor Professor Somsak Damronglerd
Thesis Co-advisor Professor Patrick Duverneuil
Thesis Co-advisor Assistant Professor Kejvalee Pruksathorn

Accepted by the Faculty of Science, Chulalongkorn University in Partial Fulfillment of
the Requirements for the Doctor's Degree

.....Dean of Faculty of Science
(Professor)

THESIS COMMITTEE

..... Chairman
(Professor Pattarapan Prasassarakich)

..... Thesis Advisor
(Professor Somsak Damronglerd)

..... Thesis Co-advisor
(Professor Patrick Duverneuil)

..... Thesis Co-advisor
(Assistant Professor Kejvalee Pruksathorn)

..... Member
(Dr. Thawach Chatchupong)

..... Member
(Dr. Jean-Pierre Bonino)

..... Member
(Dr. Hugues Vergnes)

มานิดา ชีระธนานนท์ : การวิเคราะห์การแจกแจงกระแสของเครื่องปฏิกรณ์ชุบโลหะและแบบจำลองเชิงคณิตศาสตร์ของการชุบโลหะผสมสังกะสี-นิกเกิล (CURRENT DISTRIBUTION ANALYSIS OF ELECTROPLATING REACTORS AND MATHEMATICAL MODELING OF THE ELECTROPLATED ZINC-NICKEL ALLOY) อ. ที่ปรึกษา : ศ.ดร.สมศักดิ์ ดำรงค์เลิศ, อ.ที่ปรึกษาร่วม : ศ.ดร. Patrick Duverneuil, ผศ.ดร. เก้ววลี พุกษาทร, 179 หน้า. ISBN 974-17-5940-1.

งานวิจัยนี้เป็นการศึกษาในระดับต่างๆของเซลล์ไฟฟ้าเคมีที่นำมาประยุกต์ใช้ในกระบวนการพอกพูนด้วยกระแสไฟฟ้า ในส่วนแรกของงานวิจัยเป็นแบบจำลองเชิงคณิตศาสตร์แบบมหัพภาคของเครื่องปฏิกรณ์แบบกะที่ใช้ในการบำบัดน้ำเสียที่มีทองแดงปนเปื้อน ส่วนที่สองเป็นการทดลองเรื่องการแจกแจงกระแสของเครื่องปฏิกรณ์แบบ Rotary Hull Cell และเครื่องปฏิกรณ์แบบ Modified Mohler Cell ส่วนที่สามเป็นการพัฒนาหากลไกของปฏิกิริยาการชุบโลหะผสมสังกะสี-นิกเกิล เพื่อสร้างแบบจำลองเชิงคณิตศาสตร์ในการอธิบายกลไกดังกล่าว งานวิจัยนี้ก่อให้เกิดเครื่องมือที่มีศักยภาพและเป็นประโยชน์เฉพาะด้านสำหรับพัฒนากระบวนการพอกพูนด้วยกระแสไฟฟ้า โดยเฉพาะอย่างยิ่งในการนำมาประยุกต์ใช้ในการออกแบบและควบคุมกระบวนการผลิต

สถาบันวิทยบริการ จุฬาลงกรณ์มหาวิทยาลัย

ภาควิชาเคมีเทคนิค
สาขาวิชาเคมีเทคนิค
ปีการศึกษา 2547

ลายมือชื่อนิติ.....
ลายมือชื่ออาจารย์ที่ปรึกษา.....
ลายมือชื่ออาจารย์ที่ปรึกษาร่วม.....
ลายมือชื่ออาจารย์ที่ปรึกษาร่วม.....

4373829423 : MAJOR CHEMICAL TECHNOLOGY

KEY WORD: ZINC-NICKEL/ MATHEMATICAL MODEL/ ELECTROPLATING TEST CELL/
ANOMALOUS DEPOSITION / ELECTRODEPOSITION

MANIDA TEERATANANON: CURRENT DISTRIBUTION ANALYSIS OF
ELECTROPLATING REACTORS AND MATHEMATICAL MODELING OF THE
ELECTROPLATED ZINC-NICKEL ALLOY. THESIS ADVISORS : PROF. SOMSAK
DAMRONGLERD, PROF. PATRICK DUVERNEUIL, ASST PROF. KEJVALEE
PRUKSATHORN 179 pp. ISBN 974-17-5940-1.

This work is devoted to a multi-scale study of the electrochemical cells applied in the electrodeposition process. The first part concerns with macroscopic model of a batch reactor used for copper depollution. The second part relates to the experimental study of current distributions in a rotary Hull cell and in a modified Mohler cell. The third part deals with the development of a reaction path mechanism relating to the zinc-nickel alloy codeposition resulting in the model of this operation. This work led to a set of tools particularly useful and powerful for the development of a new electrodeposition plant, especially applied for the design and the process control more than the management of the baths.



Department CHEMICAL TECHNOLOGY

Field of study CHEMICAL TECHNOLOGY

Academic year 2004

Student's signature.....

Advisor's signature.....

Co-advisor's signature.....

Co-advisor's signature.....

CONTENTS

	Page
ABSTRACT (Thai)	iv
ABSTRACT (English)	v
ACKNOWLEDGMENTS	vi
CONTENTS	vii
LIST OF TABLES	xiv
LIST OF FIGURES	xvi
NOMENCLATURES	xxiii
GENERAL INTRODUCTION	xxviii
 PART 1 : MACROSCOPIC MODEL	
Introduction.....	1
 CHAPTER I : Bibliography	
1.1 Summary of Electrochemical Theory.....	2
1.1.1 The Nature of Electrode Reactions.....	2
1.1.2 Electron Transfer.....	3
1.1.2a The Situation at Equilibrium.....	3
1.1.2b Departure from Equilibrium.....	5
(Activation Polarization)	
1.1.3 Mass Transfer.....	8
1.1.3a Steady-State Mass Transfer.....	9
1.1.3b Non Steady-State Mass Transfer.....	12
1.1.4 Concentration Evolution versus Time.....	14
1.1.4a Charge Transfer Limiting Step.....	14
1.1.4b Mass Transfer Limiting Step.....	15
1.2 Macroscopic Model.....	15
1.2.1 Kinetic and Mass Transport in the	
Electrochemical Reactor.....	18
1.2.2 Mass Balance on an Electrochemical Reactor.....	20
1.2.2a Simple Batch Reactor.....	20
1.2.2b Plug Flow Reactor.....	21
1.2.2c Continuous Stirred Tank Reactor.....	23
1.3 Conclusion.....	24

CONTENTS

Page

CHAPTER II : Analyzing Kinetics and Mass Transport on an Electrochemical Batch Reactor

2.1	Introduction.....	25
2.2	Experiment.....	25
2.3	Results and Discussions.....	26
2.3.1	Experimental Results.....	26
2.3.1a	The Effect of Copper Concentration and Applied Current Densities.....	26
2.3.1b	The Effect of Cathodic Potential.....	29
2.3.1c	The Effect of Stirring Rate on Copper Deposition Rate.....	30
2.3.1d	Conclusion.....	31
2.3.2	Macroscopic Model.....	32
2.3.2a	Determination of the Faradaic Current Densities versus Time.....	33
2.3.2b	Determination of the Mass Transfer Coefficient.....	33
2.3.2c	Comparison of Experimental Data and Theoretical Results from the Model.....	34
2.3.2d	Conclusion.....	35
	Conclusion.....	36

สถาบันวิทยบริการ
จุฬาลงกรณ์มหาวิทยาลัย

CONTENTS

Page

PART 2 : ANALYSIS OF THE CURRENT DISTRIBUTION IN DIFFERENT ELECTROPLATING REACTORS

Introduction.....	37
CHAPTER I: Bibliography	
1.1 Mass Transport and Current Distribution.....	38
1.2 Cells with Controlled Non-Uniform Current Distribution.....	41
1.3 Review of Electroplating Test Cell.....	42
1.3.1 Hull Cell.....	42
1.3.2 Hydrodynamically Controlled Hull Cell (HCHC).....	44
1.3.3 The Lu Cell.....	45
1.3.4 Hydrodynamic Electroplating Test Cell (HETC).....	46
1.3.5 Rotating Cylinder Hull Cell (RCH).....	48
1.3.6 Mohler Cell.....	49
1.4 Conclusion.....	49
CHAPTER II: Experimental Investigation of the Current Distribution in Mohler Cell and Rotating Cylinder Hull Cell	
2.1 Introduction.....	50
2.2 Experiment.....	50
2.2.1 Original Mohler Cell.....	50
2.2.2 Modified Mohler Cell.....	52
2.2.3 Determination of the Local Current Density.....	53
2.3 Results and Discussions.....	55
2.3.1 Current Distributions in the Mohler Cell.....	55
2.3.2 Current Distributions in Rotating Cylinder Hull Cell.....	58
2.3.2a Experimental Results.....	58
2.3.2b Distribution of Current in RCH.....	60
2.3.3c Copper Plating involving a Mass Transport Limited Step.....	61

CONTENTS

	Page
2.4 Conclusion.....	62
Conclusion.....	63

PART 3 : MICROSCOPIC MODEL

Introduction.....	64
-------------------	----

CHAPTER I: Bibliography

1.1 Theoretical Aspect of Alloy Plating.....	66
1.1.1 Definition of Alloy.....	66
1.1.2 Plating Variable.....	66
1.1.3 Alloy System Classification.....	67
1.1.4 Mixed Electrodes.....	67
1.1.5 Variation of Alloy Compositions with Potential : Kinetic and Thermodynamic Aspects.....	69
1.1.6 Experimental Considerations : Determination of Partial Current Densities.....	70
1.2 State of Art on Experimental Investigation of Zn-Ni Alloy Deposition.....	71
1.2.1 Zn-Ni Alloy Deposition from Acid and Alkaline Bath.....	71
1.2.1a Operating Conditions.....	71
1.2.1b The Uniform Thickness Distribution.....	73
1.2.1c Percent of Nickel Deposition relating with Corrosion Protection.....	73
1.2.1d Effect of Current Density.....	74
1.2.2 Normal and Anomalous Codeposition of Zn-Ni Alloy Deposition.....	74
1.2.2a Galvanostatic Electrodeposition.....	75
1.2.2b Potentiostatic Electrodeposition.....	78
1.2.3 Dependence of Zn-Ni Alloy Deposition with Time.....	82
1.2.4 Conclusion – Experimental Investigation of Zn-Ni Alloy.....	84

CONTENTS

	Page
1.3	Mathematical Modeling Investigation of Zn-Ni Alloy Deposition.....85
1.3.1	Mechanism involving Hydroxide Species.....85
1.3.1a	Hydroxide Suppression Mechanism.....85
1.3.1b	The pH Dependent Competitive Adsorption of Monohydroxide Species, MOH^+87
1.3.2	Property Interfaces Models.....89
1.3.2a	Underpotential Deposition.....89
1.3.2b	The Competitive Adsorption of Reaction Intermediate.....89
1.3.2c	An Adsorbed Mixed Reaction Intermediate containing the Two Codepositing Species in Partly Reduced Form.....92
1.3.3	Conclusion – Mathematical Model Investigation of Zn-Ni Alloy.....95
1.4	Conclusion.....95
CHAPTER II: Experimental Investigation of Zn-Ni Alloy Deposition	
2.1	Introduction.....97
2.2	Experiment.....98
2.2.1	Determination of the Metal Content of the Layer.....100
2.2.1a	Alloy Composition.....100
2.2.1b	Single Metal Composition.....100
2.2.2	Determination of the Minimum Operating Time for Alloy Deposition.....100
2.3	Results and Discussions.....101
2.3.1	Changing Deposit layer Composition in Zn-Ni Alloy with varying Time.....101
2.3.1a	Applied Potential at -1.2 V/SCE.....102
2.3.1b	Applied Potential at -1.5 V/SCE.....103

CONTENTS

	Page
2.3.2 Elemental Deposition.....	104
2.3.3a Hydrogen Evolution	
on Nickel Substrate and Zinc Substrates.....	106
2.3.3b Nickel Deposition	
on Nickel Substrate and Zinc Substrates.....	106
2.3.3c Zinc Deposition	
on Nickel Substrate and Zinc Substrates.....	107
2.3.3 Alloy Deposition.....	109
2.3.4 Mechanism of Normal and Anomalous Deposition	
in Zn-Ni Alloy.....	112
2.4 Conclusion.....	113

CHAPTER III : Mathematical Modelling of Zn-Ni Alloy Deposition

3.1 Substrate Effect Model.....	115
3.1.1 Introduction.....	115
3.1.2 Model Assumption.....	115
3.1.3 Theoretical Model	117
3.1.3.1 General Mechanism of the Electrode Reaction.....	117
3.1.3.2 Mass Transfer Effect.....	119
3.1.3.3 Electrochemical Kinetic.....	120
3.1.4 Elemental Simulation.....	123
3.1.4.1 Nickel Deposition on Nickel Substrate.....	123
3.1.4.2 Zinc Deposition on Zinc Substrate.....	128
3.1.4.3 Nickel Deposition on Zinc Substrate.....	132
3.1.4.4 Zinc Deposition on Nickel Substrate.....	136
3.1.5 Results of the Global Model.....	140
3.1.5.1 Comparison between Experimental Results	
and Theoretical Results.....	140
3.1.5.1a With Previously Determined Kinetic	
Parameters from Elemental Deposition.....	140
3.1.5.1b Results Obtain by Trial & Error Method.....	143

CONTENTS

	Page
3.1.5.1c Model Validation by Testing the Influence of Bath Concentration.....	146
3.1.6 Discussion	148
3.1.7 Conclusion.....	149
3.2 Mixed Species Model.....	150
3.2.1 Introduction.....	150
3.2.2 Model Assumption.....	150
3.2.3 Theoretical Model.....	151
3.2.3.1 General Mechanism of the Electrode Reaction.....	151
3.2.3.2 Mass Transfer Effect.....	152
3.2.3.3 Electrochemical Kinetic.....	154
3.2.4 Results of the Global Model.....	157
3.2.4.1 Comparison between Experimental and Theoretical Results.....	157
3.2.4.2 Model Validation.....	159
3.2.5 Discussion.....	160
3.2.6 Conclusion	161
3.3 Effect of Complexing Agent on Zn-Ni Alloy Deposition.....	162
3.3.1 Introduction.....	162
3.3.2 Experiment.....	163
3.3.3 Results and Discussions.....	163
3.3.4 Ionic Strength Effect.....	165
3.3.5 Conclusion.....	169
GENERAL CONCLUSION	170
REFERENCES	173
BIOGRAPHY	179

LIST OF TABLES

Table	Page
PART 1 : MACROSCOPIC MODEL	
2.1 Effect of stirring rate on the deposition rate and on mass transfer coefficient and diffusion layer thickness.....	31
PART 2 : ANALYSIS OF THE CURRENT DISTRIBUTION IN DIFFERENT ELECTROPLATING REACTORS	
2.1 Operating conditions for RCH tests.....	59
PART 3 : MICROSCOPIC MODEL	
1.1 Types of electrodeposited Zn-Ni alloy.....	72
2.1 Elemental deposition analysis focusing on the substrate effect.....	105
3.1 Electrochemical rate expressions for Zn and Ni alloy simulation.....	121
3.2 Electrochemical rate expressions for nickel deposition on nickel substrate simulation.....	125
3.3 Kinetic parameters of Ni ₂ Ni and H ₂ Ni.....	126
3.4 Electrochemical rate expressions for zinc deposition on zinc substrate simulation.....	130
3.5 Kinetic parameters of Zn ₂ Zn and H ₂ Zn.....	130
3.6 Electrochemical rate expressions for zinc deposition on zinc substrate simulation.....	134
3.7 Kinetic parameters of Ni ₂ Zn and H ₂ Zn.....	135
3.8 Electrochemical rate expressions for zinc deposition on nickel substrate simulation.....	138
3.9 Kinetic parameters of Zn ₂ Ni and H ₂ Ni.....	139
3.10 Kinetic parameters.....	143
3.11 Ratio of partial current alloy at different metal concentration at -1.4 V E _{app}	147

LIST OF TABLES

Table	Page
3.12	Electrochemical rate expressions for Zn and Ni alloy simulation.....155
3.13	List of the kinetic parameters.....157
3.14	Partial current of alloy obtained at -1.4 V for various operating conditions.....164
3.15	Partial current of alloy obtained at -0.01 A and various operating conditions.....165
3.16	Concentration of the equilibrium constant (k_i) of complex Zn-Cl in Zn-Ni electrolyte with and without potassium chloride.....167
3.17	Calculated parameter in each bath conditions according to equation 4.2 and 4.3 , and the Butler-Volmer equation.....168
3.18	The percentage of nickel and zinc obtained in different bath concentration.....168

LIST OF FIGURES

Figure	Page
PART 1: MACROSCOPIC MODEL	
1.1 Experimental determination of the kinetic constants, i_0 and α , using the Tafel equation.....	8
1.2 Steady-state concentration profiles for the process $O + ne^- \rightarrow R^2$	11
1.3 The time evolution of the concentration profiles for the reaction $O + ne^- \rightarrow R^2$	13
1.4 Ideal types of chemical reactors: (a) Simple batch reactor; (b) Continuous stirred tank reactor; (c) Plug flow reactor.....	17
1.5 Material balance over plug flow, parallel plate reactor.....	21
2.1 Electrochemical batch reactor for copper removal.....	25
2.2 Normalized copper concentration against time curve at different applied current densities, with initial concentration of 0.14 kg m^{-3} , stirring rate 200 rpm.....	27
2.3 Normalized copper concentration against time curve at different applied current densities, with initial concentration of 0.4 kg m^{-3} , stirring rate 200 rpm.....	27
2.4 Normalized copper concentration against time curve at different applied current densities, with initial concentration of 0.5 kg m^{-3} , stirring rate 200 rpm.....	28
2.5 A plot of cathodic potential reference saturated calomel electrode against time at different applied currents, and initial copper concentration of 0.4 g dm^{-3}	29
2.6 Normalized copper concentration against time curve at different stirring rate, initial copper concentration 0.4 g dm^{-3} and applied current 0.2 A.....	30
2.7 Normalized faradaic current densities against time curve at different applied current densities, for initial concentration of 0.5 kg m^{-3} , and stirring rate of 200 rpm.....	33

LIST OF FIGURES

Figure	Page
2.8	A plot of experimental and predicted normalized copper concentration evolution versus time at different applied current densities, initial concentration of 0.14 kg m^{-3} , and stirring rate of 200 rpm.....34
2.9	A plot of experimental and predicted normalized copper concentrations evolution versus time at different applied current densities, initial concentration of 0.4 kg m^{-3} , and stirring rate of 200 rpm.....35
2.10	A plot of experimental and predicted normalized copper concentrations evolution versus time at different applied current densities, initial concentration of 0.5 kg m^{-3} , and stirring rate of 200 rpm.....35
PART 2 : ANALYSIS OF THE CURRENT DISTRIBUTION IN DIFFERENT ELECTROPLATING REACTORS	
1.1	Length scales of electrochemical phenomena entering into theoretical modeling.....38
1.2	Secondary current distribution in the Hull cell calculated for different values of Wagner number assuming Tafel kinetics.....41
1.3	Standard Hull cell, dimension indicates in mm.....42
1.4	Standard Hull cell theoretical current density distribution at 2 A total current.....43
1.5	Hydrodynamically Controlled Hull Cell.....44
1.6	Hydrodynamically Controlled Hull Cell: (a) HCHC, partially submerged with one baffle; (b) Equipotential line distribution calculation; two-dimensional representation of the cell:

LIST OF FIGURES

Figure	Page
vertical distance from cell bottom; horizontal distance from cathode surface.....	45
1.7 Rotating disk cathode and stationary cylinder anode.....	45
1.8 Deposit thickness distribution on a rotating cone surface.....	46
1.9 The hydrodynamic electroplating test cell.....	47
1.10 The thickness and current distributions for the Hull cell and the hydrodynamic electroplating test cell (HETC) without agitation.....	48
1.11 Rotating Cylinder Hull (RCH) cell for electrodeposition studies.	48
1.12 The modified Mohler cell with forced electrolyte flow.....	49
2.1 Schematic of the Mohler cell.....	51
2.2 The modified Mohler cell with forced electrolyte flow.....	52
2.3 Electrolyte circuit.....	52
2.4 Partition of copper deposit on cathode surface of the Mohler cell.....	54
2.5 Dependence of dimensionless current density distribution versus dimensionless distance for various average current densities.....	55
2.6 Dependence of the dimensionless current density distribution versus dimensionless distance for various average current densities, and comparison with simulated results corresponding to a primary current distribution.....	56
2.7 Dependence of current density distribution versus distance.....	57
2.8 Potential distribution in the reactor, (a) our modified Mohler cell and (b) the original Mohler cell.....	58
2.9 Schematic diagram of the conventional RCH cell.....	59
2.10 Dimensionless current density ($i(x)/i_{ave}$) represented as a function of the dimensionless length (x^*).....	60

LIST OF FIGURES

Figure	Page
2.11	Dimensionless current density ($i(x)/i_{ave}$) represented as a function of the dimensionless length (x^*) and comparison with theoretical results corresponding to a (1D), (2D) and (3D).....61
2.12	Variation of dimensionless current density distribution versus dimensionless distance at various rotating speeds.....62
PART 3 : MICROSCOPIC MODEL	
1.1	Factors influencing the composition and structure of electroplated alloys.....66
1.2	Scheme showing the logarithm of the partial current densities.....69
1.3	Effect of current density on deposit composition.....74
1.4	Effect of current density on the percentage of nickel in Zn-Ni alloys electrodeposited regarding percentages of nickel.....76
1.5	Effect of current density on the percentage of nickel in Zn-Ni alloys electrodeposited at various temperatures.....76
1.6	Polarization curve during alloy deposition (V/Ag/AgCl) and effect of current density on nickel content of deposits, on current efficiency for alloy deposition and on current efficiency for hydrogen reduction.....77
1.7	Polarization curves for potentiostatic depositions.....78
1.8	Partial current densities for nickel and zinc as a function of applied potential during Zn-Ni alloy deposition and pure metal deposition from baths.....79
1.9	Effect of potential on the percentage of nickel in zinc nickel alloys electrodeposited.....80
1.10	Polarization curves and nickel percentage in the deposits obtained at various temperatures.....80

LIST OF FIGURES

Figure	Page
1.11	Effect of the nickel percentage in the bath on the nickel percentage of the deposits obtained at various potential value.....81
1.12	Dependence of the Ni content of the alloys on the deposition time for Zn-Ni deposits obtained under different conditions.....82
1.13	XPS depth profiles of Zn-Ni alloys at 20 mA cm^{-2} on commercial iron substrate.....83
2.1	General scheme of the EQCM/SIJ setup.....99
2.2	The current ratio of zinc to nickel versus current quantity.....101
2.3	Nickel, zinc and hydrogen currents evolution versus the deposition time. $E_{\text{app}} = -1.2 \text{ V / SCE}$. ZnCl_2 0.05 mol/L, $\text{NiCl}_2 \cdot 6\text{H}_2\text{O}$ 0.05 mol/L and pH of 4.....102
2.4	Nickel, zinc and hydrogen currents evolution versus the deposition time. $E_{\text{app}} = -1.5 \text{ V / SCE}$. ZnCl_2 0.05 mol/L, $\text{NiCl}_2 \cdot 6\text{H}_2\text{O}$ 0.05 mol/L and pH of 4.....104
2.5	Hydrogen evolution on zinc and nickel substrates.....105
2.6	Nickel deposition on zinc and nickel substrates.....107
2.7	Zinc deposition on zinc and nickel substrates.....108
2.8	Hydrogen evolution current density for alloy and elemental experiments data.....109
2.9	Nickel current density for alloy and elemental experiments data.....110
2.10	Zinc current density for alloy and elemental experiment data.....110
2.11	The influence of coelement concentration on nickel partial current density.....111
2.12	The influence of coelement concentration on zinc partial current density.....112

LIST OF FIGURES

Figure	Page
3.1 Diagram of Zn-Ni alloy codeposition	116
3.2 Scheme of nickel deposition on nickel substrate.....	123
3.3 The experiment and model simulation of Ni_Ni.	127
3.4 The experiment and model simulation of H ₂ _Ni.....	127
3.5 Scheme of zinc deposition on zinc substrate.....	128
3.6 The experimental and model simulation of Zn_Zn.	131
3.7 The experimental and model simulation of H ₂ _Zn.....	131
3.8 Chronoamperogram of Zn-Ni and Ni_Zn elemental deposition.....	132
3.9 Sketch of the mechanism assumed for nickel deposition on zinc substrate.....	132
3.10 The experimental and model simulation of Ni_Zn.	135
3.11 The experimental and model simulation of H ₂ _Zn.....	136
3.12 Sketch of the mechanism assumed for zinc deposition on nickel substrate.....	136
3.13 The experimental and model simulation of Zn_Ni.....	139
3.14 The experimental and model simulation of H ₂ _Ni.	140
3.15 Nickel partial current density in alloy simulation and experimental data(substrate model)	141
3.16 Zinc partial current density in alloy simulation and experimental data(substrate model).....	141
3.17 Hydrogen partial current density in alloy simulation and experimental data (substrate model)	142
3.18 Percentage of nickel in alloy simulation and experimental data.....	142
3.19 Partial current density of zinc in alloy simulation and experimental data obtained by Trial & Error method.....	144
3.20 Partial current density of nickel in alloy simulation and experimental data obtained by Trial & Error method	144

LIST OF FIGURES

Figure	Page
3.21	Partial current density of hydrogen in alloy simulation and experimental data obtained by Trial & Error method145
3.22	Percentage of nickel in alloy simulation and experimental data obtained by Trial & Error method.....145
3.23	Predicted influence of coelement concentration on nickel partial current (substrate model)146
3.24	Predicted influence of coelement concentration on zinc partial current (substrate model)147
3.25	Diagram of Zn-Ni alloy codeposition.....151
3.26	Nickel partial current density in alloy simulation and experimental data (mixed species model)158
3.27	Zinc partial current density in alloy simulation and experimental data (mixed species model).....158
3.28	Hydrogen evolution partial current density in alloy simulation and experimental data (mixed species model)159
3.29	Predicted influence of coelement concentration on nickel partial current (mixed species model)160
3.30	Predicted influence of coelement concentration on zinc partial current (mixed species model)160
3.31	Effect of KCl complexing agent on the Chronoamperogram.....164

NOMENCLATURES

Standard Subscripts

a	anodic
c	cathodic
O	pertaining to species O in $O + ne^- \rightarrow R$
R	pertaining to species R in $O + ne^- \rightarrow R$

PART 1 : MACROSCOPIC MODEL

Symbol	Meaning	Dimension
A_s	specific surface area	m^{-1}
C^{σ}	concentration at the electrode surface	$mol\ m^{-3}$
C^{∞}	concentration at the bulk concentration	$mol\ m^{-3}$
D_i	diffusion coefficient	$m^2\ s^{-1}$
E_e	equilibrium potential	V
E°	standard potential	V
F	Faraday number	Col equivalent ⁻¹
i	efficient current density	Col $m^{-2}\ s^{-1}$
i_o	exchange current density	Col $m^{-2}\ s^{-1}$
i_L	limiting current density	Col $m^{-2}\ s^{-1}$
$J_i(x)$	molar Flux of species i	$mol\ s^{-1}\ m^{-2}$
k	first order heterogeneous rate constants	$m\ s^{-1}$
k°	standard rate constant	$m\ s^{-1}$
x	distance from the electrode surface	m

NOMENCLATURES

PART 1 : MACROSCOPIC MODEL (continued)

Symbol	Meaning	Dimension
$C(0)$	initial concentration of metal ion	mol m^{-3}
$C(t)$	concentration of metal ion at time t	mol m^{-3}
C	concentration of metal ion	mol m^{-3}
I	efficient current	Col s^{-1}
I_{app}	applied current	Col s^{-1}
I_{H_2}	partial current for hydrogen evolution	Col s^{-1}
k_m	mass transfer coefficient	m s^{-1}
n	number of electron transfer	equivalent mol^{-1}
Q	volumetric flow rate	$\text{m}^3 \text{s}^{-1}$
S	actual electrode surface area	m^2
X	Fractional conversion	none
V	volume of solution	m^3

สถาบันวิทยบริการ
จุฬาลงกรณ์มหาวิทยาลัย

NOMENCLATURES

PART 2 : ANALYSIS OF THE CURRENT DISTRIBUTION IN DIFFERENT ELECTROPLATING REACTORS

Symbol	Meaning	Dimension
F	Faraday's constant, 96484.6	Col mol ⁻¹
h	cathode length	mm
i_{ave}	average current density	mA.mm ⁻²
k	electrolyte conductivity	S.m ⁻¹
L	characteristic length of the system	mm
M	atomic weight of copper, 63	g.mol ⁻¹
n	number of electron transfer	equivalent mol ⁻¹
t	time	s
W	deposit weight	g
x^*	dimensionless length	none
$(i(x^*)/i_{ave})$	dimensionless current density	none
$Wa.$	Wagner number	none

NOMENCLATURES

PART 3 : MICROSCOPIC MODEL

Symbol	Meaning	Dimension
A'	a constant (function of the absolute temperature, of the dielectric constant, and of the charge of the ionic reactants)	none
$b_{2,M}$	Tafel constants	V^{-1}
C_M^{2+}	surface concentration of species M^{2+}	mol l^{-1}
c_i	concentration	mol l^{-1}
I	ionic strength ion	mol l^{-1}
$k_{1,M}$ and $k_{2,M}$	potential dependent rate constants	$\text{cm s}^{-1}, \text{mol cm}^{-2} \text{s}^{-1}$
$k_{1,M}^{\circ}$ and $k_{2,M}^{\circ}$	pre-exponential factors of $k_{1,M} = k_{1,M}^{\circ} \exp(b_{1,M}V)$	cm s^{-1}
K_1	rate constant at ionic strength I	cm s^{-1}
K_0	rate constant at infinite dilution	cm s^{-1}
m_B	mass of element B deposited in the alloy	g
M_B	atomic weight of element B	g mol^{-1}
n_B	number of electrons involved in the reaction of element B	equivalent mol^{-1}
Δt	deposition time	time
z_i	ion present charge	mol l^{-1}
Ni_Ni	nickel deposition on nickel substrate	
Ni_Zn	nickel deposition on zinc substrate	
Zn_Zn	zinc deposition on zinc substrate	
Zn_Ni	zinc deposition on nickel substrate	
H ₂ _Ni	hydrogen evolution on nickel	
H ₂ _Zn	hydrogen evolution on zinc	
Zn-Ni	zinc and nickel codeposition	

NOMENCLATURES

PART 3 : MICROSCOPIC MODEL (continued)

Symbol	Meaning	Dimension
Greek Characters		
η	overpotential,	mV
ρ	electrolyte resistance, 0.187	$\Omega.m$
β_c	cathodic Tafel constant, 30.8	mV
γ_i	activity coefficient,	none
θ_i	the surface covered by specie i	none
α_a and α_c	anodic and cathodic transfer coefficients	none
ϕ	potential	mV
μ_i	charge of species i	none
v_x	velocity,	$m s^{-1}$
δ	boundary layer thickness	m

สถาบันวิทยบริการ
จุฬาลงกรณ์มหาวิทยาลัย

GENERAL INTRODUCTION

Nowadays, electrochemistry has wide application fields including thin or thick layer depositions, metals machining, energy production or organic synthesis without forgetting organic and heavy metals depolluting. For each application, the necessary knowledge to conduct the process is different and the analysis scale differs also depending on the needed accuracy.

Over 10 years ago, a lot of studies deal with the electrolytic removal (electrodeposition, electrocoagulation, electroprecipitation, etc) of heavy metals. By reason of environmental constraint, it corresponds to an only one step process, which can provide great economical profits. The operating cost is much cheaper than that of conventional process and no or little volume of sludge is produced during an electrochemical process compared with conventional chemical precipitation process. The strongest advantage of electrochemical process is no chemical contamination in treated water. In this kind of process the main parameter is the metal concentration. In this case, a macroscopic model is often sufficient to design and built the apparatus, which permit to destroy the pollutant. This model can also predict the evolution of the pollutant species versus time and constitute a convenient tool to operate these processes.

In recent years, electrochemistry application has been increasingly interested in the electronics industry, generally micro-industrial applications. The micro-industrial applications use electrochemical deposition to build layer or device by electrodeposition of metallic layers. Also, micromachining is used to build holes, and so on, necessary to elaborate microsystems. In this case, the knowledge of the metal concentration evolution versus the time is less interesting. It is better to know the current distribution on the electrode to design a best device, which is able to generate items required. The metal deposition operations depend on a great number of chemical and operational parameters such as local current density, electrolyte concentrations, complexing agents, buffer capacity, pH, leveling agents, brighteners, surfactants, contaminants, temperature, agitation, substrate properties, cleaning procedure. All these parameters act on the structure of the deposit and also on its

composition, in terms of alloy and its properties. Accordingly, the determination of these parameters is very important. These parameters are often determined empirically. For this, a lot of experiments have to be studied the effect of the operating conditions, mainly the applied current density. To decrease this number of experiments, some cells with specific geometries have been elaborated so as to produce well-known non-homogeneous distribution. In relation to these cells, it greatly ease to test a wide range of current density effects, depending on the cell used. Even if these cells provide an easier and quickest way to develop a new plating process, they do not give a better understanding of phenomena undergoing in the reactor. So, it is better to develop a model, which can explain phenomena being used to conduct their process.

The increasing availability of computing power is able to simulate complex electrochemical phenomena, which in the past must be studied in a more empirical and qualitative way. There is a difficulty studying all relevant parameters of microscopic mathematical models for deposition process. Microscopic models are nevertheless greatly useful because they quantitatively examine relationships, existing among mutually dependent parameters. Microscopic mathematical modeling can be applied to many different deposition problems, for example:

- Identification of mechanisms as a guide to new alloy development experiments.
- Criteria for process scale up or scale down.
- Cell design and optimization

In the case of alloy deposition, these models could also be used, for example:

- Prediction of the alloy composition from a minimum number of experiments.
- Control of local composition variations on a nanoscopic, microscopic or macroscopic scale based on the consideration of current and reaction distribution.

But these models need parameters, which are easier to determine for a single metal deposition, comparing with an alloy.

As mentioned above, all information is summarized and then applied for a plating process. It appears that:

- Macroscopic models are needed to follow the concentration species during the plating process in order to know when species must be added to avoid their depletion or when the bath must be changed. This model could also be useful to design and conduct an electrochemical process to destroy cleanly plating bath at its end of life. This fact is more and more important in plating process due to environmental constraints.
- Experimental or theoretical determination of the current distribution in the reactor is necessary to conveniently design the reactor, in order to obtain layers with the desired properties.
- Determinations of mechanisms and of its parameters are important to subsequently build models to permit a better understanding of what happen in the reactor and optimize the process.

Thus, this report is composed of three parts. The first part, dealing with the macroscopic modelling of the electrochemical reactor, comprises two chapters. The first one is a bibliographic review including different concepts necessary to introduce and well understand the different macroscopic models. The second chapter presents initial experimental results, obtained during the recovery of copper by using a batch reactor. These results are further compared with those coming from a macroscopic model.

The second part affects the analysis of the current distribution in different electroplating reactors. This part is made up of two chapters. The first presents a bibliographic report concerning different cells that have been built to develop special current distribution in order to check the effect of the current distribution on the bath efficiency. In the second chapter, there are experimental results obtained with two kinds of reactors. These results concern mainly the current distribution in these devices. These distributions are explained and the efficiency of each cell is

commented before presenting a classification of the various cells versus the goal chosen.

In the last part, the research team concentrates on the proposal of mechanism models and the determination of the parameter of mathematical models, predicting the composition of an electrodeposited binary alloy. For this work, the Zn-Ni alloy is chosen due to this alloy presents an anomalous deposition being difficult to modeling. Also, it presents an industrial interest for protecting steel against corrosion. This part consists of three chapters. The first one is a review of the bibliography, regarding alloy deposition, and more specifically about Zn-Ni alloy deposition. The second chapter presents a set of experiments being performed in order to check the different models presented previously and also to be used subsequently for determining the parameter of models. In the third chapter of this part, it is focused on the modeling of the Zn-Ni alloy. Two models, assuming homogeneous current distribution and mass transport rate on the working electrode, have been used. Each model assumption is first introduced; afterwards, the parameters of the model are calculated with respect to the experimental results of the previous chapter. At the end of the chapter, we conclude on the better-suited model.

At the end of this work, the best practice is given to conduct an electroplating process and more generally all electrochemical process.

สถาบันวิทยบริการ
จุฬาลงกรณ์มหาวิทยาลัย

PART 1

MACROSCOPIC MODEL

Introduction

Plating baths are composed of one or several metals that are used to deposit in the electrode surface. During the plating process, the metal concentration is decreased with time. The metal concentration and properties effecting on the product quality therefore should not be too low to use for plating on the substrate material. In this part we consider the macroscopic model monitoring the bulk concentration of the metal in the electroplating bath. This study could also be used during the treatment of the plating bath at the end of its life and electrosynthesis.

Rate of metal deposition could be under two controlled systems, the kinetic and mass transfer. We study a changing rate of metal concentration by considering copper concentration versus time. According to this study, we can observe time of which copper concentration is too low for plating bath. At this time, the bath must be destroyed before laundry or to be regenerated by adding reacting species. Time duration for plating process at its end of life can thus be determined.

This macroscopic model section is composed of two chapters; i.e., bibliography and experimental parts (monitoring rate of copper concentration). In the bibliography part, a summary of electrochemistry considering the kinetic and mass transfer system and the electrochemical reactor has been described. In the experimental part, the removal rate of copper is monitored versus time under kinetic and mass transfer controlled.

CHAPTER I

Bibliography

1.1 Summary of Electrochemical Theory

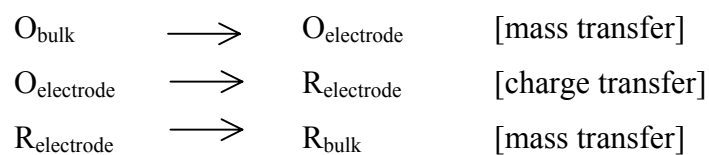
Electrochemistry involves chemical phenomena associated with a charge transfer, which can heterogeneously occur on electrode surfaces. In this chapter, a brief overview of electrochemistry, particularly of electrode reactions are described in order to show the interdisciplinary nature and versatility of electrochemistry and to introduce a few of the important fundamental concepts. Before discussing, it is worth looking briefly at the nature of electrode reactions¹.

1.1.1 The Nature of Electrode Reactions

Electrode reactions are heterogeneous and take place in the interfacial region between electrode and solution. The simplest electrode reaction could inter-convert at an inert surface, two species, O and R, which are completely stable and soluble in the electrolysis medium containing an excess of an electrolyte:



The electrode reaction is a sequence of more basic steps. To maintain a current it is essential to supply reactant to the electrode surface and also to remove the product, as well as for the electron transfer reaction at the surface to occur. For example, in experimental conditions where O is reduced to R, the electrode reaction must have three steps:



Since the rate of reduction, and hence cathodic current, is determined by the rate of the overall sequence. The rate must depend on the slowest step. Thus to understand the characteristics of an electrode reaction, both mass transport and electron transfer have to be considered.

1.1.2 Electron Transfer

Mechanisms of electrode reactions are explained the most simple case of simple electron transfer without a chemical transformation. Mechanisms at equilibrium and the non-equilibrium have been analysed. In the system involving reagents and products at an equilibrium stage (departure from the equilibrium) , the rates of the reactions in each direction are equal. For reactions at an electrode, the equilibrium expression is the Nernst equation.

1.1.2a The Situation at Equilibrium

A simple electron exchange between ions in the electrolyte solution and an electrode can be written as



Here, k_c and k_a are the first order heterogeneous rate constants for the reduction and oxidation reactions respectively. The definition of an equilibrium for such a system can be based on either thermodynamic or kinetic principles. The kinetic definition of equilibrium is very straightforward: the net rate of a chemical change in the reaction must be zero. In other words,

$$k_c C_O^\sigma = k_a C_R^\sigma \quad (1.3)$$

where C_O^σ and C_R^σ are the concentrations of O and R at the electrode surface. If the concentrations of O and R are defined in units of mol m^{-3} , then k_c and k_a are expressed

in units of m s^{-1} . Alternatively, equilibrium can be defined in terms of the current densities by the identity

$$i = i_c + i_a = 0 \quad (1.4)$$

where

$$i_c = -nF k_c C_O^\sigma \quad (1.5)$$

and

$$i_a = nF k_a C_R^\sigma \quad (1.6)$$

i_a for the current of oxidation process has a positive, sign whereas, i_c , the current for the reduction process has a negative sign. i_a is referred to as the anodic partial current density and i_c as the cathodic partial current density. The measured current density, i ($\text{Col m}^{-2} \text{ s}^{-1}$), is therefore made up from contributions of the anodic and cathodic processes.

Here the key assumption concerns the potential dependence of k_c and k_a in the relation 1.2. This is usually written as

$$k_c = k_c^\circ \exp \left\{ -\frac{\alpha_c nF(E - E_e)}{RT} \right\} \quad (1.7a)$$

and

$$k_a = k_a^\circ \exp \left\{ -\frac{\alpha_a nF(E - E_e)}{RT} \right\} \quad (1.7b)$$

where k° is the standard rate constant, and α_a and α_c are the anodic and cathodic transfer coefficients, respectively. For the moment, α_a and α_c are assumed to be constants which take values between 0 and 1, and it is commonly assumed that $\alpha_c = 0.5$. E_e (V) is the equilibrium potential related to the standard potential of the couple O/R, E° (V).

At the equilibrium potential, the anodic and cathodic currents must sum up to zero, Eq.1.4, the magnitudes of the anodic and cathodic partial currents are identical to the exchange current density, i_0 :

$$|i_c| = |i_a| = i_0 \text{ at } |E = E_e| \quad (1.8)$$

The expression for i_c and i_a can now be substituted from Eqs. 1.5 and 1.7, assuming $\alpha_a = 1 - \alpha_c$, to give

$$nFC_o^\sigma k^\circ \exp\left\{-\frac{\alpha_c nF(E - E_e)}{RT}\right\} = nFC_R^\sigma k^\circ \exp\left\{\frac{(1 - \alpha_c)nF(E - E_e)}{RT}\right\} \quad (1.9)$$

Rearrangement of Eq. 1.9 leads to the expression

$$E_e = E^\circ + \frac{RT}{nF} \ln \frac{C_o^\sigma}{C_R^\sigma} \quad (1.10)$$

The system is at equilibrium so $C_o^\sigma = C_o^\infty$ and $C_R^\sigma = C_R^\infty$, where C_o^∞ and C_R^∞ are the bulk concentration of O and R. Equation 1.10 becomes identical to the Nernst equation².

1.1.2b Departure from Equilibrium (Activation Polarization)

It is an experimental fact that the rate of an electron transfer reaction is sensitive to changes in electrode potential, and it is therefore suitable to choose the equilibrium potential as a reference point and then to determine the overpotential, η (V) as.

$$\eta = E - E_e \quad (1.11)$$

Alternatively, the overpotential can be referred to the standard potential using the Nernst equation.

$$\eta = E - E_c - \frac{RT}{nF} \ln\left(\frac{C_o^\infty}{C_R^\infty}\right) \quad (1.12)$$

The exchange current density, i_o can now be obtained by substitution of Eq.1.12 into 1.9

$$i_o = |i_c| = |i_a| = nFk^o (C_R^\infty)^{\alpha_c} (C_o^\infty)^{1-\alpha_c} \quad (1.13)$$

The net current density can now be expressed in terms of the exchange current density in the form

$$i = i_a + i_c = i_o \left\{ \exp\left(\frac{(1 - \alpha_c)nF\eta}{RT}\right) - \exp\left(-\frac{\alpha_c nF\eta}{RT}\right) \right\} \quad (1.14)$$

Eq 1.14 is known as the Butler-Volmer equation², and it forms the basis for the theoretical description of electrode processes.

It is often convenient to consider the limiting behavior of Eq 1.14 for small and large values of the exponential terms. The exponential terms can be written as Taylor expansions.

For small values of the arguments of the parameters $\alpha_c nF\eta / RT$ and $(1-\alpha_c)nF\eta / RT$, the first two terms can be combined into

$$i = \frac{i_o nF\eta}{RT} \quad \text{for } \alpha_c nF\eta / RT \ll 1 \quad (1.15)$$

In practice, the linear approximation can be used for $|\eta| \ll 10/n$ mV when the error due to the approximation is about 1% for $\alpha_c = 0.5$.

For large positive or large negative overpotentials, under these conditions, one or other of the exponential terms in the Butler-Volmer equation dominates, the relation and the limiting relationships become

$$i = i_c = -i_0 \exp(-\alpha_c n F \eta / RT) \quad (1.16a)$$

for large negative overpotentials, and

$$i = i_a = -i_0 \exp\{(1-\alpha_c) n F \eta / RT\} \quad (1.16b)$$

for large positive overpotentials.

These relationships are often written in the form of the Tafel equations¹:

$$\eta = -\frac{2.3RT}{\alpha_c n F} \log|i| + \frac{2.3RT}{\alpha_c n F} \log i_0 \quad (\eta < 0) \quad (1.17a)$$

$$\eta = \frac{2.3RT}{\alpha_a n F} \log|i| + \frac{2.3RT}{\alpha_a n F} \log i_0 \quad (\eta > 0) \quad (1.17b)$$

where i is the net current density. The Tafel approximation is generally used for $|\eta| \gg 70/n$ mV.

Eqs. 1.17a and b are known as the Tafel equations and are the basis of a simple method of determining the exchange current density and a transfer coefficient, as shown in Figure 1.1.

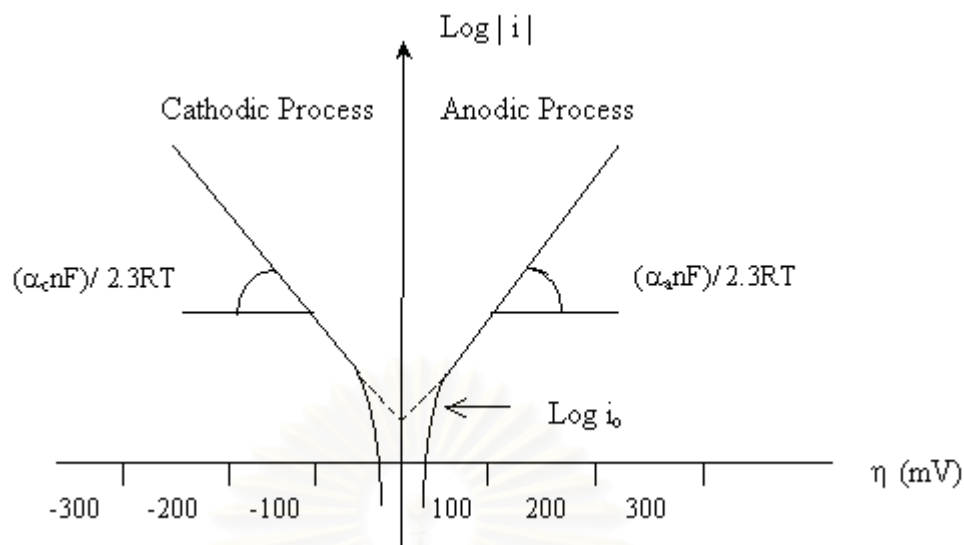


Figure 1.1 Experimental determination of the kinetic constants, i_0 and α , using the Tafel equation²

Tafel equations contain information about both the exchange current density, i_0 , and the transfer coefficient, α . Plots of $\log |i|$ vs η are more commonly used than the true Tafel plots of η vs $\log |i|$, simply because η is now usually the controlled variable. Figure 1.1 illustrates plots of this kind, and shows how i_0 is obtained from the extrapolation of the data obtained in the limiting Tafel regions at high positive and negative values of η . The relationships between the slopes of the plots and the value of α are given by

$$\frac{d(\log |i|)}{d\eta} = -\frac{\alpha_c nF}{2.3RT} \quad (1.18a)$$

$$\frac{d(\log |i|)}{d\eta} = \frac{\alpha_a nF}{2.3RT} \quad (1.18b)$$

1.1.3 Mass Transfer

This part, in turn, reaction rate is affected not only by the electrode reaction itself but also by the transport of species to and from a bulk solution. However the

kinetic of electron transfer rate is very rapid compared to mass transfer processes rate. This mass transport can occur by diffusion, convection, or migration.

Mass transfer is the movement of materials from one location in solution to another, arises either from differences in electrical or chemical potential at the two locations. The modes of mass transfer are

1. *Migration*. Movement of a charged body under the influence of an electric field (a gradient of electrical potential)
2. *Diffusion*. Movement of a species under the influence of a gradient of chemical potential (activities) (i.e., a concentration gradient).
3. *Convection*. (Stirring or hydrodynamic transport) Generally, fluid flow occurs because of forced convection, and may be characterized by stagnant regions, laminar flow, and turbulent flow and natural convection (convection caused by density gradients),

Mass transfer to an electrode is governed by the Nernst-Planck equation³, which is written for one-dimensional mass transfer along the x-axis as

$$J_i(x) = -D_i \frac{\partial C_i(x)}{\partial x} - \bar{z}_i C_i \frac{\partial \phi(x)}{\partial x} + C_i v_x(x) \quad (1.19)$$

where $J_i(x)$ is the flux of species i ($\text{mole s}^{-1} \text{m}^{-2}$) at distance x from the surface, D_i is the diffusion coefficient ($\text{m}^2 \text{s}^{-1}$), $\partial C_i(x)/\partial x$ is the concentration gradient at distance x , $\partial \phi(x)/\partial x$ is the potential gradient, \bar{z}_i and C_i are charge and concentration of species i , respectively, and $v_x(x)$ is the velocity (m s^{-1}) with which a volume element in solution moves along the axis. The three terms on the right hand side of the equation 1.19 represent the contributions of diffusion, migration, and convection, respectively, to the flux.

1.1.3a Steady-State Mass Transfer

In the presence of a base electrolyte, diffusion is the only form of mass transport

for the electroactive species, which need to be considered. The simplest model is that of linear diffusion to a plane electrode; it is assumed that the electrode is perfectly flat and of infinite dimensions, so that concentration variables can only occur perpendicular to the electrode surface. Diffusion may then be characterized by Fick's law in a one dimensional form.

Fick's law states that the flux of any species, i , through a plane parallel to the electrode surface is given by

$$J_i(x) = -D_i \frac{dC_i}{dx} \quad (1.20)$$

where D_i is the diffusion coefficient and typically has values around $10^{-9} \text{ m}^2 \text{ s}^{-1}$.

The number of electron reaching to the current is constant versus time, $i = -d(n\bar{e})/dt$. The first law applied at the electrode surface, $x = 0$, is used to relate the current to the chemical change at the electrode by equating the flux of O or R with the flux of electrons, where

$$\frac{i}{nF} = -D_c \left(\frac{\partial C_o}{\partial x} \right)_{x=0} \quad (1.21a)$$

or

$$\frac{i}{nF} = D_a \left(\frac{\partial C_R}{\partial x} \right)_{x=0} \quad (1.21b)$$

Close to the electrode surface zone, convection will not be an important form of mass transport, and it is therefore possible and certainly convenient for understanding of a boundary layer thickness, δ , which diffusion is the only significant form of mass transport. Outside this boundary layer, convection is strong enough to maintain the concentrations of all species uniform and at their bulk values. Using this

concept, the steady state concentration profiles for a solution of O and R are shown in Figure 1.2.

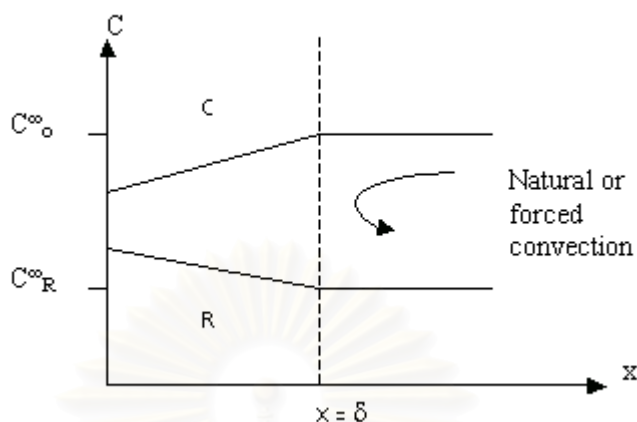


Figure 1.2 Steady-state concentration profiles for the process $O + ne^- \rightarrow R$

With the rotating disc electrode, the diffusion layer thickness is determined by the rotation rate of the disc, the layer becoming thinner with increasing rotation rate. The C_i vs x plot inside the boundary layer must, in the steady state, be effectively linear. The steady state will be given by

$$i = -nFD \left(\frac{dC_O}{dx} \right)_{x=0} = nFD \frac{C_O^\sigma - C_O^\infty}{\delta} \quad (1.22)$$

The surface concentration C_O^σ is, of course, a function of potential, but the diffusion limited current density or limiting current density, i_L corresponds to the maximum flux, i.e. to potentials where $C_O^\sigma = 0$.³ Therefore

$$i_L = \frac{-nFDC_O^\infty}{\delta} \quad (1.23)$$

From equations 1.22 and 1.23, it could be deduced to

$$\frac{C_O^\sigma}{C_O^\infty} = 1 - \frac{i}{i_L} \quad (1.24)$$

1.1.3b Non Steady-State Mass Transfer

The second law discusses the change in concentration of i species with time due to diffusion. At a point in the center of n elements of solution bounded by two planes parallel to the electrode the concentration will change because diffusion is occurring both into and out of the element. This leads to the equation

$$\frac{\partial C_i}{\partial t} = D_i \frac{\partial^2 C_i}{\partial x^2} \quad (1.25)$$

The zone close to the electrode surface where the concentrations of O and R are different from those in the bulk is known as the diffusion layer.

The graph, showing the dependence of concentration on distance from the electrode surface, is known as concentration profiles. The concentration profiles are the complete solutions to Eq. 1.25, $C_i = f(x,t)$, but many experiments may be understood from a qualitative consideration of the way in which concentration profiles develop with time and vary with experimental parameters. For example, Figure 1.3 shows the time development of the concentration profiles for O and R during an experiment is carried out with a solution initially containing O but no R and in which the electrode potential is stepped at $t = 0$ in such a way as to cause the surface concentration of O to change instantaneously from C_o^∞ to zero due to the reaction $O + ne^- \longrightarrow R$. At a short time, the concentration of O will only have changed from its initial value, C_o^∞ , at points very close to the electrode surface, and the concentration profile will consequently be steep.

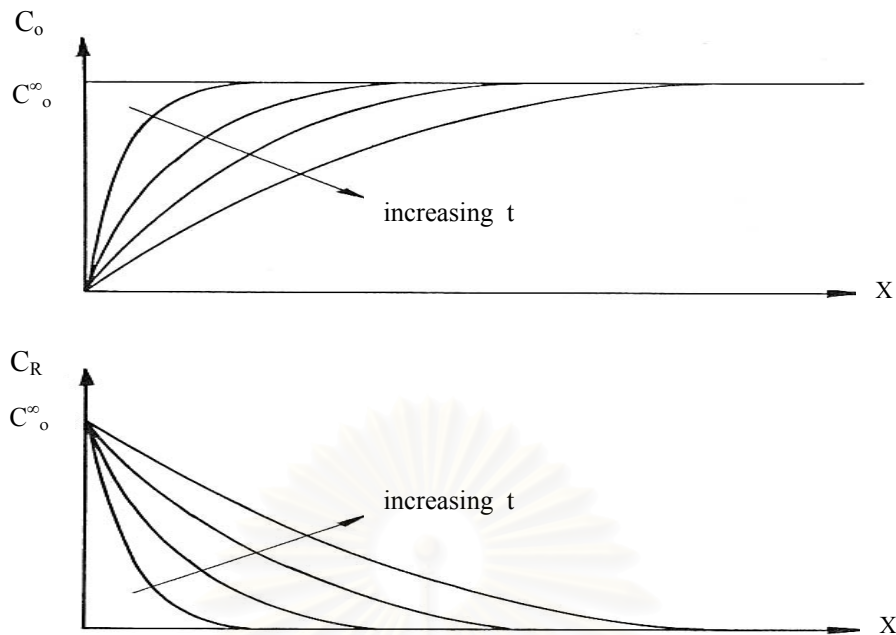


Figure 1.3 The time evolution of the concentration profiles for the reaction $O + ne^- \rightarrow R$ at a potential where the process is diffusion controlled, i.e. for $t > 0$, $C_o = 0$ at $x = 0$
 Initial: $C_o = C_o^\infty$ and $C_R = 0$ at all x^2

With increasing time, diffusion will cause the concentration profiles to relax towards their steady state by extending into solution and becoming less steep. Since the current is a simple function of the flux of O at the electrode surface, Eq. 1.22, we can also see that it will decrease with time. As indicated above, to obtain a more detailed knowledge of the transient, the equation is solved.

$$\frac{\partial C_o}{\partial t} = D_c \frac{\partial^2 C_o}{\partial x^2} \quad (1.26)$$

With the initial and boundary conditions which describe this particular potential step experiment.

$$\begin{aligned} &\text{at } t = 0 \text{ and for all } x, C_o = C_o^\infty \\ &\text{for } t > 0, \text{ at } x = 0, C_o^\sigma = 0 \\ &\text{and at } x = \infty, C_o = C_o^\infty \quad \forall t \end{aligned}$$

1.1.4 Concentration Evolution versus Time

In electrodeposition system, the rate of electrode reaction can be controlled by charge or mass transfer rate. In the case of charge transfer control, the molar flux density of metal reaction rate ion, J_D , is calculated from the applied current density according to Faraday's law as shown below:

$$J_D = -\frac{V}{S} \frac{dC}{dt} = \frac{i}{nFS} \quad (1.27)$$

where V is the volume and S is the electrode surface area of the reactor.

1.1.4a Charge Transfer Limiting Step

For a given reactor, a known ratio of apparent surface area to volume, A_s , Equation 1.27 becomes:

$$\frac{dC}{dt} = -\frac{iA_s}{nFS} \quad (1.28)$$

$$\frac{C(t) - C(0)}{C(0)} = -\frac{iA_s}{nFS} \int_0^t dt \quad (1.29)$$

The solution to this differential equation is

$$i = \frac{nFS}{A_s t} (C(0) - C(t)) \quad (1.30)$$

$$C(t) = C(0) - \frac{iA_s t}{nFS} \quad (1.31)$$

1.1.4b Mass Transfer Limiting Step

For the mass transfer controlled reaction case, the molar flux of metal ion defined by Fick's first law of diffusion is equal to that by Faraday's law shown in Equation 1.32.

$$J_D = -D \left(\frac{dC}{dx} \right) = \frac{I}{nF} \quad (1.32)$$

where I is the efficient current, Col s^{-1} which is not constant and relates with the concentration. It also depends on the type of reactor as shown in the following part.

1.2 Macroscopic Model

Electrochemical engineering is a multi-disciplinary subject that concerns the design, characterization and operation of electrochemical reactors and process⁵. Electrochemical reactors are used for a wide range of applications especially the environmental treatment⁶ considering the removal of toxic metal ions from waste water down to very low outlet concentrations. Following the composition of the electron during deposition, the reactor could also be used for electrochemistry synthesis.

Both in laboratory and in industries, the electrochemical reactor is a key component of an electrochemical process. Special attention must be taken in its design to achieve a high conversion rate of reactant to product as well as a high current efficiency for a desired reaction.

In view of the diverse applications of electrochemistry, a wide range of different electrochemical reactor designs is possible, ranging from traditional plate in tank configurations up to more sophisticated designs using, for example, modern filter press cells⁷, porous three-dimensional reactor⁸, or rotating electrodes cells⁹.

In this part, the studies focus on an electrochemical reactor that is an established unit process for the pollution control application, i.e., removing heavy metal in wastewater stream. The operation under charge transfer and mass transfer controlled has been analyzed, taking into account the idealized batch reactor and flow-through reactors in the single pass mode.

Two types of ideal fluid flow through the reactor, namely plug flow and perfect mixing flow, are commonly considered. In the first case, it is assumed that the fluid flow is continuous through the reactor with no mixing of the electrolyte in the direction of the flow between inlet and outlet, under steady state mode. The reactant and product concentrations are both functions of the distance but they are independent of time. As a result, the residence time must be equal for all species in the reactor. A reactor with such properties is called a plug flow reactor (PFR).

A perfectly stirred tank with a continuous flow through the reactor is called a continuously stirred tank reactor (CSTR). In this case, the concentration of reactants and products are uniform throughout the reactor. The reactant concentration within the reactor is equal to the outlet concentration, $C(\text{OUT})$, and is independent of time.

The most common example of a perfectly mixed reactor is the simple batch reactor in which the reactant is continuously stirred throughout a batch time during which reaction occurs. During the batch processing time, the concentration of reactants and products will progressively change. At any instant, however, the electrolyte composition is uniform through the reactor. The batch reactor is widely used due to its simplicity and versatility. Batch reactors are used for small-scale operations where they are more economical than continuous reactors. Figure 1.4 shows a sketch of three types of ideal reactor.

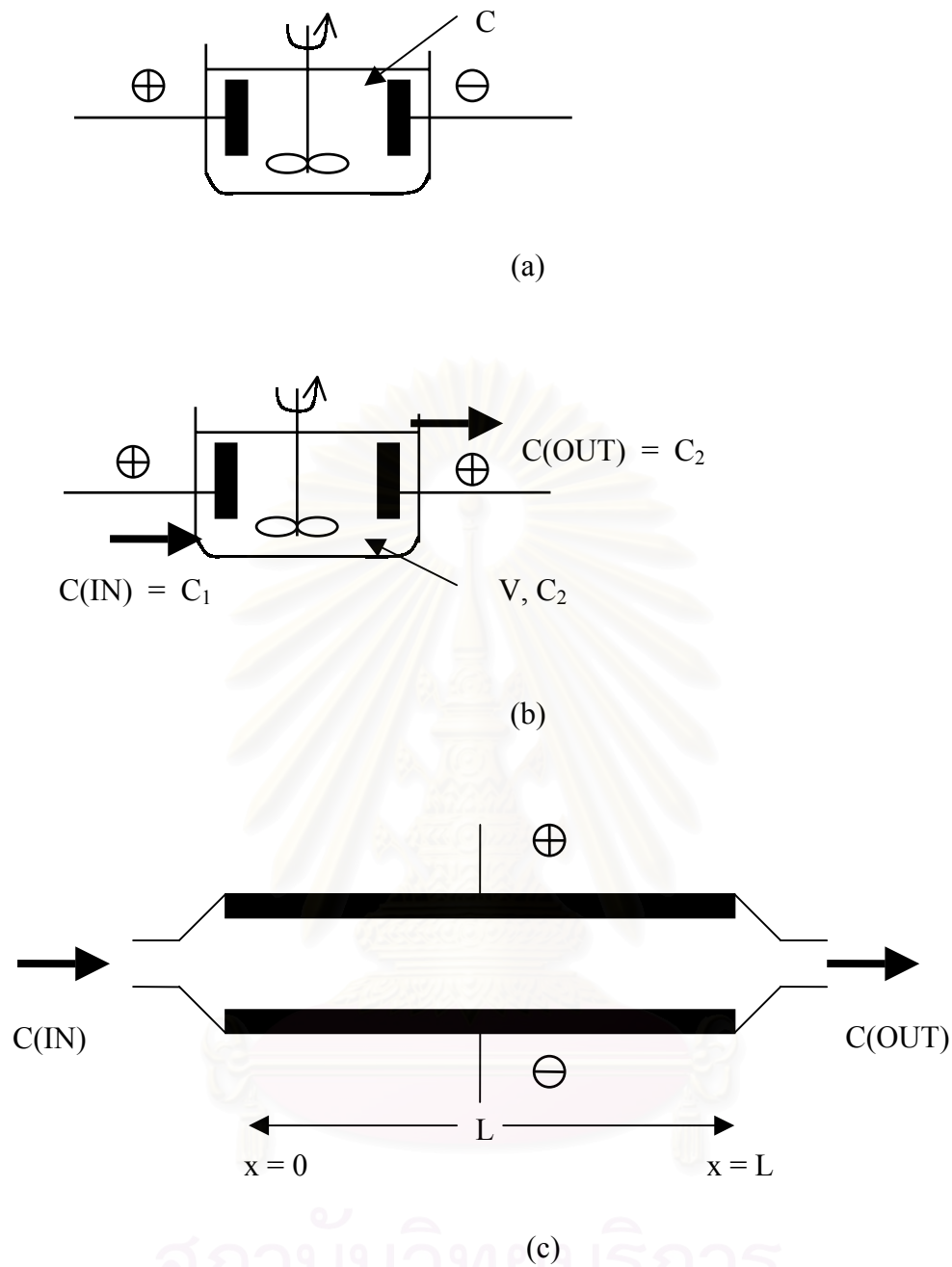


Figure 1.4 Ideal types of chemical reactors: (a) Simple batch reactor; (b) Continuous stirred tank reactor; (c) Plug flow reactor¹⁰

Here, this study considers batch reactors, PFRs and CSTRs operating under charge transfer control and complete mass transport controlled. For reactor analysis, a material balance (per unit of time) is set to determine the reactor design equations. The theoretical equations for the reactor design thus provide equations, describing

reactor's performance in terms of conversion and as a function of the mass transport coefficient, k_m .

1.2.1 Kinetic and Mass Transport in the Electrochemical Reactor

The conversion of an oxidized (Ox) to a reduced (Re) species of a redox couple Ox/Re can be considered:



The material balance is based on the principle of the matter conservation. In the case of the component O in reaction 1.33, this material balance can be written as:

$$\text{Rate of mass input} = \text{Rate of mass output} + \text{Rate of loss} \quad (1.34)$$

- For the case of a batch reactor, there is no inputs and outputs, so the relationship of Eg. 1.34 can be simplified to:

$$\text{Rate of accumulation of O} = - \text{Rate of disappearance of O} \quad (1.35)$$

- For the case of PFR and CSTR, there is no accumulation and the material balance for component O can be written as:

$$\text{Rate of mass input} - \text{Rate of mass output} = \text{Rate of mass disappearance} \quad (1.36)$$

In an electrochemical reaction the rate of mass disappearance of Ox (i.e., $d[O]/dt$) is given by the expression:

$$I/nFV = -d[O]/dt \quad (1.37)$$

where I is the cell current (A), n is the number of electrons involved in the electrode reaction and F is the Faraday constant (mole). $[O]$ is the concentration of component

O (mole m^{-3}) and V is volume of the electrolyte (m^3). The quantity $I = nF$ is the rate of reaction and has units of $mol\ s^{-1}$.

Here, the reaction is considered to take place under mass transport control and the value of I is the limiting current, I_l ($Col\ s^{-1}$) is given by:

$$I_l = nFk_m AC_B \quad (1.38)$$

where k_m is the mass transport coefficient which unit $cm\ s^{-1}$ (a type of heterogeneous rate constant), A is the electrode area (m^2) and C_B is the concentration of the electroactive species in the bulk electrolyte (mole m^{-3}).

Bard and Faulkner³ have described the characteristic of controlled current electrolysis, the change of the limiting current with time.

As long as the applied current (I_{app}) is less than the limiting current (I_l) at a given bulk concentration, the electrode reaction proceeds with 100% current efficiency. As the electrolysis proceeds, the bulk concentration of metal ion decreases with time and the limiting current decreases linearly with time.

At longer time, magnitude of the applied current is more than that of the limiting current, and the potential shifts to more negative value, where an additional electrode reaction can occur. This reaction contributes to the additional current, $I_{app} - I_l = I_{H_2}$. The current efficiency thus drops below 100%.

It is useful to express reactor performance in terms of the fractional reactant conversion, X . In the case of a constant volume system, this may be defined as¹⁰.

$$X = (C_0 - C) / C_0 \quad (1.39)$$

where C_0 (mole cm^{-3}) is the initial concentration of reactant and C (mole cm^{-3}) is the concentration at t time. $0 < X < 1$, $X=0$ for $t = 0$ and $X \rightarrow 1$ for $t \rightarrow \infty$

1.2.2 Mass Balance on an Electrochemical Reactor

1.2.2a Simple Batch Reactor

A batch reactor contains a volume of catholyte, V , having an initial concentration of reactant, C_0 which is subsequently reduced to a value, C , at time, t

The balance for the concentration species is rate of the cathodic reaction at any time is given by

$$-V \frac{dC}{dt} = \frac{I}{nF} \quad (1.40)$$

where I is the efficient current at time, t .

Considering that charge transfer is the limiting step in the electrochemical reactor, the solution to this differential equation is

$$C = C_i - \frac{It}{nFV} \quad (1.41)$$

Design equation, which expresses the fractional conversion under charge transport controlled reaction, has been derived as

$$X = \frac{It}{nFVC_0} \quad (1.42)$$

As mentioned before, for mass transfer control in the electrochemical reactor, the value of corresponding limiting current is, $I_l = nFk_mAC_0$. Substituting Eq 1.38 to Eq 1.40 and rearranging, we obtain:

$$-V \frac{dC}{dt} = k_m A C_o \quad (1.43)$$

$$C = C_o \exp(-k_m A t / V) \quad (1.44)$$

Design equation, which expresses the fractional conversion under mass transport controlled reaction, has been derived as

$$X = 1 - \exp(-k_m A t / V) \quad (1.45)$$

1.2.2b Plug Flow Reactor

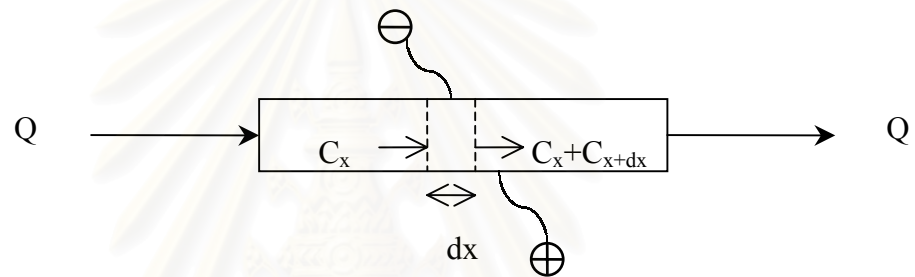


Figure 1.5 Material balance over plug flow, parallel plate reactor¹¹

Consider plug flow reactor included two electrodes, anode and cathode, separated by a certain distance as shown in Figure 1.5¹¹. A volumetric flow rate, Q ($\text{m}^3 \text{s}^{-1}$), of electrolyte solution enters this reactor with reactant concentration, C_x ($\text{m}^3 \text{s}^{-1}$), and leaves with reactant concentration, C_{x+dx} ($\text{m}^3 \text{s}^{-1}$). The apparent surface area to volume is A_s .

An instantaneous mass balance over the reactor gives following equations,

$$Q_x C_x - Q_{x+dx} C_{x+dx} = \frac{IA_s dx}{nF} \quad (1.46)$$

$$-Q \frac{dc}{dx} = \frac{IA_s}{nF} \quad (1.47)$$

$$dC = -\frac{IA_s}{QnF} dx \quad (1.48)$$

Considering that charge transfer is the limiting step in the electrochemical reactor, the solution to this differential equation is

$$C = C_o - \frac{IA_s}{QnF} x \quad (1.49)$$

Design equation, which expresses the fractional conversion under charge transport controlled reaction, has been derived as

$$X = \frac{IA_s}{QnFC_o} x \quad (1.50)$$

As mentioned before, for mass transfer control in the electrochemical reactor, the value of corresponding limiting current is, $I_l = nFk_mAC_o$. Substituting Eq 1.38 to Eq 1.48 and rearranging, we obtain

$$-\frac{dC}{dx} = \frac{k_m CA_s}{Q} \quad (1.51)$$

$$-\frac{dC}{C} = \frac{k_m CA_s}{Q} dx \quad (1.52)$$

$$C = C_o \exp\left(-\frac{k_m A_s x}{Q}\right) \quad (1.53)$$

Design equation which expresses the fractional conversion under mass transport controlled reaction, has been derived as

$$X = 1 - \exp\left(\frac{-k_m A x}{Q}\right) \quad (1.54)$$

1.2.2c Continuous Stirred Tank Reactor

Considering the CSTR when the device consists of a single compartment as seen in Figure 1.4b. The flow rates of solution, entering and leaving the reactor, are equal to Q ($\text{m}^3 \text{s}^{-1}$). The terminal concentrations of the reacting species being considered are constant and equal to C_1 and C_2 (mole cm^{-3}), with a net volume of V (cm^3).

The overall material balance for the general case of a stirred tank reactor, over a time interval, dt , can be seen from equation¹¹.

$$Q(C_1 - C_2) = \frac{I}{nF} \quad (1.55)$$

Under charge transfer control, the solution of the differential equation is

$$C_2 = C_1 - \frac{I}{nFQ} \quad (1.56)$$

Design equation which expresses the fractional conversion under charge transport controlled reaction, has been derived as

$$X = \frac{I}{nFQC_1} \quad (1.57)$$

For a single component CSTR, with the specified reactant undergoing a fast reaction, the limiting current density is related to the outlet concentration by $I_L = nFk_m AC_2$, and Eq 1.52 modifies to

$$Q(C_1 - C_2) = k_m C_2 A \quad (1.58)$$

Where A represents the electrode area (m²). The terminal concentration is related to the entrance concentration by

$$C_2 = \frac{C_1}{1 + k_m A/Q} \quad (1.59)$$

which could be compared for the plug flow reactor

The fractional conversion over the reactor under mass transfer control can be obtained by a simple manipulation on Eq 1.56

$$X = \frac{k_m A/Q}{1 + k_m A/Q} \quad (1.60)$$

Comparing to Eq 1.51, it is evident that a smaller X is obtained with the CSTR than plug flow reactor for given values of k_m, A and Q.

1.3 Conclusion

According to literature review, equations for macroscopic models have been established. Studying the macroscopic models, the experiment should be performed by considering only the bulk metal concentration evolution versus time. In this case, charge or mass transfer could control the rate of bulk metal concentration variation.

In order to simplify the model, the batch reactor is used to be the case study. In addition, copper solution can be used for this experimental determination of current distributions in a particular reactor. Copper deposition from a sulfate/sulfuric medium is a well-known electrochemical reaction and can be considered as a test reaction¹².

CHAPTER II

Analyzing Kinetics and Mass Transport on an Electrochemical Batch Reactor

2.1 Introduction

Kinetic and mass transport of the copper ion reaction rate is studied in this chapter. The considered parameters are the applied current, initial concentration, cathodic potential and stirring rate. According to those studied parameters, the concentrations of copper reducing with time are monitored under the kinetic and mass transport controlled. A simple batch reactor under galvanostatic conditions is studied in these experiments. The results, provided by the theoretical macroscopic model, are compared to the experimental results in the second part of this chapter.

Regarding the idea of plating process, this study helps towards better understanding a relationship between the decrease of metal ion concentration and time, with respect to a reduction reaction. Essentially, it leads to identify duration of depositing process when the metal concentration appears too low. The results significantly ease our decision to add more reactant species or to terminate the bath. The time recovery to destroy plating bath at its end of life could also be determined.

2.2 Experiment

The schematic flow diagram of experiment was demonstrated in Figure 2.1.

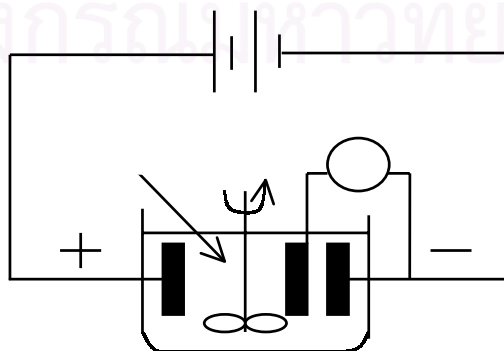


Figure 2.1 Electrochemical batch reactor for copper removal

Basically, the experiment consisted of a cell with static vertical electrodes containing 0.8 L of electrolyte. The cathode was a stainless steel sheet with a surface area of 0.008 m^2 and the anode was titanium sheet coated by ruthenium oxide. The baths were prepared using deionized water and analytical grade of copper sulfate ($\text{CuSO}_4 \cdot 5(\text{H}_2\text{O})$). The initial concentrations of copper were 0.14, 0.4 and 0.5 kg m^{-3} , respectively. The initial electrolyte pH was adjusted to 1 by adding sulfuric acid and measuring by a digital pH meter. Experiments were conducted at 305 K.

Electrodeposition was carried out under a galvanostatic condition at applied current densities ranging from 1.5 A m^{-2} to 62.5 A m^{-2} . Samples were taken by every half of an hour from the electrolyte, and the concentration of copper was analyzed, using an atomic absorption spectrophotometer.

The differences in stirring rates ranging from 0 to 300 rpm, were provided by a stirrer with an anchor paddle of a 5.2 cm diameter to determine the effect of stirring rate on mass transfer coefficient.

To verify the limiting current, the voltammetry operation of copper plating is determined by disk electrode using a Model PGSTAT 30 potentiostat/galvanostat. The disk electrode is made of stainless steel with the surface area of $1.26 \times 10^{-5} \text{ m}^2$, and the anode is a titanium coated by ruthenium oxide sheet. The reference electrode is the saturated calomel electrode.

2.3 Results and Discussions

The experimental results and the modeling are focal points in this part. The studied effects of copper concentration, applied current densities, cathodic potential and stirring rate are considered in the first section. In the second section, the modeling is performed, and a comparison with the experimental results has been made.

2.3.1 Experimental Results

2.3.1a The Effect of Copper Concentration and Applied Current Densities

The influence of the applied current on the effectiveness of electrolysis operation is depicted in Figures 2.2, 2.3 and 2.4 which illustrate the decrease in the normalized copper concentration ($C(t)/C(0)$) plotted against time of electrolysis, using different applied current densities for the two different initial concentrations. The data show that the reduction of copper is sensitive to the applied current. Removal rate increases with the applied current used for the operation. Limiting current estimated values of 21.25, 25 and 37.5 A m⁻² for initial copper concentration of 0.14, 0.4 and 0.5 kg m⁻³, respectively are determined by the first value observing from the experimental curve versus time. These values are closed to those obtained from the voltammetry curve for copper using a potentiostat/galvanostat model PGSTAT 30. The limiting current densities are 19.9, 23.0 and 37.4 A m⁻² for initial copper concentration at 0.14, 0.4 and 0.5 kg m⁻³ respectively.

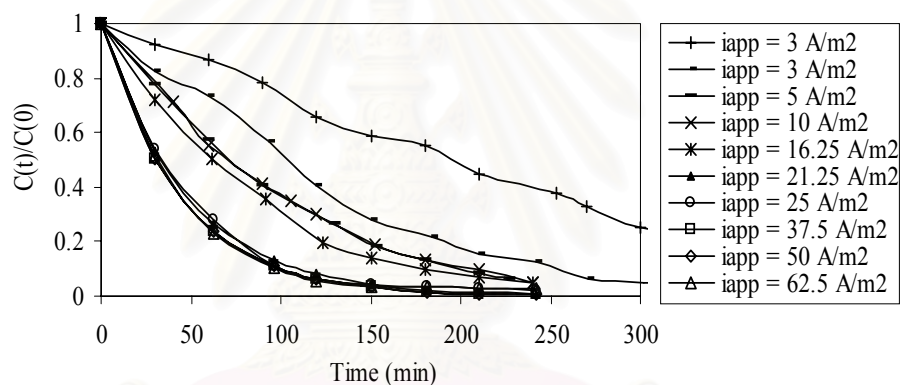


Figure 2.2 Normalized copper concentration against time curve at different applied current densities, with initial concentration of 0.14 kg m⁻³, stirring rate of 200 rpm

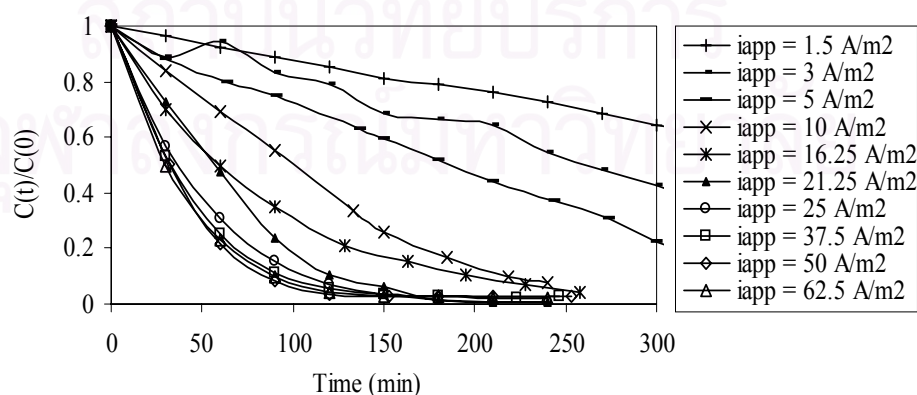


Figure 2.3 Normalized copper concentration against time curve at different applied current densities, with initial concentration of 0.4 kg m⁻³, stirring rate of 200 rpm

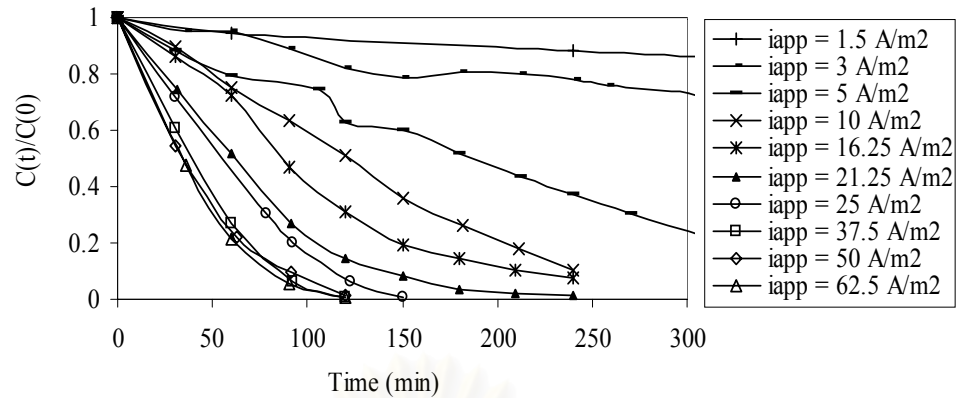


Figure 2.4 Normalized copper concentration against time curve at different applied current densities, with initial concentration of 0.5 kg m^{-3} , stirring rate of 200 rpm

At the low applied current density, linearly decreasing of the concentration versus time is observed whereas decreasing rate is exponential at a highly applied current density. The charge and mass transfer equations are shown by the following equations:

Charge transfer limit:

$$C = C_i - \frac{It}{nFV}$$

Mass transfer limit:

$$C = C_o \exp(-k_m At / V)$$

From the data in Figures 2.2 to 2.4, it can be explained that before the applied current densities reach the limiting current, the overall rate of reaction is controlled by the rate of the electrochemical charge transfer process, which is in turn an activation-controlled process. It seems that normalized copper concentrations drop linearly with time, then it can be affirmed that the reaction is zero order. This gives rise to kinetics controlled that are described by Equation 1.41.

When the applied current exceeds the limiting current, all copper ions that reach the electrode are diminished. This implies fast kinetic, hence the reaction of

copper is controlled by the rate at which ions can reach the electrode. The reaction is mass transfer limited. The limiting current in this period can be defined according to Equation 1.38. It appears that normalized copper concentration drops exponentially with time thus this is the evidence of first order reaction described by Equation 1.44.

2.3.1b The Effect of Cathodic Potential

The variation in cathodic potential with time for different applied currents is depicted in Figure 2.5. At the beginning of the electrodeposition process, the cathodic potential increases with time. The slight increase in cathodic potential at the beginning of the process may be a consequence of the deposition of fresh metal onto the cathode surface (nucleation overpotential). A similar effect has been observed by Stankovic (1995)⁶. After this period, the applied current exceeding the current limit, the cathodic potential falls over a longer period, and then it remains constant. The time for which the cathodic potential falls, corresponds approximately to the time for which the normalized copper concentration departs from its linearity with time. It is supposed that the observation is caused by the hydrogen evolution⁷ when the applied current exceeds the limiting current. This behavior can be explained that once the concentration of copper ion at the electrode surface is zero, the applied current can no longer support the electron transfer reaction of copper, so the potential changes to the redox potential of hydrogen evolution reaction⁸. The falling period of the cathodic potential is shorter for higher applied current.

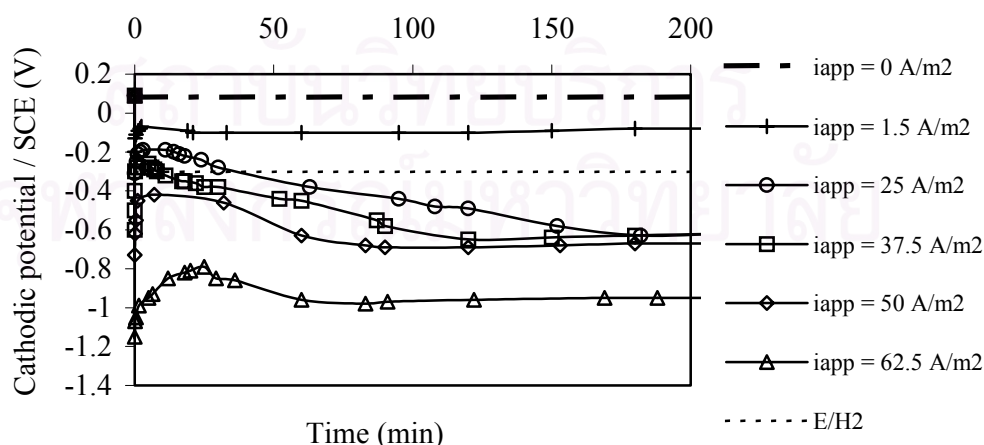


Figure 2.5 A plot of cathodic potential reference saturated calomel electrode against time at different applied currents, and initial copper concentration of 0.4 g dm^{-3}

2.3.1c The Effect of Stirring Rate on Copper Deposition Rate

A number of controlled current electrodeposition processes are carried out at 0.2 A with an initial copper concentration of 0.4 kg m^{-3} for different stirring rates. Such a current is corresponding to the limiting current for an initial 0.4 kg m^{-3} copper concentration. Figure 2.6 shows that the reduction of the metal ions drops exponentially with time and becomes more effective as the stirring rate increases. This is evidence that the process is under mass transfer control⁹⁻¹¹. It is possible to note that the mass transfer coefficient increases with the stirring rate. For higher stirring rate, hydrodynamic condition improves the mass transfer in the cell by reducing the diffusion layer thickness^{12,13} (Table 2.1). The diffusion layer thickness can be calculated by Equation 1.23, the diffusion coefficient used for this system is $6.79 \times 10^{-10} \text{ m}^2 \text{ s}^{-1}$ ¹⁴. Figure 2.6 also shows that stirring rate can be used for the optimization of cell performance, with a clear limiting value of 200 rpm. The experiment is useful for determining the optimum rate used for copper plating. The process should not operate more than 200 rpm for energy saving.

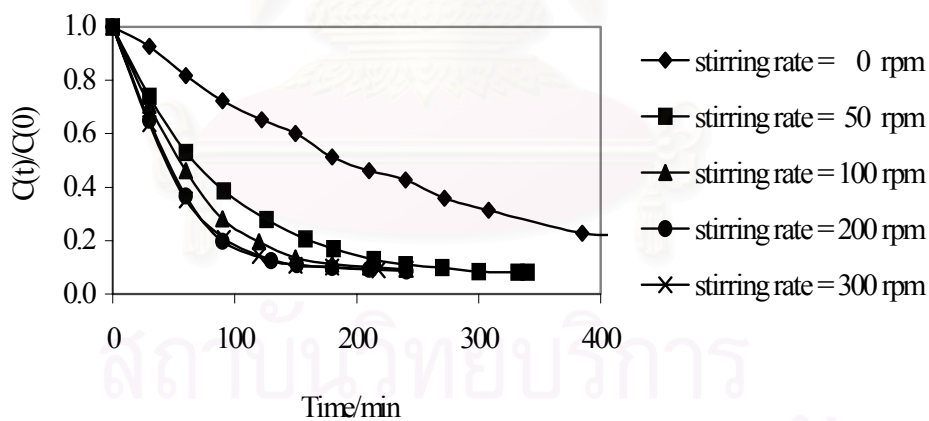


Figure 2.6 Normalized copper concentration against time curve at different stirring rate, initial copper concentration of 0.4 g dm^{-3} and applied current of 0.2 A

Table 2.1 Effect of stirring rate on mass transfer coefficient and diffusion layer thickness

Stirring rate/rpm	$k_m \times 10^5 / \text{m s}^{-1}$	Diffusion layer thickness/ μm
0	0.6	115
50	1.62	43
100	2.17	32
200	2.55	27
300	2.63	26

2.3.1d Conclusion

In the analysis of galvanostatic methods for copper electrodeposition rate using 2 dimensional electrode cells under batch system, it can be concluded that

- (i) The decrease in limiting current and copper concentration with time are depended on the applied currents (in the range from 1.5 to 62.5 A m⁻²) for the electrolysis cell. The current limit values obtained from the range of initial copper concentration from 0.14, 0.4 and 0.5 g dm⁻³ are 0.17, 0.2 and 0.3 A (or 20.9, 24.6 and 37.0 A m⁻² of limiting current density), respectively.
- (ii) Being less than the limiting current, the applied current has an effect on the deposition rate, which is controlled by charge transfer rate.
- (iii) Being higher than the limiting current, the applied current has no effect on the overall rate, which is controlled by mass transfer rate.
- (iv) At different stirring rates, the best performance of copper deposition rate is obtained at 200 rpm.

2.3.2 Macroscopic Model

In the literature review, the relationships of metal ion concentration versus time are analyzed according to charge and mass transfer process. The equations are described below:

$$C(t) = C(0) - \frac{iA_s t}{nFS} \quad \text{Charge transfer} \quad (1.61)$$

$$C(t) = C(0) \exp^{-k_m A_s t} \quad \text{Mass transfer} \quad (1.62)$$

The mass transfer equation can be rewritten in the following form

$$\ln \frac{C(t)}{C(0)} = -k_m A_s t \quad \text{Mass transfer} \quad (1.63)$$

In this section, the copper concentration evolution versus time has been simulated according to Eq 1.61 when the system is assumed to operate under charge transfer limiting. The faradaic current efficiency used in this case is equal to one, thus, the efficient current density is equal to the applied current densities. When the system reaches to the mass transfer control, the copper concentration evolution versus time is thus calculated according to Eq. 1.62. The faradaic current efficiency used in this case is less than one and the efficient current density is equal to the limiting current densities. The criterion to differentiate charge/mass transfer region is the current efficiency.

2.3.2a Determination of the Faradaic Current Densities versus Time

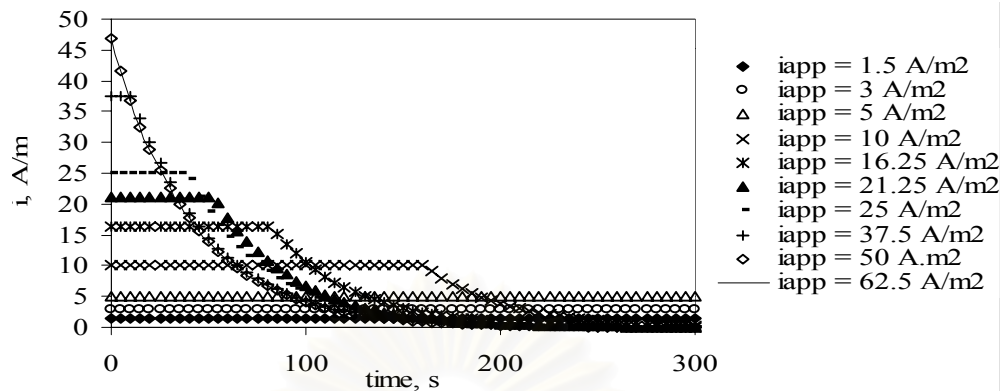


Figure 2.7 Normalized faradaic current densities against time curve at different applied current densities, for initial concentration of 0.5 kg m^{-3} , and stirring rate of 200 rpm

According to the results of the concentration changing with time, the faradaic current densities can be calculated following to Eq. 1.37 and 1.45 for charge and mass transfer, respectively. Figure 2.7 shows that at the applied current densities of 1.5 to 5 A m^{-2} , the faradaic current densities are the same value as the applied current densities. At the applied current densities 10 to 37.5 A m^{-2} , the faradaic current densities are lower than the applied current densities in the longer time observation. In addition, at the applied current densities 50 to 62.5 A m^{-2} , the faradaic current densities are lower than the applied current densities at all the observation time. This behavior means that at the lower applied current densities; the faradaic current densities require 100% of applied current densities for copper plating. While less than 100% are required for the higher applied current densities, the hydrogen evolution, at the higher current densities, is observed.

2.3.2b Determination of the Mass Transfer Coefficient

To simulate the copper concentration versus time, mass transfer coefficient is necessary to be determined from the experimental data. The mass transfer coefficients listed in Table 2.1 are determined from the slope of the logarithmic plot of concentration ratio evolution, $(C(t)/C(0))$, versus depositing time as shown in Eq. 1.44. The slope of this curve corresponds to the value of the mass transfer coefficient multiplied by the specific area, $k_m A_s$.

The average value of mass transfer coefficient is equal to $1.9 \times 10^{-5} \text{ m s}^{-1}$ and determined by keeping the constant stirring rate (200 rpm) at different applied current densities and initial concentrations.

2.3.2c Comparison of Experimental Data and Theoretical Results from the Model

Figures 2.8, 2.9 and 2.10 show the comparison of the results provided by our model to the experimental data obtained in copper concentrations of 0.14, 0.4 and 0.5 kg m^{-3} . It is observed that modeling results fit well with the experimental data especially when the applied current densities reach the limiting current densities ($\sum \text{error}^2 < 0.003$). On the other hand, at the lower applied current densities, deviations have been observed. This difference is caused by the lower current densities applying to the system with inconstant power supply throughout the experiment. It leads to the discrepancies of some concentration points observed in applied current densities of 1.5 and 3 A m^{-2} .

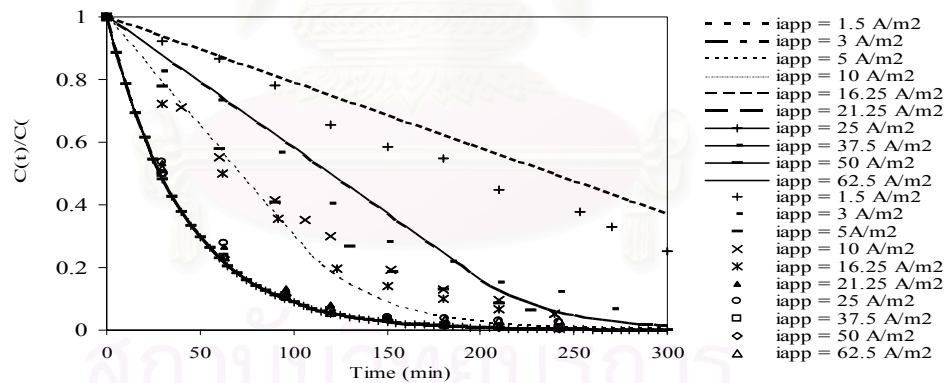


Figure 2.8 A plot of experimental and predicted normalized copper concentrations evolution versus time at different applied current densities, initial concentration of 0.14 kg m^{-3} , and stirring rate of 200 rpm. The lines stand for the model results and the marked points for the experimental data. The limiting current density is 20.9 A m^{-2} .

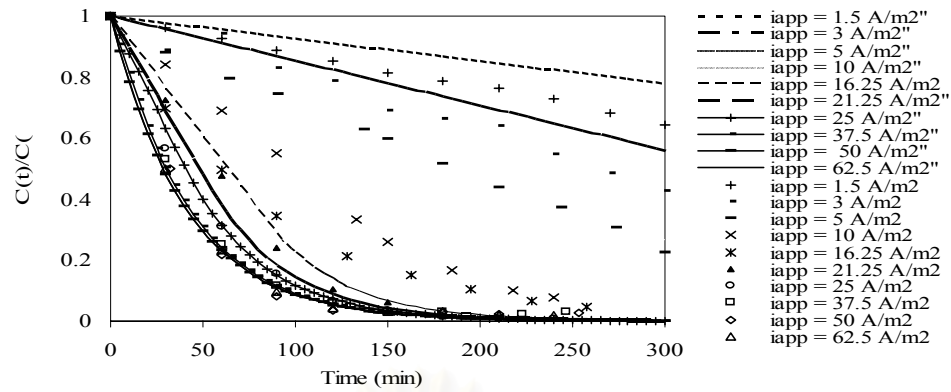


Figure 2.9 A plot of experimental and predicted normalized copper concentrations evolution versus time at different applied current densities, initial concentration of 0.4 kg m^{-3} , and stirring rate of 200 rpm. The lines stand for the model results and the marked points for the experimental data. The limiting current density is 24.6 A m^{-2} .

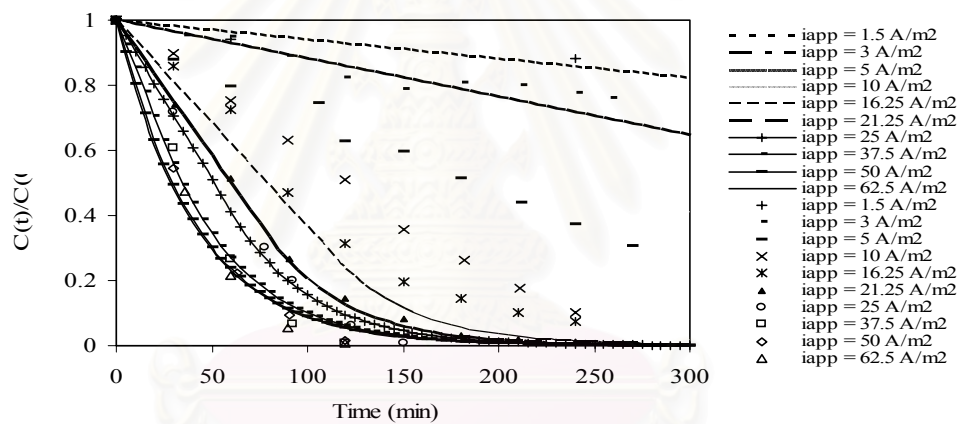


Figure 2.10 A plot of experimental and predicted normalized copper concentrations evolution versus time at different applied current densities, initial concentration of 0.5 kg m^{-3} , and stirring rate of 200 rpm. The lines stand for the model results and the marked points for the experimental data. The limiting current density is 37 A m^{-2} .

2.3.2d Conclusion

According to the results of model simulations in this section, it can be concluded that the theoretical model can fit well with the experimental data, especially at the mass transfer control region, $C(t) = C(0) \exp(-k_m A_s t)$. The average mass transfer coefficient determined for all experiments performed at 200 rpm is equal to $1.9 \times 10^{-5} \text{ m s}^{-1}$.

The application of this model is to monitor the decrease in concentration versus time. As the concentration decreases, the properties of the bath are also changed with time, diminishing the quality of the deposit. According to the model, time duration, related to the lower concentration of reacting species in the bath, is determined. This will guide towards an appropriate time of adding species into the bath, to maintain their required concentration.

Conclusion

The general theory of the electrochemistry dealing with the charge transfer, mass transfer and the electrochemical reactor, has been analyzed in the bibliography part, chapter 1. The macroscopic model is used to investigate concentrations of metal species at the bulk electrolyte versus time according to the role of charge and mass transfer in the batch reactor.

In this part, the bulk concentration, in relation to efficient current, is monitored versus time. The different characteristic of concentration evolution depends on the type of electrochemical reactor. These characteristics can be applied for the electrochemical process of metal recovery, and determined for time duration of plating process and electrosynthesis.

The macroscopic model is not sufficient to explain the electrochemical mechanism dealing with the reaction phenomenon on the electrode surface. In doing so, the microscopic model is required and analyzed, as will be described in the part 3.

PART 2

ANALYSIS OF THE CURRENT DISTRIBUTION IN DIFFERENT ELECTROPLATING REACTORS

Introduction

Electrochemical plating is used to give a particular surface property to a component. This can be a decorative aspect (silver, gilding), a physical or mechanical property different from an existing one (hard chromium), or a protection against corrosion (nickel and chromium). The operating condition has an effect strongly on the properties of the deposit. The current density is able to affect the morphology and composition. It is often purposely carried out under **non-uniform** current distribution, using electroplating test cells. In a single experiment, electroplaters can thus study the effect of a wide range of current densities on deposit morphology and composition, to save time¹³.

This section is composed of two main chapters. The first one concerns the bibliography dealing with the different kinds of current distribution and Wagner number, and the different kinds of electroplating reactors used in the electroplating industry. The advantages and disadvantages of these electroplating reactors are also discussed. **The second chapter presents the experimental investigation consisting of the current distribution in two particular reactors, the Mohler cell and the Rotating Cylinder Hull cell.**

CHAPTER I

Bibliography

1.1 Mass Transport and Current Distribution

The uniformity, microstructure and composition of electroplated metals and alloys depend not only on kinetic and thermodynamic factors, but also on mass transport and current distribution conditions at the cathode. An important goal of metals alloy depositions studies is the development of predictive models in relationship of operating conditions to alloy composition and structure. Therefore, it is useful to distinguish different electrochemical phenomena according to the length scale (distance from the model surface to the bulk solution) involved as schematically shown in Figure 1.1.

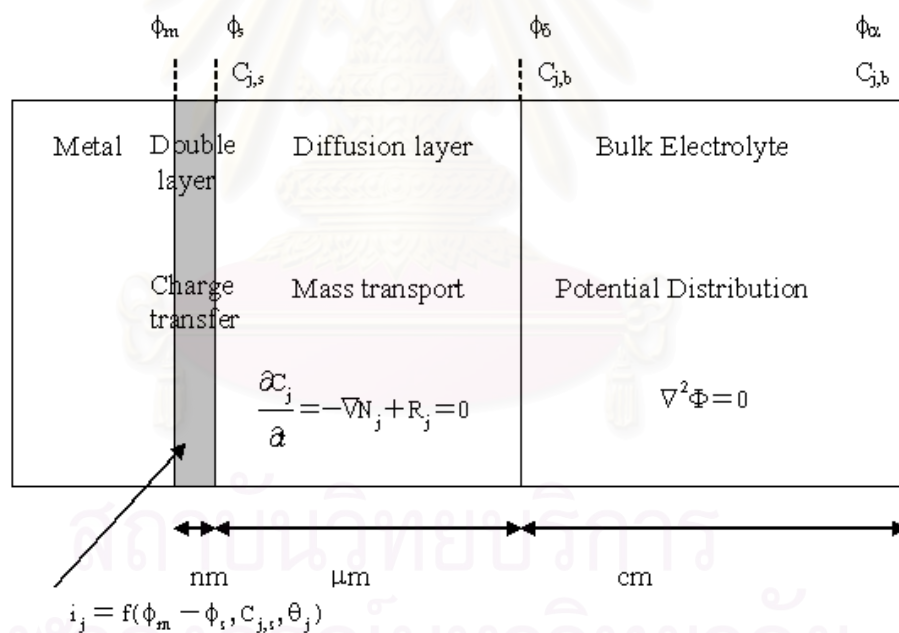


Figure 1.1 Length scales of electrochemical phenomena entering into theoretical modeling ¹³

Charge transfer reactions are responsible for the formation of metallic deposits at the metal electrolyte interface. Their characteristic length is on the order of two to three nanometers, corresponding to the thickness of the electrical double layer. The partial current density i_j of species j is a function of its overpotential (η_j) and its concentration at the electrode surface ($c_{j,s}$). In addition, i_j may depend on the surface

coverage θ_j of different electrolyte species, or reaction intermediates adsorbed on the surface.

$$i_j = f(\eta_j, c_{j,s}, \theta_j) \quad (1.1)$$

For a given applied current or cell voltage, the value of the local current density i_j at the cathode may be influenced by mass transport conditions and by the potential distribution in the bulk electrolyte.

The characteristic length for mass transport corresponds to the thickness of the diffusion layer and is typically on the order of a few micrometers. This is much larger than the double layer thickness, and for this reason charge transfer kinetics enter as a boundary condition into theoretical models when consideration of mass transport phenomena near the cathode. According to the Nernst diffusion layer concept, a stagnant diffusion layer is assumed to exist near the electrode, and mass transport in this region proceeds due to diffusion and migration only. For each species j , a mass balance equation can be formulated, which may include a variation of time dependent concentrations and chemical reaction R_j .

$$\frac{dC_j}{dt} = -\nabla N_j + R_j \quad (1.2)$$

At the steady state, outside the diffusion layer, the electrolyte concentration is uniform. The potential distribution in the electrolyte in this case can be calculated from the Laplace equation.

$$\nabla^2 \phi = 0 \quad (1.3)$$

From the potential distribution, the current density at each point is evaluated using Ohm's law. The characteristic dimension for the potential distribution is that of the electrochemical cell, typically in the centimeter range. This is much larger than the diffusion layer thickness. As a consequence, current distribution calculations based on Laplace's equation are linked with electrode kinetics.

A non-uniform potential distribution in the electrolyte normally leads to a non-uniform current distribution on the cathode. Three cases can be distinguished, Firstly, if the influence of electrode polarization and mass transport is unimportant, the so called primary current distribution prevails, which depends only on the geometry of the electrochemical cell. Secondly, in the absence of non-negligible electrode polarization, the so-called secondary current distribution prevails. The uniformity of the current density on the cathode, in this case, depends on cell geometry and on the value of electrode polarization. Wagner number (W_a) expresses the ratio of the polarization resistance at the interface over the ohmic resistance in the electrolyte.

$$W_a = \frac{d\eta/di}{\rho_e L} \quad (1.4)$$

Here ρ_e is the electrolyte resistivity ($\Omega \text{ m}$) and L is a characteristic length of the system (m). The secondary current distribution is always more uniform than the primary current distribution. Under conditions where the polarization resistance becomes dominating, *ie* when the Wagner number goes to infinity, the current distribution on the cathode becomes perfectly uniform, independent of cell geometry. The primary current distribution corresponds to Wagner number approaching to zero, which is attained when $\rho_e L$ is high. Finally, in presence of significant mass transport and polarization effects, the tertiary current distribution prevails. The current distribution on the cathode in this case will depend on both the potential distribution and the local rate of mass transport and geometry of the cell ¹⁴.

In alloy deposition more than one electrode reaction takes place. The relative importance of potential distribution and mass transport may then differ for the different components. In such a case not only the global current distribution is of interest, but also the distribution of partial current densities, which describe the reaction distribution for the different components. While a non-uniform current distribution in a single metal plating leads to a locally varying film thickness, a non-uniform reaction distribution in alloy plating different structure deposit, leads to a locally varying composition.

Because the local rate of an electrode reaction depends not only on charge transfer kinetics, but also on mass transport and current distribution, all three phenomena must be taken into account on theoretical modeling of alloy plating and in the design of experiments. This means that laboratory studies on alloy deposition should be carried out under controlled hydrodynamic and current distribution conditions at the cathode.

1.2 Cells with Controlled Non-Uniform Current Distribution

In general, electroplating operations are performed over a broad range of hydrodynamic conditions. In some instances, as in barrel plating, the liquid moves slowly relative to the work piece. While in jet plating, used in strip plating operations, the solution moves at speeds up to several meters per second. Further electroplating processes encounter a wide range of current densities.

When using a controlled non-uniform current distribution cell, one must bear in mind that under secondary current distribution conditions, i.e. with increasing the effect of the electrode polarization, the current density becomes more uniform and the empirical formulas for estimating the current no longer apply. Figure 1.2 shows the effect of electrode polarization (expressed by the value of the Wagner number) on current distribution, assuming Tafel kinetic¹³. Also shown (broken line) is the primary current distribution, which corresponds to a Wagner number of zero. At high Wagner number ($Wa \gg 1$) the current distribution becomes uniform.

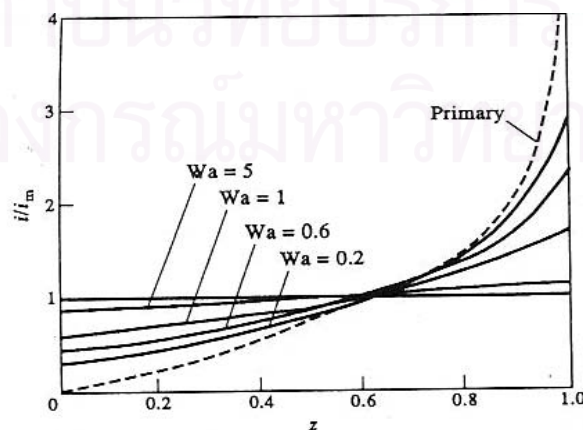


Figure 1.2 Secondary current distribution in the Hull cell calculated for different values of Wagner number assuming Tafel kinetics. Dashed line indicates primary current distribution¹³

1.3 Review of the Electroplating Test Cell

1.3.1 Hull Cell [R. O. Hull, 1939]¹⁴

The Hull Cell was developed by R.O. Hull in 1939¹⁴. The main property of the Hull cell (Figure 1.3) is its ability to deposit a metal over a wide range of current densities at a fixed total current. One design feature of the Hull cell is the acute angle and relative longer distance between the anode and the cathode at one end of the cell. This provides the characteristic field variation, which combined with the shielding effect of the cell wall, results in low current density at this end. From this position, the current density increases gradually, reaching its maximum at the obtuse angle end where the shielding is minimal and the anode-cathode distance is the shorter, resulting in the highest current density. Hull defined a logarithmic relation, which describes the current distribution for a typical 267 mL Hull cell:

$$\text{Current Density (CD)} = I(0.105 - 0.051 \log L) \quad (1.5)$$

Where current density is in amperes per square meter (A m^{-2}). I is the total current in amperes, and L is the position on the panel in inches from the low-current density end.

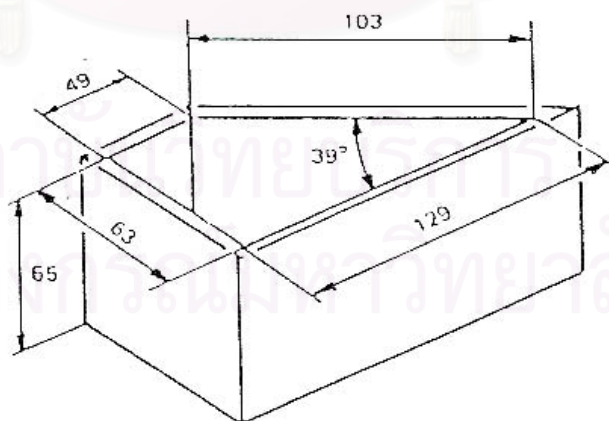


Figure 1.3 Standard Hull cell, dimension indicates in mm

Figure 1.4 shows the theoretical current density distribution versus the distance along the Hull cell panel for a total applied current of two amperes. Thus one can preview the performance of a particular plating chemistry over a large range of current densities in a single test¹³.

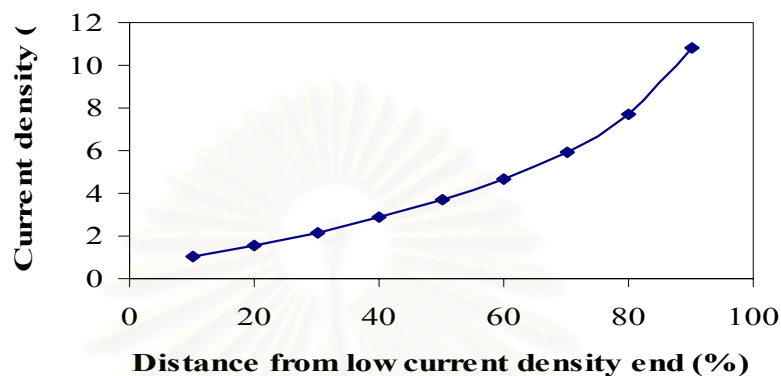


Figure 1.4 Standard Hull cell theoretical current density distribution at 2 A total current¹⁵

Interpretation of the Hull cell patterns has developed into an art. This is understandable since, in most instances, the electrodeposition is obtained under poorly controlled hydrodynamic conditions defined as low, medium, or high and performed by a magnetic stirrer, a reciprocating paddle, or manual stirring. Under such conditions, it is difficult to quantify or reproduce the experiment, and interpretation becomes subjective and often arguable¹⁵. The Hull cell is convenient when we operate in a charge transfer rate.

Finally, and most importantly, many modern electroplating cells employ liquid velocities of several meters per second¹⁶, while a typical Hull cell can only attain velocities of 20 to 30 cm/sec. Therefore, information obtained under moderate agitation is not directly applicable to high-speed processes. In summary, the applicability of the conventional Hull cell is limited for the following reasons:

- Lack of well-defined and reproducible hydrodynamics.
- Inability to provide high-speed solution agitation.
- Inability to attain high current densities.
- Non-uniform vertical current distribution at specified current densities.

To overcome this problem, several authors have proposed modified Hull type cells that include controlled hydrodynamic conditions allowing an enhancement of mass transfer in the Hull cell or other types of test cell. In those studies, a rotating electrode, in the form of a cone or cylinder, was employed to provide well-defined hydrodynamics and increase the magnitude of operating cathodic current densities. The presentation of this cell constitutes the part of this work.

1.3.2 Hydrodynamically Controlled Hull Cell (HCHC) [I.Kadija, 1991]¹⁵

The HCHC proposed by Kadija¹⁵ and all utilizes a rotating cylinder to control the mass transfer conditions accurately while applying a current density range typical of a conventional Hull cell. This geometry provides continuous variation in anode to cathode distance as one moves from the circular anode up along the shaft of the rotator i.e. the cathode. The core of the instrument is schematically represented in Figure 1.5.

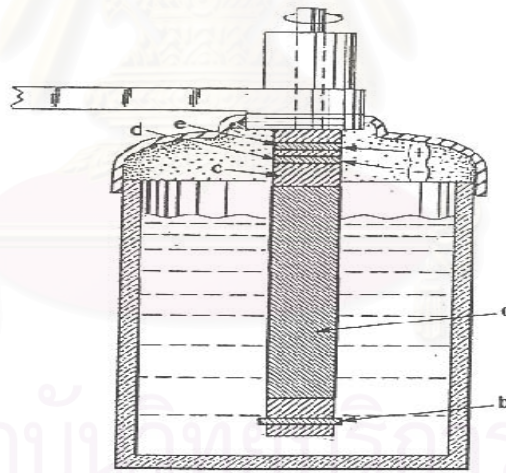


Figure 1.5 Hydrodynamically Controlled Hull Cell: (a) Cathode, HCHC panel; (b) Anode (c) Rotating cylinder body, insulated; (d) Cathode slip ring; (e) Anode slip ring¹⁵

A baffle is used to modify the electric field in a controlled manner. Geometries similar to the Hull cell were considered, such as the cone-shaped baffle shown in Figure 1.6.

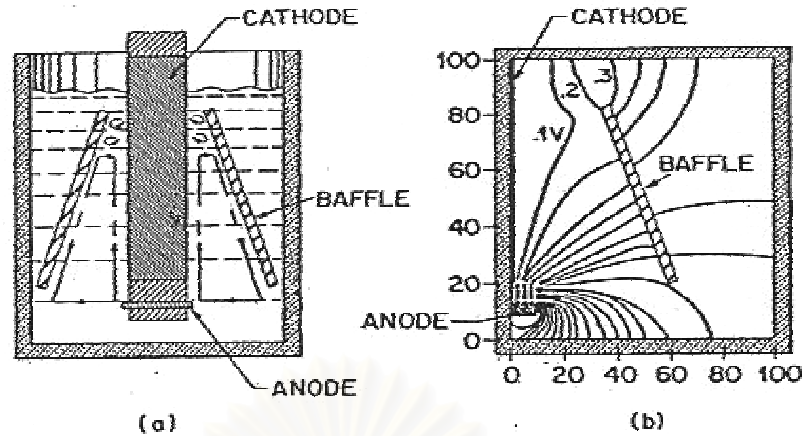


Figure 1.6 Hydrodynamically Controlled Hull cell: (a) HCHC, partially submerged with one baffle; (b) Equipotential line distribution calculation; two-dimensional representation of the cell: vertical distance from cell bottom; horizontal distance from cathode surface¹⁵

1.3.3 The Lu Cell [Po-Yen Lu, 1991]¹⁷

Lu¹⁷ proposed several designs using conical and cylindrical electrodes. The basis of this rotating Hull cell design is the combination of the current density variation feature of the classic Hull cell and the reproducible mass transfer feature of a rotating electrode. In other words, the rotating Hull cell design consists of a current restricting shield (usually forming a less than 90 degree angle with the cathode), a rotating cathode, and an anode (either stationary or rotating). Based on the above principle, many versions of rotating Hull cells may be designed as for an example in rotating cone cathode and a stationary disk anode as shown in Figure 1.7.

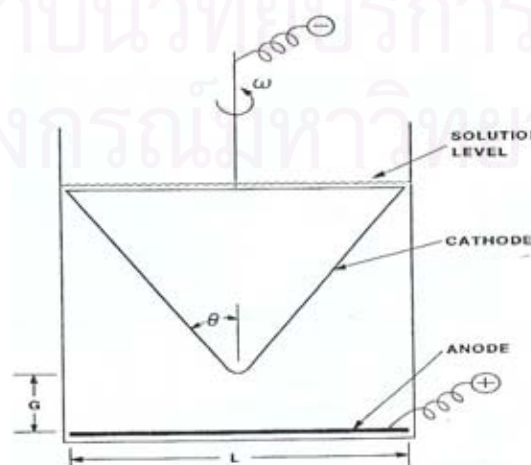


Figure 1.7 Rotating disk cathode and stationary cylinder anode¹⁷

In this design, the variation of the current density along the cone can be obtained by adjusting the gap (G) between the tip of the cone and the anode, the diameter of the anode (L) and the angle of the cone (θ).

The thickness distribution of the deposit versus the length of the cathode is plotted in Figure 1.8. As in the conventional Hull cell, a very wide range of current densities is achieved. θ is the angle of the cone and ω is the rotation rate.

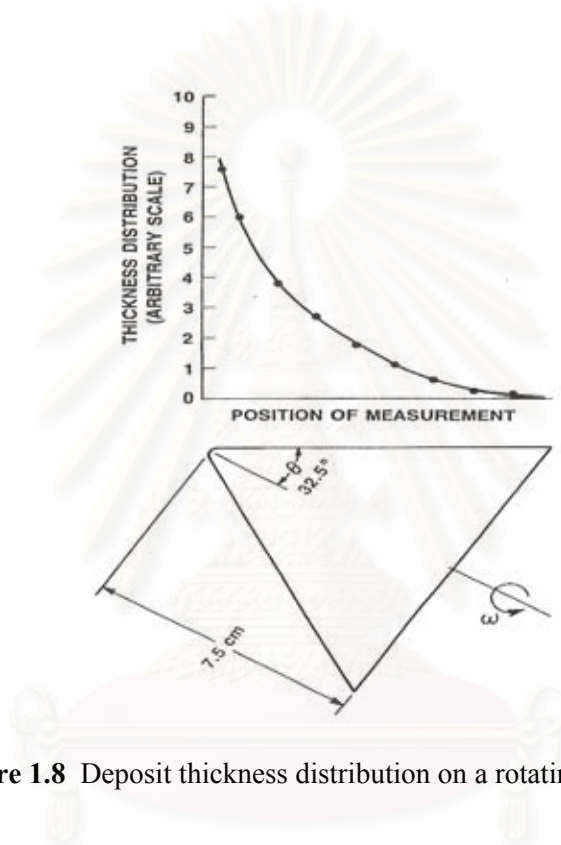


Figure 1.8 Deposit thickness distribution on a rotating cone surface¹⁷

1.3.4 Hydrodynamic Electroplating Test Cell (HETC) [Shi-Chern Yen and I-Mon Lu, 1994]¹⁸

The HETC proposed by Shi-Chern Yen and I-Min Lu¹⁸ is sketched in Figure 1.9. The surface of the rotating cylinder is insulated. The two electrodes can be set at any angle, 90° in this case. The region enclosed by the two electrodes and the rotating cylindrical surface is a sector called the reaction zone. The radius of the rotating cylinder is 2.5 cm, and the width and height of the electrodes are 10 and 6.5 cm, respectively. The geometry of the HETC provides continuous variation in solution resistance between electrodes in the outward direction from the surface of the rotating cylinder. During electroplating, metal deposition is possibly limited by mass transfer,

which may dominate the structure of the deposit, at the region of high current density. Therefore, this HETC was developed to enhance the mass transfer of metal ions and retain the feature of current density variation of the traditional Hull cell. The dimensionless current distribution (i/i_m) along the cathodic surface can be derived analytically, and is expressed as

$$\frac{i}{i_m} = \frac{(R_2 - R_1)}{\ln(R_2 / R_1)} \frac{1}{R_1 + x} \quad (1.6)$$

where R_1 is the radius of the rotating cylinder, R_2 is the radius of the outer cylindrical surface in the plating zone, and x is the position on the cathodic plane away from the inner cylindrical surface that is at the high current density end. The quantity i_m is the average current density across the test panel. In the work presented by Shi-Chern Yen and all, R_1 and R_2 are respectively equal to 23 mm and 125 mm and the volume of HETC is 267 ml.

The HETC employs two planar electrodes that serve as cathode and anode. The longer the cathode, the wider the range of current densities provided by the HETC.

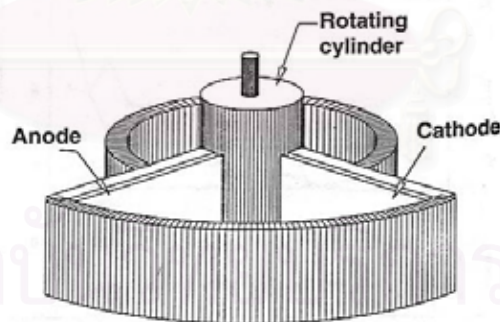


Figure 1.9 The hydrodynamic electroplating test cell¹⁸

A comparison of thickness distribution between the 267 ml Hull cell and the HETC, with electrolyte not agitated, is shown in Figure 1.10. The charge passed through the electrolytic cells is 2000 Coulombs, and the total current applied to the cells is 0.5 A. Variations are a little bit lower for HETC, however this cell is better in the hydrodynamic condition.

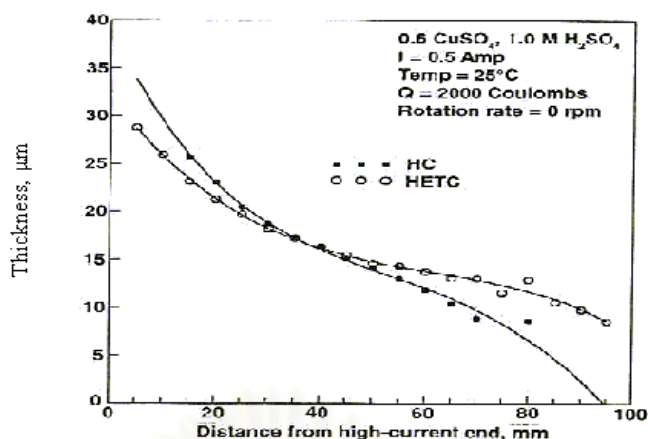


Figure 1.10 The thickness and current distributions for the Hull cell and the hydrodynamic electroplating test cell (HETC) without agitation¹⁸

1.3.5 Rotating Cylinder Hull Cell (RCH) [C. Madore & D. Landolt, 1993]

19

RCH developed by C. Madore and D. Landolt¹⁹ consists of a rotating cylinder electrode partially shield by a tube made of an insulating material, usually plexiglass. The tube is open at one side, either at the top or at the bottom (Figure 1.11). The current lines enter asymmetrically through the open end of the tube, yielding a highly non-uniform primary current distribution on the cathode. Through numerical optimizations of the cell geometry, the primary current distribution on the cathode can be made close to that of the classical Hull cell. The mass transport conditions at the RCH cathode are those of a conventional rotating cylinder electrode, which means that the limiting current density is uniform, and can be varied by varying the rotation rate.

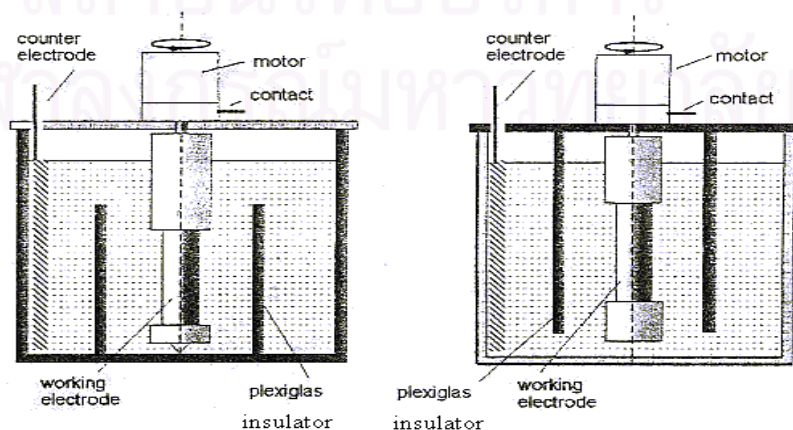


Figure 1.11 Rotating Cylinder Hull (RCH) cell for electrodeposition studies

1.3.6 Mohler Cell [L. Lacourcelle, 1997]²⁰

The Mohler cell, which is proposed by L. Lacourcelle²⁰, is sketched in Figure 1.12. It is a rectangular cell with a plastic screen placed between the cathode and anode, and perpendicular to the potential direction.

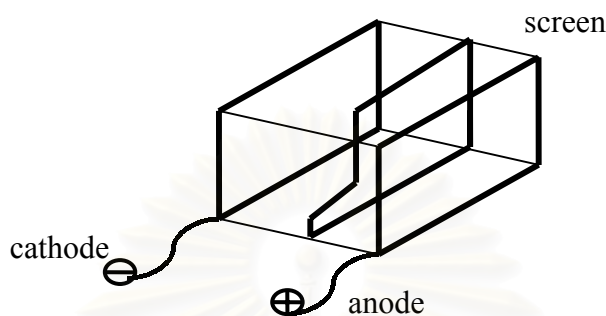


Figure 1.12 The modified Mohler cell with forced electrolyte flow

In the Mohler cell, the current distribution depends on the shape of the insulator. The one slit along the side of the screen, gives a logarithmic current distribution along the cathode. The other insulator containing three slits provides a linear current distribution. In this case, there is no mass transfer system, so the modified Mohler cell is developed to provide a flow in the cell in next chapter.

1.4 Conclusion

According to the literature reviews of the electroplating test cell, the current distribution has an effect on the morphology and composition. To investigate the current distribution, the electroplating test cell is applied to perform an experiment. In the next chapter, the Mohler cell and the RCH are investigated. For Mohler cell, it is easier to model the hydrodynamic condition, because of the flow through cell of the electrolyte. The RCH mass transfer system is the rotating speed and more difficult to model. The Mohler cell is therefore previously performed, and if the investigation of the current distribution is not completely successful, the RCH is analyzed later. The both testing cells are overcome the mass transfer problem in the Hull cell which will be explained in the following chapter.

CHAPTER II

Experimental Investigation of the Current Distribution in Mohler Cell and Rotating Cylinder Hull Cell

2.1 Introduction

Two electroplating test cells have been proposed and tested in order to analyze the performance of plating solutions in electroplating processes. The current distribution on the cathode during deposition of copper electrolyte is discussed.

The first one is a modified Mohler cell composed of a rectangular electrolytic cell with forced electrolyte flow and two flat electrodes. In this study, an insulating separator is inserted between the cathode and anode. This screen modifies the electric field distribution and leads to a non-uniform current distribution or deposit thickness on the cathode panel.

The other one is a Rotating Cylinder Hull cell consisting of an inner rotating cylinder electrode coaxial with a stationary outer insulating tube to produce a non-uniform current distribution along the cylinder cathode.

Both Mohler cell and Rotating Cylinder Hull cell are developed to overcome the absence of controlled mass transport condition in the traditional Hull cell.

2.2 Experiment

2.2.1 Original Mohler Cell²⁰

In the Mohler cell, the current distribution depends upon the shape of the insulator. The one slit along the side of the screen, gives a logarithmic current distribution along the cathode. The other insulator contains three slits providing a linear current distribution. As shown in [Figure 2.1](#) (a), the screen was placed between the electrodes at 25 mm from the cathode, and 50 mm from the anode. The different

insulation screens modify the electrical field along the two electrodes resulting in different types of current distribution on the electrodes.

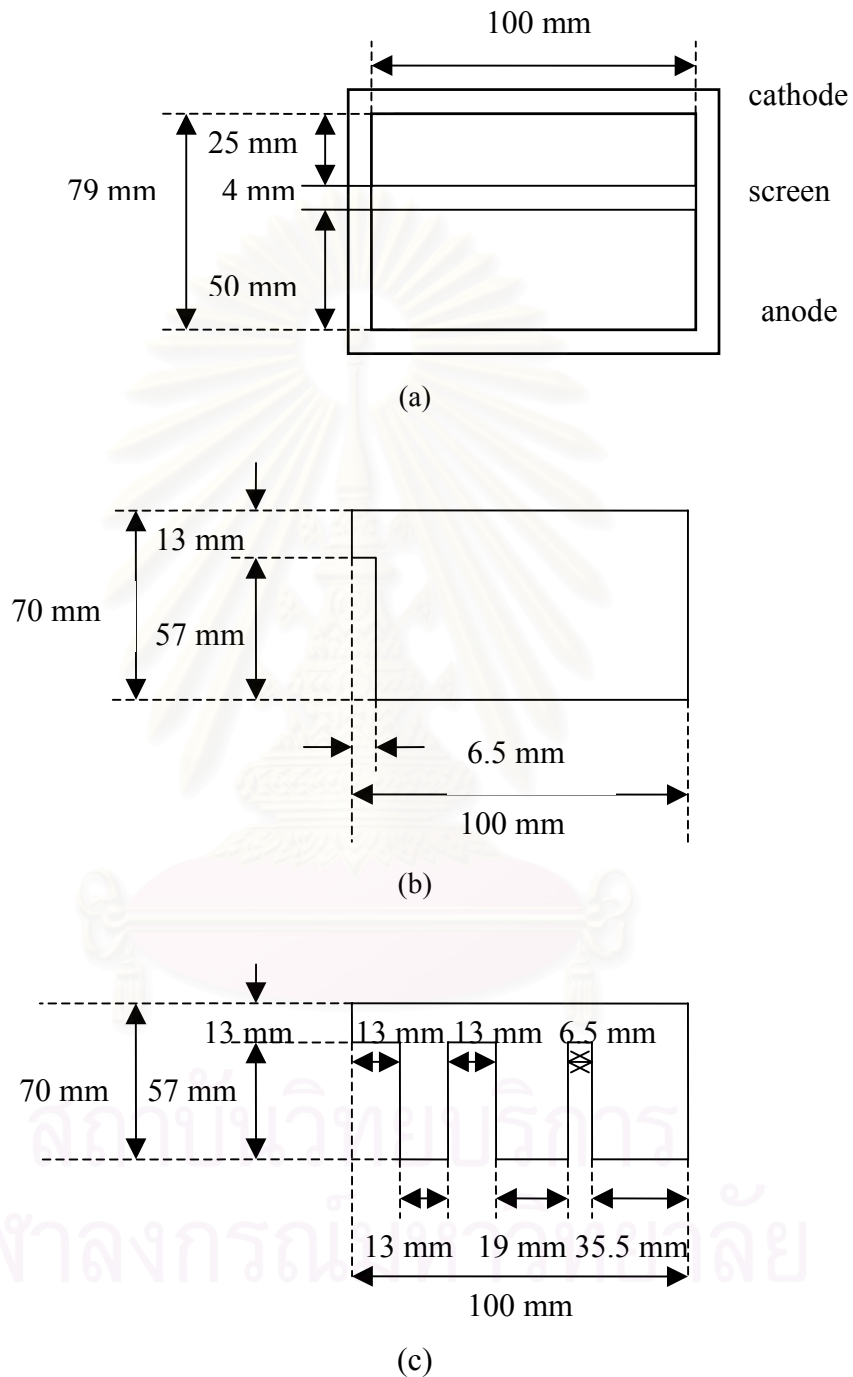


Figure 2.1 Schematic of the Mohler cell (a) Top view of the Mohler cell (b) The screen with one slit along the side (c) The screen with three slits²⁰

2.2.2 Modified Mohler Cell

Mass transfer conditions could have a strong effect on deposit properties. Accordingly, providing reproducible mass transfer condition, which can result from a well-defined hydrodynamic flow, is important for assessing an electrolyte performance. Consequently, the uniform mass transfer to the electrode in the modified Mohler cell will be provided by flowing the electrolyte through the cell parallel to the electrodes according to Figure 2.2. Two opposite side walls of rectangular cell are therefore open to let the forced electrolyte flow.

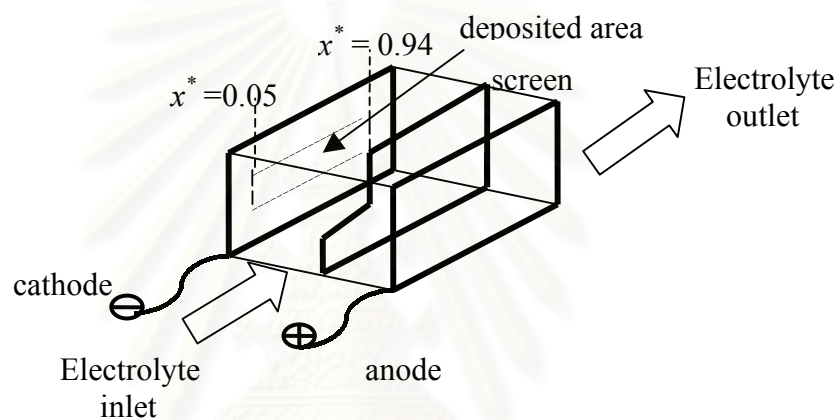


Figure 2.2 The modified Mohler cell with forced electrolyte flow

As shown in Figure 2.3, the experimental device is comprised of a 10 liters electrolytic tank (T), one centrifugal pump (P), the electrolytic cell, 79 mm height, 70 mm width and 100 mm long (C) and two 0.7 meters long adaptive channels (A) to pass from the circular section of the pipes to the rectangular section of the cell and to ensure a fully developed flow in the cell.

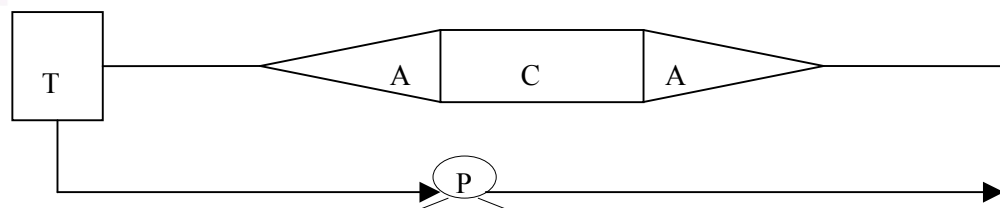


Figure 2.3 Electrolyte circuit (T) electrolytic tank; (A) adaptive channel; (C) electrolytic cell; (P) centrifugal pump

The electrical circuit included a 10 A - 30 V., regulated DC power supply ZS 3205 (PHILIPS). The cathode was a stainless steel sheet. The anode was a Ti/RuO₂ grid with an active area of 52.5×10⁻⁴ m². The cathode had an area of 70×10⁻⁴ m² with the deposited area of 27 ×10⁻⁴ m², as seen in [Figure 2.2](#). The deposited area (27 ×10⁻⁴ m²) taking into account in this study corresponds to the upper part of the cathode because previous works have shown that uniform deposition is obtained on this area²¹.

Analytical grade chemicals were used to prepare the electrolyte solutions. The copper sulfate bath contained 37 g dm⁻³ Cu²⁺, using H₂SO₄ for adjusting pH to 4. The solutions were kept at temperature of 25 °C. Copper deposits were obtained by constant current densities at 0.22, 0.30 and 1.11 mA mm⁻². The electrolytic flow rate was 0.7 dm³ s⁻¹.

A high copper concentration was used to minimize the influence of mass transport, and acid concentration was used to increase solution conductivity and prevent oxide formation at the anode. Current efficiency for copper deposition, as measured by weight gain experiments, was found approximately 100 % for all deposits.

2.2.3 Determination of the Local Current Density

The current density is related to the mass deposit through Faraday's law.

$$i^*(x^*) = \frac{i(x^*)}{i_{ave}} = \frac{nFW(x^*)}{Mt} \quad (2.1)$$

$$x^* = \frac{x}{L} \quad (x^* \text{ is the dimensionless length})$$

where M is the atomic weight of copper (63 g mol⁻¹), n is copper valence, F is Faraday's constant (96484.6 C mol⁻¹), t is time (s), and W is the weight of the deposit (g). For a current efficiency of 100 percent, the dimensionless current density $i(x^*)/i_{ave}$ corresponds exactly to the value of $W(x^*)$. The star represents the normalized value.

The deposition area is defined from the resin application. Before the deposition process occurred, the cathode was coated using resin, except the deposited area. After electrolysis, the copper content on the deposited area was protected by coating with a resin, and divided into 9 samples of the same surface (samples 1 to 9, see Figure 2.4). The resin of the sample part 1 was firstly removed by trichloroethylene and then the copper deposit was dissolved in nitric acid before determining copper content of this solution by atomic absorption spectrometry. Sequentially, analysis process was repeated for each sample.

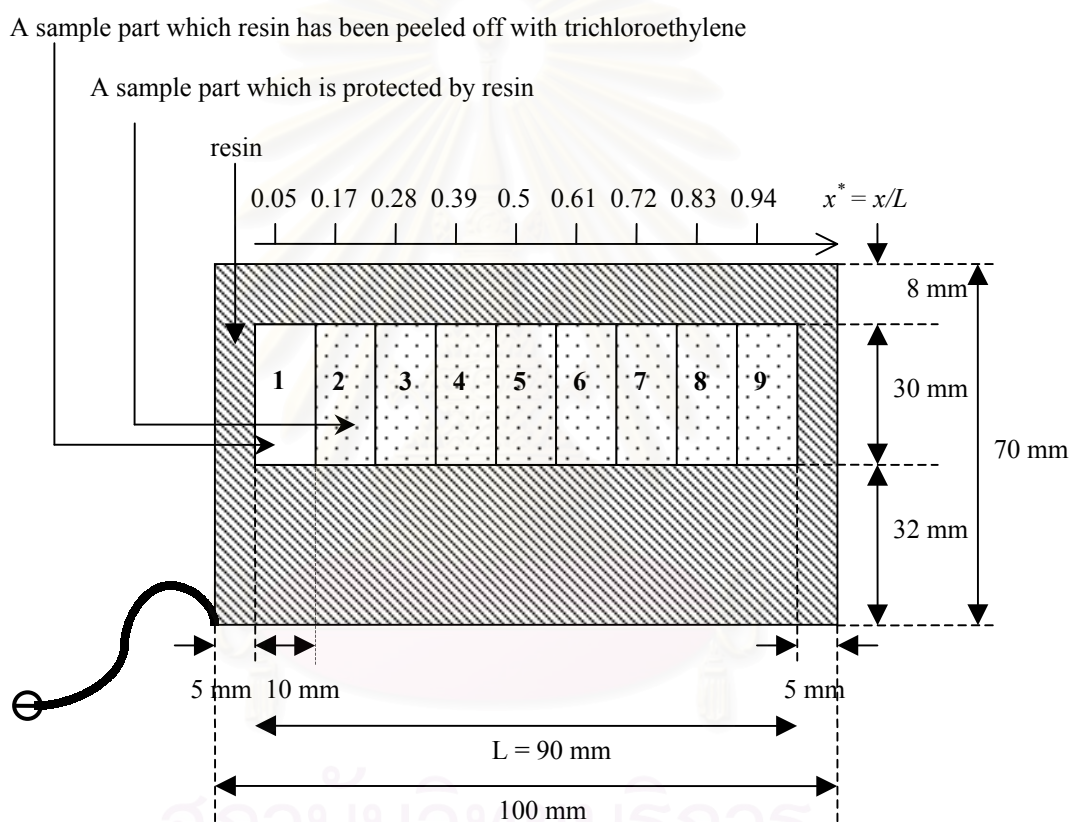


Figure 2.4 Partition of copper deposit on cathode surface of the Mohler cell

2.3 Results and Discussions

2.3.1 Current Distributions in the Mohler Cell

In order to verify the linear current distribution in the Mohler cell, the three slits screen was used. Figure 2.5 shows the experimental dimensionless current density ($i(x^*)/i_{ave}$) versus the dimensionless length ($x^* = x/L$) along the cathode for different total applied currents, i_{ave} correspond to the average current density corresponding to the ratio of the total current intensity over the deposited area. From this figure, it is apparent that the metal distribution along the length of the cathode decreases from the inlet to the half of the cell, and an increase in the observed current occurs beyond this point.

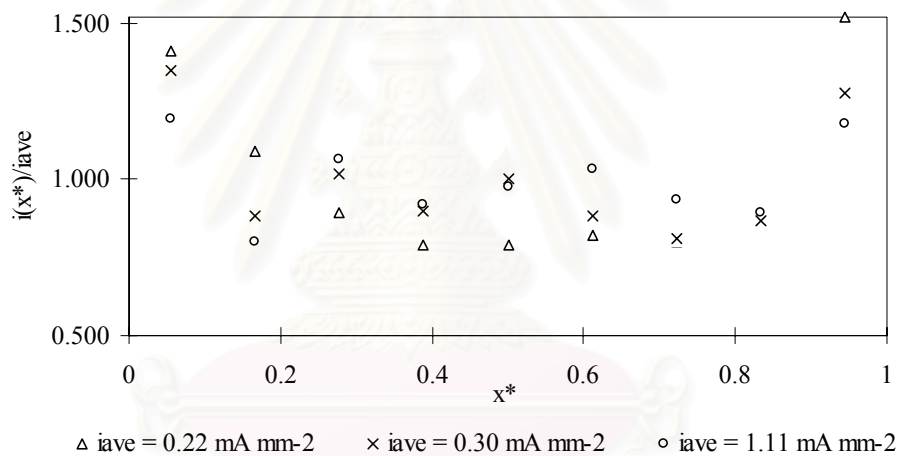


Figure 2.5 Dependence of dimensionless current density distribution versus dimensionless distance for various average current densities

The variation of current density versus the reduced distance does not produce a linear current distribution. The local current density is found to vary within a range from about 0.18 to 1.33 mA mm⁻² for average deposition current densities ranging from 0.22 to 1.11 mA mm⁻². It is found that the ratio of the maximum (obtained at $x^* = 0.05$) to the minimum dimensionless current density (corresponding to $x^* = 0.5$) is only 2. Thus, the current variation at the cathode does not have a wide range for each average current studied. In addition, there is border effect at the inlet and outlet of the cathode, that is clearly seen by the increasing of current at $x^* = 0.05$ and 0.94 respectively.

To further understand the results of this kind of current distribution behavior in the modified Mohler cell, simulation of the primary current distribution in this cell was made. A more detailed discussion on assumptions and limitation of the model in this study have been given elsewhere ^{22, 23}.

The comparison between experimental data and the primary current distribution derived by employing the Laplace 's equation is shown in Figure 2.6. The simulation results confirm that the current variation is not linear, and that also border effects are observed. Results do not present an obvious difference between the maximum and the minimum end of the dimensionless current density, which are due to the border effects. The simulation result presents a little higher value at $x^* = 0.05$ comparing to those obtained at $x^* = 0.94$, but the difference between the both values is low. In other words, the border effects are higher than slits effects.

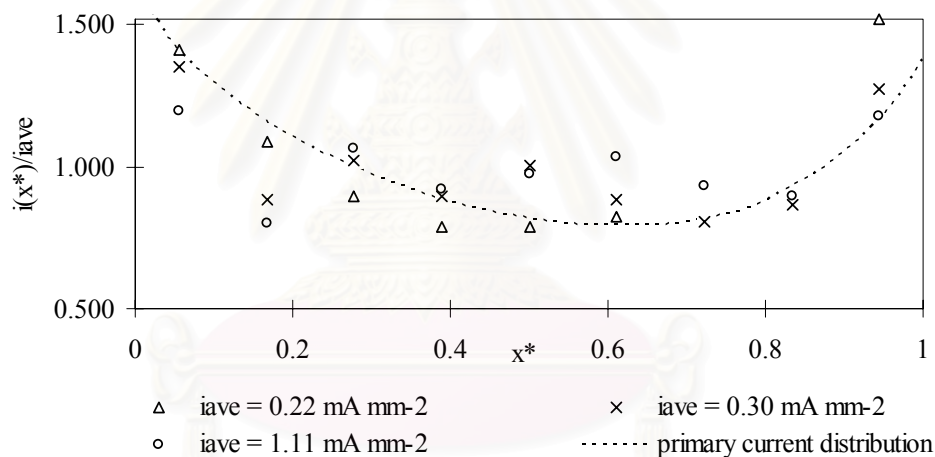
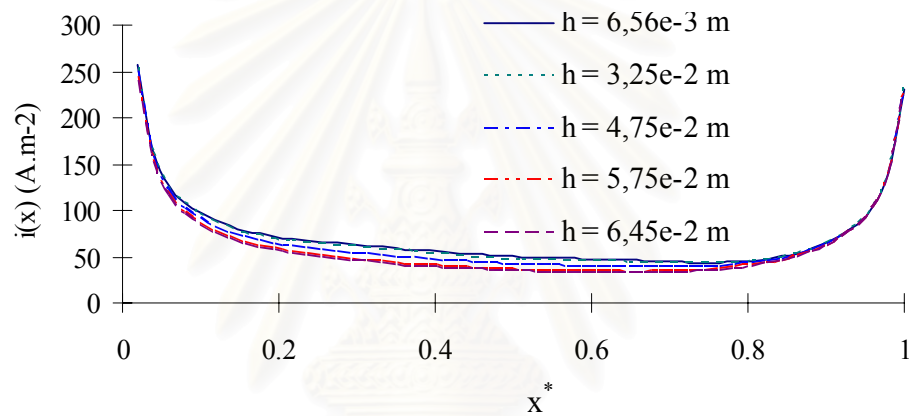


Figure 2.6 Dependence of the dimensionless current density distribution versus dimensionless distance for various average current densities, and comparison with simulated results corresponding to a primary current distribution

The border effects are attributed to the modified configuration of classical Mohler cell by removing its two opposite panels, the front and the end, of rectangular reactor. This facilitates the electrolyte flow conveniently. The current can therefore not only flow through to the slit but also to the slit's border resulting in different current distribution observation at the inlet and outlet of the electrode.

This assumption is validated by Figure 2.7^{22,23} which gives the evolution of the current densities versus position calculated for the modified Mohler cell (a) and for the original Mohler cell (b), at different heights in the reactor. The linear current evolution is observed in the original Mohler cell. The modified Mohler cell does not give a wide current range, in addition, non-linear current distribution and border effects are observed.

Figure 2.8 shows the evolution of the potential distribution for our modified Mohler cell (a) and for the original Mohler cell (b) at 6.45×10^{-2} m. heights in the reactor.



(a)

สถาบันวิทยบริการ
จุฬาลงกรณ์มหาวิทยาลัย

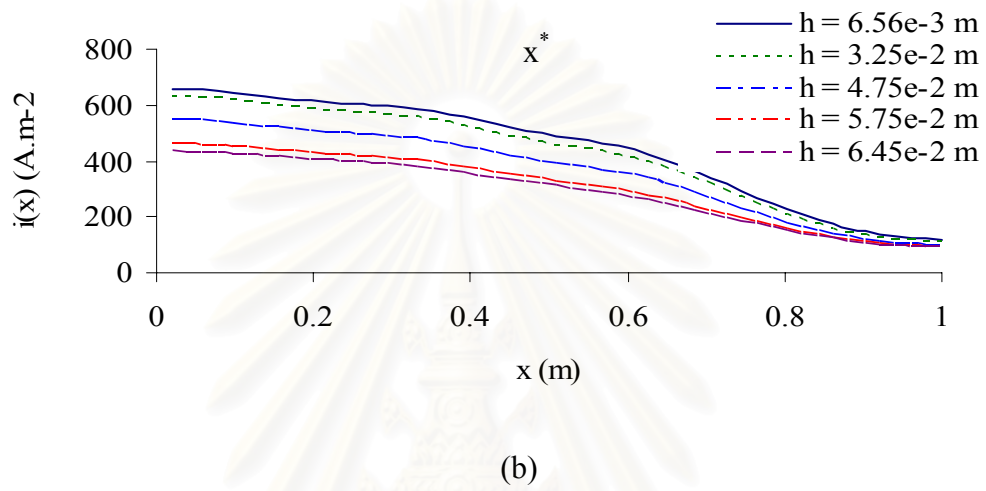


Figure 2.7 Dependence of current density distribution versus distance, (a) the modified Mohler cell and (b) the original Mohler cell at different heights in the reactor^{22, 23}

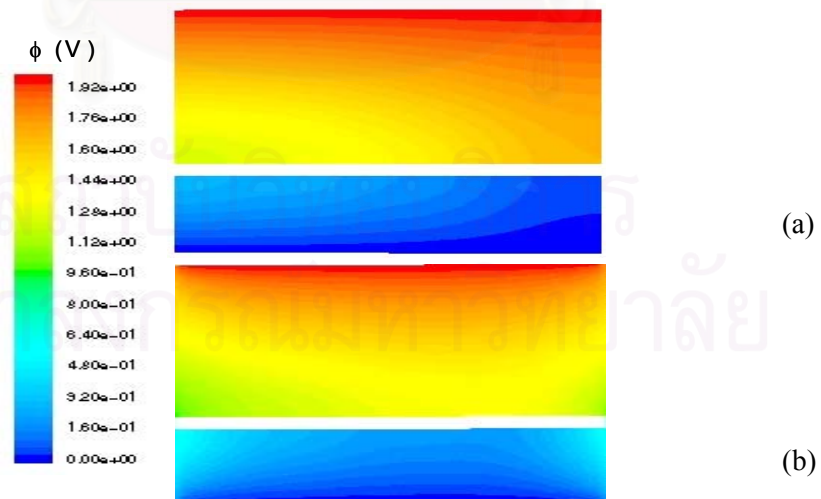


Figure 2.8 Potential distribution in the reactor, (a) our modified Mohler cell and (b) the original Mohler cell at 6.45×10^{-2} m. heights^{22, 23}

This cell is thus not useful as a screening tool, or to control the quality of the bath as the traditional Hull cell or the classical Mohler cell. Further investigation has been performed with other types of plating test to obtain more evenly produced current distributions along the cathode length. The new device is the rotating cylinder Hull cell.

2.3.2 Current Distributions in Rotating Cylinder Hull Cell

2.3.2a Experimental Results

Rotating Cylinder Hull cell (RCH) developed by C. Madore has been chosen. RCH described recently in the literature is employed ^{19, 24, 25}. RCH configuration shown in Figure 2.9 was used for galvanostatic depositions. The working electrode was a nickel cylinder having 15 mm in diameter. The rotating rate was controlled by a rotating electrode (model EDI 101 Radiometer Copenhagen). The electrode length was 60 mm. An insulating cylindrical wall with a diameter of 53 mm was placed around the electrode in order to induce a controlled non-uniform primary current distribution along the electrode length. The counter electrode was a Pt/RuO₂ grid (78 mm in diameter) placed around the outside of the insulating tube. All other sizes are given on the Figure 2.9. The current and potential were controlled by a DEA 332 Digital Electrochemical analyzer (Radiometer), piloted by the software Master 2[®].

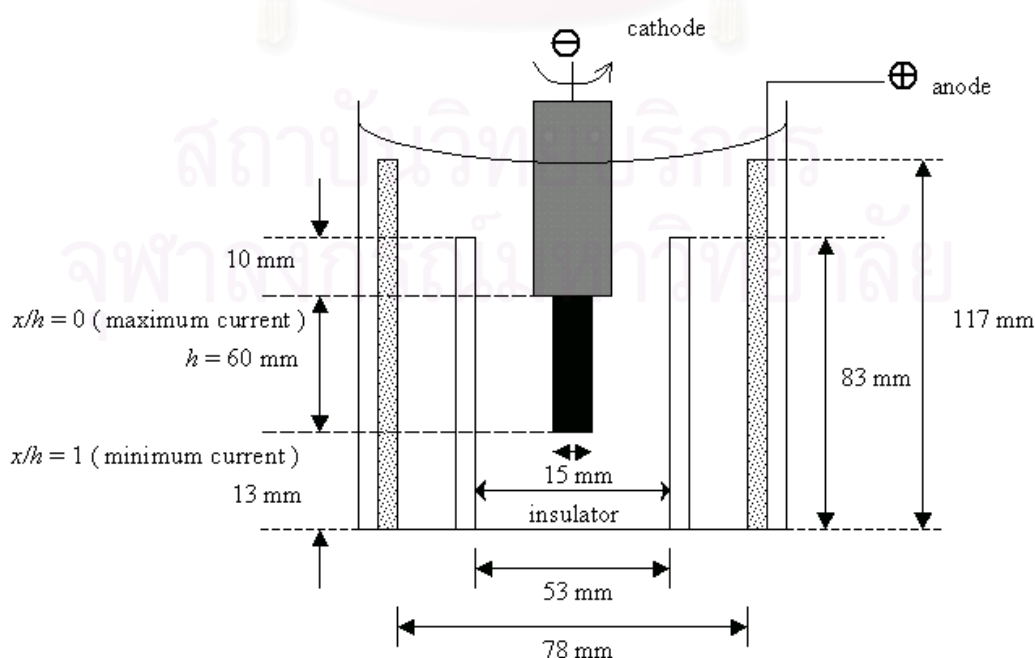


Figure 2.9 Schematic diagram of the conventional RCH cell

Deposition was performed galvanostatically at average current densities ranging from 0.71×10^{-2} mA mm⁻² to 9.2×10^{-2} mA mm⁻² corresponding to Wagner numbers between 0.4 and 0.03 (Table 2.1). The electrolyte was the same solution that those used for modified Mohler cell investigation and the electrolyte resistance was 0.187 Ω m. The cathodic Tafel constant was found to be $\beta_c = 30.8$ mV. The time duration is operated to have an enough amount of copper deposition to analyze with atomic absorption spectroscopy later.

Table 2.1 Operating conditions for RCH tests

i_{ave} (mA mm ⁻²)	Wa	t (s)	Stirring rate (rpm)
9.20×10^{-2}	0.03	726	1250
4.58×10^{-2}	0.06	726	1250
2.76×10^{-2}	0.1	2358	1250
1.41×10^{-2}	0.2	2358	1250
0.71×10^{-2}	0.4	10800	1250

2.3.2b Distribution of Current in RCH

In Figure 2.10, the experimentally determined dimensionless current densities ($i(x^*)/i_{ave}$) are presented as a function of the dimensionless length ($x^* = x/h$) along the cathode. Lower i_{ave} is indicative of a more uniform current distribution. These results agree well with those of the literature, which indicates that a secondary current distribution is more uniform than a primary one.

The variation of current versus the dimensionless distance does not present a border effect. The local current density is found to vary within a range from about 3.4×10^{-2} to 0.4 mA mm⁻² for average deposition current densities ranging from 0.71×10^{-2} to 9.2×10^{-2} mA mm⁻². It is found that the ratio of the maximum (at $x^* = 0.05$) to the minimum current (at $x^* = 0.94$) is 7 that is 3.5 times higher than those obtained in the Mohler cell. The variation thus covers wider current distribution range than the

experiments performed with the modified Mohler cell.

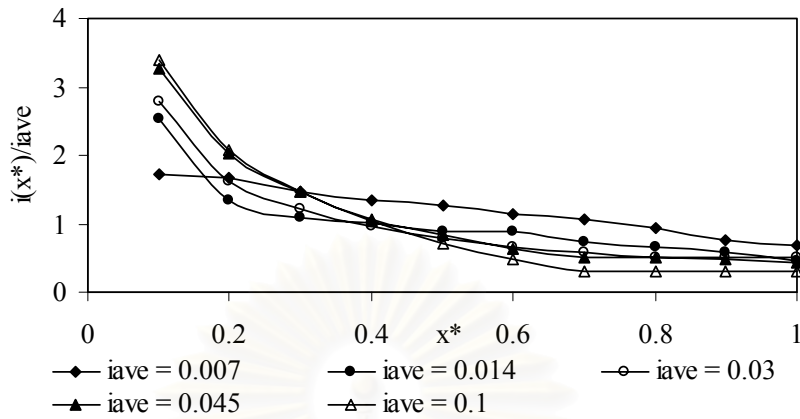


Figure 2.10 Dimensionless current density ($i(x)/i_{ave}$) represented as a function of the dimensionless length (x^*) along the cathode at various average current densities

The theoretical primary current distribution, for the RCH cell can be represented by the following experimental expression²⁴.

$$\frac{i(x^*)}{i_{ave}} = \frac{0.652 - 0.609(x^*)}{\{0.0209 + (x/h)^2\}} + 2.66 \times 10^{-3} \times \exp\{4.53(x^*)\} \quad ; \quad x^* = \frac{x}{h} \quad (2.2)$$

Figure 2.11 represents the experimental dimensionless current densities ($i(x^*)/i_{ave}$) as a function of the dimensionless length ($x^* = x/h$) along the cathode comparing with the empirical relation for primary current distribution given by C. Mafore et. al., secondary and tertiary current distribution coming from simulation results²³. Good agreement is found between the empirical curve and the experimental curves for the average current density (i_{ave}) ranging from 0.1 to 0.045. Therefore it can be concluded that experiments performed with i_{ave} higher than 0.1 are representative of current distributions that are nearly primary. However, i_{ave} being lower than 0.007, is a representative of secondary current distribution. The latter is clearly differentiated from the primary current distribution calculated from the empirical equation 2.2. In this case, the current distribution is much more uniform than those observed at higher i_{ave} .

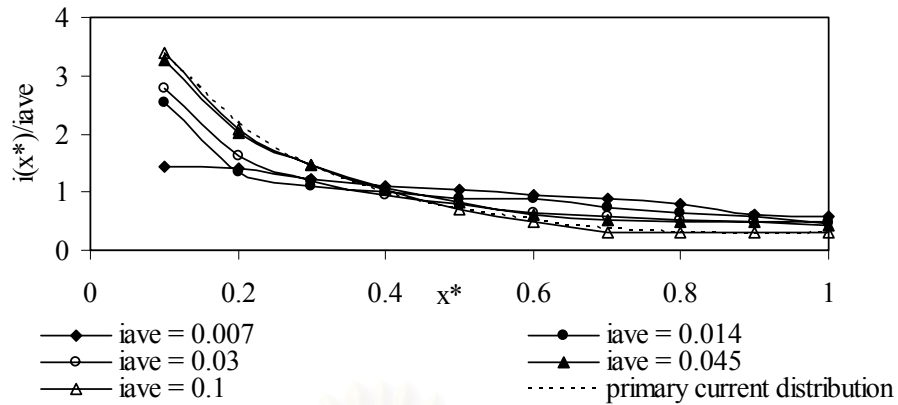


Figure 2.11 Dimensionless current density ($i(x)/i_{ave}$) represented as a function of the dimensionless length (x^*) along the cathode at various average current densities, and comparison with theoretical results corresponding to a primary current distribution (1D), secondary current distribution (2D) and tertiary current distribution (3D)

2.3.2c Copper Plating involving a Mass Transport Limited Step

Experimentation of mass transfer effects is investigated with an average current density of $9.2 \times 10^{-2} \text{ mA mm}^{-2}$, at varied rotation rates ranging from 250 to 2500 rpm. Deposition time is 12 min. and temperature is $22 \text{ }^\circ\text{C}$. In order to facilitate mass transport control of the copper deposition reaction, the electrolyte contains a low copper concentration (1.6 Kg m^{-3}), which is lower than the previous experiment.

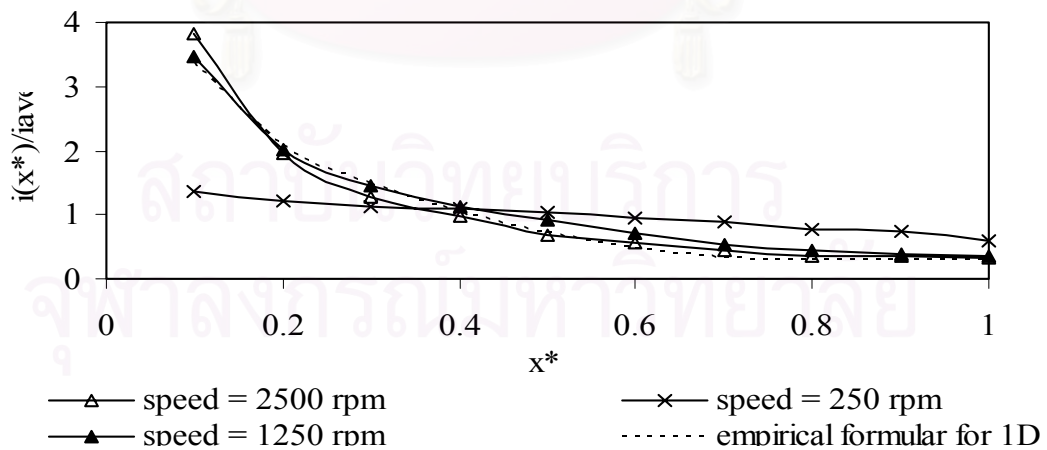


Figure 2.12 Variation of dimensionless current density distribution versus dimensionless distance at various rotating speeds

Figure 2.12 shows the variation of dimensionless current density distribution as a function of dimensionless distance at various rotating speeds. At the speed 1250 and 2500 rpm, the variation of current densities yields current distributions that are nearly primary; i.e. a reasonable agreement between the experimental results and those from the work of C. Madore et. al. On the other hand, at 250 rpm, current distribution is more uniform and corresponds to secondary current distribution (clearly differentiated from the empirical curve and more uniform). Consequently, the effect of mass transport could be observed at the speed of 250 rpm. Moreover, the current efficiency of the rotating speed at 250 rpm is less than 100%. Although the same electrochemical condition is operated, the different results can be obtained in case of inappropriate hydrodynamic conditions chosen. These results show how important hydrodynamic condition should be controlled.

2.4 Conclusion

Two kinds of cells have been tested in order to determine the best device to characterize electroplating baths. The first is a new modified flow-through Mohler cell. This cell was designed, built and tested with copper deposition from acid bath. By positioning an insulating screen between the parallel electrodes, the electric field was distorted to produce a distribution of currents across the cathode of Mohler cell. In this cell, mass transfer is imposed by electrolyte flow parallel to the electrodes, and the experiments performed with this cell can be used to simulate electroplating under industrial hydrodynamic conditions, especially for modern types of industrial cells where mass transfer is imposed by circulation. Except for edge effects at the inlet and outlet of the cathode, the ratio of the maximum to minimum current densities studied was low, ranging from 1 to 2. This fact was confirmed by the results of a model simulating a primary current distribution. However, it could be concluded that this cell is not very useful as a bath control cell where a large range of current densities must occur. The large area cathode allows study of the influence of current on the deposit structure.

The second is a Rotating Cylinder Hull cell (RCH), which has been tested, using the same electrolyte. It has been shown that experimental results agree well with

the empirical formula and theoretical results determined for primary current distribution. In this case, the ratio of the maximum to the minimum current density (a ratio of 7) covers wider range than those observed from the Mohler cell. It could be concluded that this RCH cell constitutes an appropriate reactor to bath control.

Conclusion

The current distribution is widely different in the reactor and significantly relates to the composition. Accordingly, analysis of current distribution in the reactor is an important factor in clarifying the composition, in relation to the current distribution. The simulation study which is complicated and time consuming, was performed by the research team. Basically, the mechanism model and its kinetic parameters obtained from doing elemental experiments are solid foundations in simulation study. The next part of this thesis therefore shows how the kinetic parameters can be determined and how the mechanism model can be developed.



สถาบันวิทยบริการ
จุฬาลงกรณ์มหาวิทยาลัย

PART 3

MICROSCOPIC MODEL

Introduction

Increasing availability of computing power has made it possible to simulate complex electrochemical phenomena. In addition, the design of complex substrate geometry and the electroplating test cell have also been simulated. For example, the simulation results for the current distribution of copper plating along the cathode surface in Mohler cell and RCH cell have well corresponded to the experimental observations in the part 2. For the simulation in the part 2, the simple mechanism and kinetic constant are known with a certain boundary condition.

The mathematical model is not only the extremely useful tool to predict physical event but also to process scale up or scale down, and to identify of mechanisms as a guide to new complicate development of experiments such as alloy plating, and prediction of the alloy composition from a minimum number of experiments.

According to the part 2, the pieces of equipment controlling the bath performance have been determined. In addition, the effects of current distributions have been analyzed. The modeling of the electrochemical cell therefore could be useful. The research team has done the simulation and model of the electrochemical plating test cell. The data such as the boundary conditions, and kinetic parameters are needed for completing the simulation. In the third chapter of this part is mentioned how to determine these data.

The following concentrates on mathematical models predicting the composition of electrodeposited binary alloys. The pure metal deposition is a simple case study, while alloy deposition is more complicated and interesting. Zn-Ni alloy deposition thus is investigated in the following study. The mechanism model of Zn-Ni

alloy is analyzed, and determined the kinetic parameters assuming a homogeneous current distribution and mass transport rate on the working electrode. The established model can be applied further for the computing simulation. The procedure is firstly analyzed the behavior of the Zn-Ni alloy system according to the experimental part. The following procedure is to determine the mechanism of Zn-Ni alloy and the kinetic constant of the model.

The experiments to examine Zn-Ni alloy deposition depending on the operation parameters have been carried out in order to hypothesize effectively the mechanism model. The effect of complex agent to Zn-Ni alloy deposition has also been studied.

Hence, the structure of this part follows by four main chapters. Firstly, the bibliography relating to alloy plating, the literature reports of Zn-Ni alloy deposition experiment, and of Zn-Ni alloy mechanisms have been reviewed. Secondly, the experimental investigation of Zn-Ni alloy deposition has been carried out. The microscopic model of Zn-Ni alloy deposition is followed as the third chapter. The last one is thus the complex agent effect to Zn-Ni alloy deposition.

สถาบันวิทยบริการ
จุฬาลงกรณ์มหาวิทยาลัย

CHAPTER I

Bibliography

1.1 Theoretical Aspect of Alloy Plating

1.1.1 Definition of Alloy

According to the metal handbooks, alloy can be defined as “ A substance that has metallic properties and is composed of two or more chemical elements of which at least one is a metal ”²⁷.

1.1.2 Plating Variable

The functional properties of electrodeposited alloys depend on their chemical composition and on their structure in the micro and nano scales. Many factors could affect the composition and microstructure of electrodeposited alloy as in Figure 1.1.

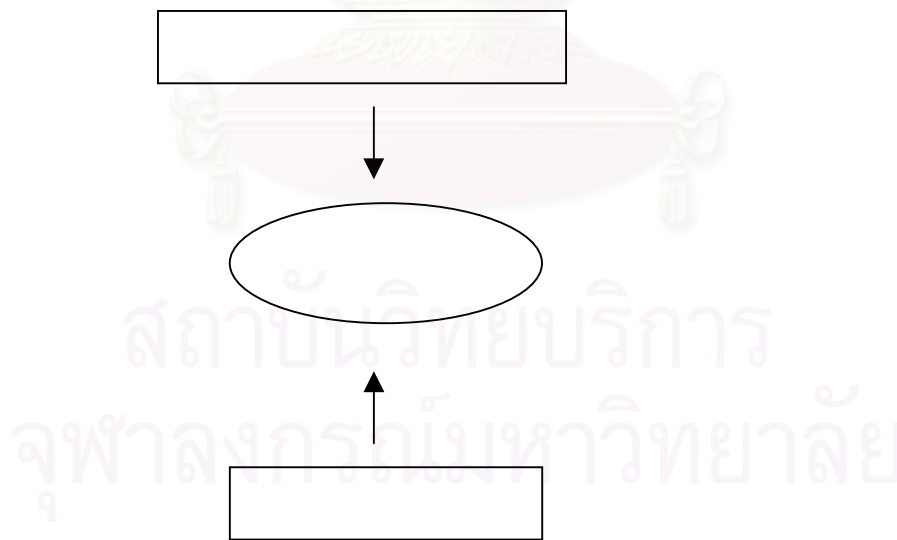


Figure 1.1 Factors influencing the composition and structure of electroplated alloys¹³

1.1.3 Alloy System Classification

The factors that influence the composition of electrodeposited alloys have been comprehensively described by Brenner²⁷, who has classified alloy systems into various types depending on their behavior.

A major distinction exists between “normal” system, in which more noble species deposits preferentially, and “Anormal” system, in which the less noble species is favored. (The term more noble refers to a more positive rest potential.) “Anormal” behavior includes “anomalous” and “induced” codeposition. Anomalous deposition is typically observed during codeposition of the iron group metals: iron, nickel and cobalt, with each other or with zinc. Induced codeposition indicates that a metal which can not be deposited in pure form can be codeposited as an alloy, well known examples being the codeposition of molybdenum or tungsten with iron group metals. Brenner classification is based essentially on thermodynamic and kinetic considerations.

The deposition of zinc–nickel alloys involves the so called anomalous codeposition of zinc^{27,28} since the less noble metal zinc deposits preferentially. So the ratio of this metal is higher in the deposit than in the electrolyte.

A second phenomenon during zinc-nickel deposition is depolarization^{27, 30} which is a positive shift in the equilibrium potential of zinc in the alloy due to the free energy of alloy formation³⁰. The term “underpotential deposition” (UPD) is used below for the deposition of metal species on a foreign substrate in a more positive potential region than the equilibrium potential of the bulk deposit³¹.

1.1.4 Mixed Electrodes

The theory of mixed electrodes was originally developed by Wagner and Traud (1938)¹³ and later by Stern and Geary (1957)¹³ to describe uniform corrosion. It states that the measured current density at a mixed electrode is the sum of the partial

current densities of all anodic and cathodic reactions (anodic partial current densities are taken as positive value and cathodic partial current densities as negative one).

Normally, during alloy deposition, at least two electrochemical reactions proceed simultaneously onto the cathode such as the deposition of the alloy constituents and sometimes the formation of hydrogen. For deposition of a binary alloy of metals A and B yields

$$i = i_A + i_B + i_{H_2} \quad (1.1)$$

where i_A and i_B are the partial current densities of alloy components A and B, respectively, and i_H is the current density for hydrogen formation. The current efficiency for alloy deposition and the composition of the deposited alloy can be expressed in terms of partial current densities. For deposition of a binary alloy AB, this yields for the current efficiency, ϵ

$$\epsilon = \frac{i_A + i_B}{i} \quad (1.2)$$

and for the alloy composition, x_B (expressed as mole % of B)

$$x_B = \frac{i_B/n_B}{i_A/n_A + i_B/n_B} \times 100 \quad (1.3)$$

Here n_A is the electron number involved in the deposition of component A of the alloy, and n_B for deposition of B. It follows from these equations that for given plating conditions the composition of electrodeposited alloys and the current efficiency are uniquely determined by the value of the partial current densities.

1.1.5 Variation of Alloy Compositions with Potential: Kinetic and Thermodynamic Aspects

Figure 1.2 illustrates how the kinetics of partial reactions affects the

composition of electrodeposited alloys. This figure schematically shows the plots of the logarithm of the partial current densities (absolute value) versus potential for different electrode kinetics typically encountered in alloy electrodeposition. One assumes deposition of a binary alloy AB, where A is the thermodynamically more noble element (equilibrium potential: $E_{r,A} > E_{r,B}$).

Figure 1.2a presents a situation where both alloy elements codeposit under activation control, i.e., the charge transfer at the electrode surface is rate limiting and the deposition obeys to Tafel kinetics. In this case, the two Tafel slopes are assumed to be equal. At potentials more negative than $E_{r,B}$, the ratio of the partial current densities for deposition of A and B is changed and $x_B > x_A$.

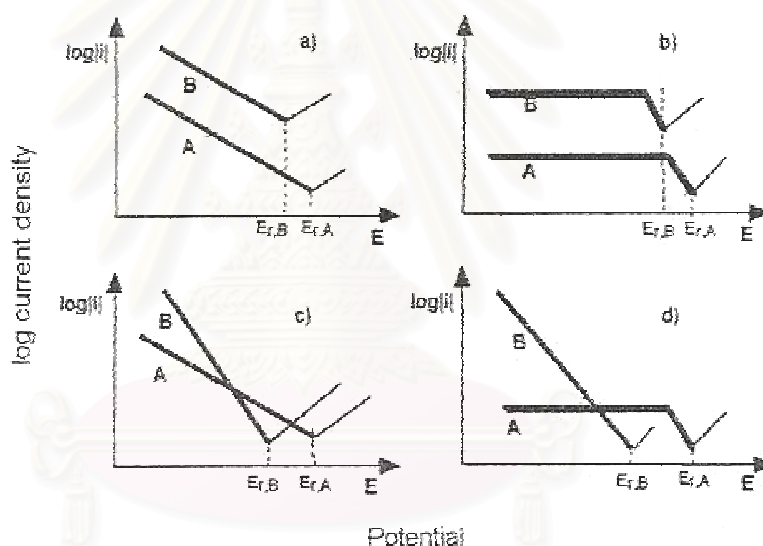


Figure 1.2 Scheme showing the logarithm of the partial current densities for components A and B. (a) both components are under activation control kinetics and exhibit identical Tafel slopes. (b) Both components exhibit a limiting current. (c) Both components deposit under activation control but exhibit different Tafel slopes. (d) Component A exhibits a limiting current, component B deposits under activation control.¹³

In Figure 1.2b, both elements codeposit at the limiting current under diffusion control. In this case, the alloy composition is constant over a wide potential range corresponding to the limiting current plateau.

Figure 1.2c shows a situation where both elements codeposit under activation control, but contrary to Figure 1.2a, here, the Tafel slope of element B is higher than those of element A. The alloy composition therefore varies with potential. At not too negative potentials, the partial current density of A dominates and the deposited alloy contains mostly this element. On the other hand, at very negative potentials the partial current density of B dominates and the alloy deposit therefore contains mostly B. Note that over a wide potential range, the less noble element B deposits at a higher rate than the more noble element A. In this case, the thermodynamic equilibrium potential therefore gives no indication about the alloy composition resulting from codeposition.

Figure 1.2d shows a situation where element A deposits under diffusion control and B under activation control. At potentials more positive than the equilibrium potential of B, only the more noble element A deposits, while at very negative potentials, deposition of B dominates. The described situation is typical for alloy plating electrolytes containing a noble element at low concentration and a less noble element at high concentration.

1.1.6 Experimental Considerations: Determination of Partial Current Densities

To study the codeposition behavior, we need to know how the partial current densities vary with potential. Unfortunately partial current densities cannot be measured directly. Their values must be calculated from the quantity and composition of the deposited alloy. For example, for a binary alloy AB and a thickness of deposit Δd , the partial current density of B is

$$i_B = \frac{n_B F}{M_B \Delta t} m_B \quad (1.4)$$

Here, m_B is the mass of element B deposited in the alloy, M_B is the atomic weight of element B, Δt is the deposition time and n_B is the number of electrons involved in the

reaction of element B. One can therefore estimate either the thickness by assuming the density or the mass of the deposit.

Different chemical and physical methods are available for determining the composition. This one can be obtained by chemical solution analysis after chemical or electrochemical dissolution of the deposit or by physical methods such as X-ray fluorescence (XRF). Electron microprobe analysis, microspot XRF, or scanning Auger electron spectroscopy can also be used to determine the local and surface composition of alloy deposits.

1.2 State of the Art on Experimental Investigation of Zn-Ni Alloy Deposition

The use of zinc and its alloys for improving the corrosion resistance of coated steel sheet has been growing worldwide. In the automotive industry, for example, its use has been growing in a search to increase the corrosion resistance of chassis. In recent years the interest in zinc alloy coatings, such Zn-Ni, Zn-Fe and Zn-Co, has been increasing as a consequence of their better mechanical and anti-corrosion properties than pure zinc coatings, and as a substitute for toxic and high cost cadmium coatings. The Zn-Ni alloys obtained by electrodeposition processes, with the amount of nickel varying between 8% and 14% by weight, give corrosion protection five to six times superior to that obtained with pure zinc deposits^{32, 33}. Electrodepositions of zinc alloy in particular, Zn-Ni, are currently the subject of many studies. They mainly concern sulfate or chloride bath³³⁻³⁶.

1.2.1 Zn-Ni Alloy Deposition from Acid and Alkaline Bath

1.2.1a Operating Conditions

The main Zn-Ni alloy processes are based on two types of electrolyte systems as shown in Table 1.1. One acid type uses zinc and nickel salts (sulfate or chloride) as the main source of metal ions in solution. The acid electrolyte contains buffering agents, such as boric acid or acetic acid, to stabilize the pH during plating. Some

electrolytes also contain a brightener, such as strontium sulfate³⁷, and a leveling agent such as phenolic derivative.

The alkaline electrolyte consists of zinc oxide and nickel salt as the major source of zinc and nickel ions. The electrolyte in this case contains either sodium or potassium hydroxide³⁸.

The Zn-Ni alloy processes operate at various temperatures ranging from 10 to 60 °C. The most popular of the processes operate at room temperature for economic reasons. Most processes operate at a pH between 3 to 5³⁹.

Table 1.1³⁹ Types of electrodeposited Zn-Ni alloy

Electrolyte Constituents	Operating Conditions	Remarks
Concentration, g/L		
Acidic bath 1		
ZnSO ₄ 7H ₂ O	260	Nickel strike bath prior to Alloy plating. pH 1.5 to 3.5, 50 ° C Current Density 30 A/dm ²
NiCl ₂ 6H ₂ O	240	
CH ₃ COOH	3%v/v	
Acidic bath 2		
ZnCl ₂	83.3	25 & 30 ° C, pH 5.5 Current Density 1-4 A/dm ² The optimum corrosion resistance of Zn-Ni alloy. Current efficiency is 95%.
NiCl ₂ 6H ₂ O	1-40	
KCl	210	
H ₃ BO ₃	25	
Acidic bath 3		
ZnCl ₂	50	40 ° C, pH 4.5 Current Density 3 A/dm ² Average coating for rack & barrel plating are 9 and 6.5 μm.
NiCl ₂ 6H ₂ O	15-100	
NaCl	200	
NH ₄ Cl	30	
+ additive, stress reliever and wetting agent		

Electrolyte	Operating Conditions		Remarks
Constituents			
Concentration, g/L			
Alkaline bath			
Zinc oxide	6-12	21-32 ° C	Zn-Ni alkaline plating bath. Application are rack & barrel plating.
NaOH	100-120	pH above 12	
NiCl ₂ ·6H ₂ O	0.7-1.5	Current Density 1-4.5 A/dm ²	Plating efficiency ranges from 60-80%
Zn:Ni	6-7:1		

1.2.1b The Uniform of Thickness Distribution

The problem of the acid bath system comparing with the alkaline bath is its corrosive nature, leaving unplated or recessed areas that may not have been thoroughly rinsed. These areas will be subject to oxidation and rusting after plating. The alkaline bath is free from such problems. In addition, the deposit from the acid solution tends to have poor thickness distribution and significant alloy variation from high to low current density areas. The alkaline bath is more uniform in terms of both thickness of deposit and alloy composition. Despite some advantages of alkaline processes versus an acid bath, the deposited coatings contain less nickel.

1.2.1c Percent of Nickel Deposit relating with Corrosion Protection

Acid Zn-Ni deposits typically range from 7-13 % nickel and the alkaline deposits typically range from 3-7 %. The best corrosion protection is the percent of nickel in the deposit between 12 and 15% independently on the electroplating process. Whereas most commercial processes produced coatings having 10 to 15 percent nickel. In part, because of this, the corrosion protection in acid bath is also considerably higher. For this reason, acid electrolytes are preferred to enhance the corrosion resistance of substrate; alkaline electrolytes are used as a supplement to the successful acid processes⁴⁰. In recent years, the ammonium chloride bath developed

by Muller et. al. can give higher nickel content than do acid bath⁴¹⁻⁴³. Consequently, alkaline bath is now more useful than acidic bath.

1.2.1d Effect of Current Density

The current density as well as the type of zinc-nickel plating bath has a major role in the content of nickel in the deposit depending on the type of bath used. As shown in Figure 1.3, Acid baths produce higher nickel content at low current density before stabilizing at the higher range (3 A/dm²). Alkaline baths maintain a fairly even level from low to high current densities.

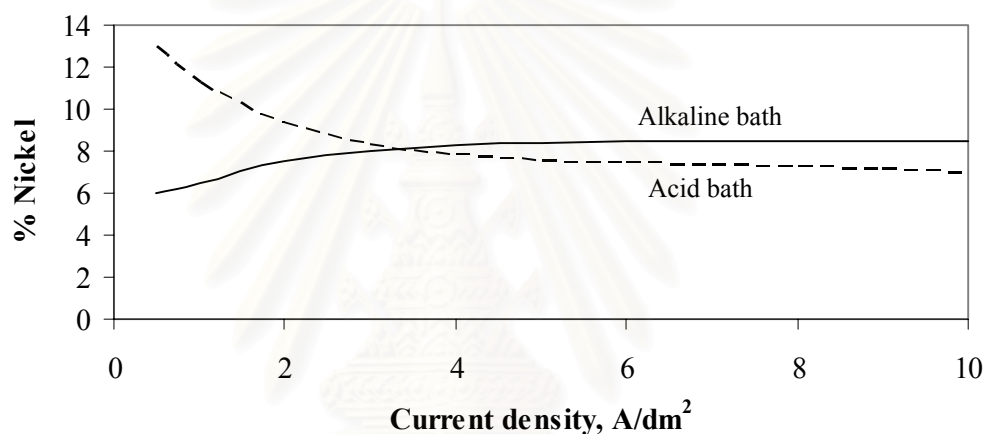


Figure 1.3 Effect of current density on deposit composition for alkaline (solid line) and acidic (dashed line) Zn-Ni alloy baths³⁸.

The operating conditions for ammonium chloride acid bath 3 and alkaline bath are shown in Table 1.1.

1.2.2 Normal and Anomalous Codeposition of Zn-Ni Alloys Deposition

The electrodeposition of Zn-Ni alloys is generally a codeposition of anomalous type, with respect to Brenner's definition, since the less noble metal zinc deposits preferentially and its percentage in the deposit is higher than that in the electrolyte. However, normal Zn-Ni codeposition is possible in particular experimental conditions,^{28, 44, 45}. The codeposition of Zn-Ni alloys from different electrolytic baths has been studied by means of potentiostatic and galvanostatic

electrodepositions with different operating variables. Both normal and anomalous codepositions of Zn-Ni alloy occur according to the following parameters.

Two kinds of approaches have been reported – galvanostatic and potentiostatic modes. The galvanostatic mode is applied for the industrial process and direct application. On the other hand, the potentiostatic bath is used for the research application that is linked directly to the potential governing the equation.

1.2.2a Galvanostatic Electrodeposition

Zinc-nickel alloys were obtained at 40 °C, under galvanostatic conditions, using baths of the following compositions: 28.7 to 67.2 g dm⁻³ NiCl₂ · 6H₂O (0.12 to 0.28 M Ni²⁺), 20.7 to 8.8 g dm⁻³ ZnO (0.25 to 0.11 M Zn²⁺), 125 to 250 g dm⁻³ NH₄Cl, 20 g dm⁻³ H₃BO₃, 0.5 g dm⁻³ dodecyldiethoxy sodium sulphate, 1 g dm⁻³ gelatine; pH 5.8⁴⁵.

Effect of Operating Variables on the Ni Percentage in the Coating

The effect of the nickel ion percentage in the bath and temperature on the composition of the deposits was studied. Figure 1.4 represents the effect of current density on the percentage of nickel in zinc-nickel alloys electrodeposited from different nickel percentage. Figure 1.5 shows the effect of current density on the percentage of nickel in zinc-nickel alloys electrodeposited at the different temperatures.

It is observed that the percentage of nickel in the alloys was approximately constant over a wide current density range and increased strongly at the lowest current density values. This result is similar to that observed by Majid R. Kalantary³⁹ and N. Zaki³⁸ shown in Figure 1.3.

Temperature and percentages of nickel ions in the bath strongly affected the composition of the deposits as shown in Figure 1.4 and 1.5. When increasing temperature and the nickel ion percentage in the bath, the nickel percentage in alloy increased.

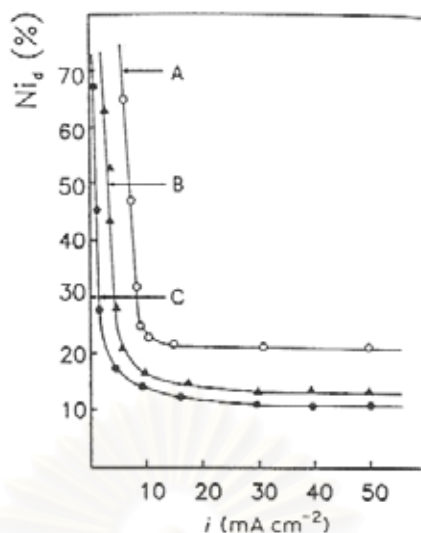


Figure 1.4 Effect of current density on the percentage of nickel in Zn-Ni alloys electrodeposited from baths containing the following percentages of nickel:

(○) 70%, (▲) 50%, (●) 30%. A, B and C points indicate the point where the transition from normal to anomalous codeposition occurs.

$T = 40\text{ }^{\circ}\text{C}$, $\text{NH}_4\text{Cl} = 250\text{ g dm}^{-3}$, $\text{pH } 5$.⁴⁵

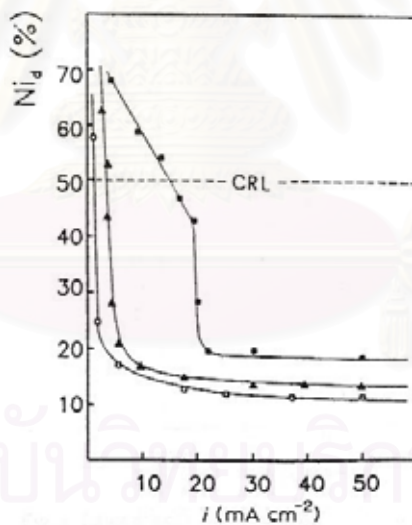


Figure 1.5 Effect of current density on the percentage of nickel in Zn-Ni alloys electrodeposited at the following temperature: (■) $54\text{ }^{\circ}\text{C}$, (▲) $40\text{ }^{\circ}\text{C}$, (□) $30\text{ }^{\circ}\text{C}$.

CRL : Composition Reference Line. $\text{Ni}_b = 50\%$, $\text{pH } 5.8$.⁴⁵

With the operating conditions used, the transition from anomalous to normal codeposition occurs at the points indicated by the letters A, B and C in Figure 1.4 and the intersecting points of the composition reference line (CRL) with the curve obtained at different temperature in Figure 1.5. CRL represents the percentage of

nickel in the electrodeposited zinc-nickel alloys with respect to the percentage of nickel in the plating bath at various current densities.

The effect of current density on alloy composition, on current efficiencies of the alloy deposition and of the hydrogen reduction, together with the polarization curve is shown in Figure 1.6. In correspondence with the transition current density, there is a sharp decrease in the potential and current efficiency in the alloy deposition, and an increase in the current efficiency of hydrogen reduction. This pattern is confirmed by all the measurement carried out by the recent work of Zn-Ni alloy deposition in chloride bath by G. Barcelò and all⁴¹.

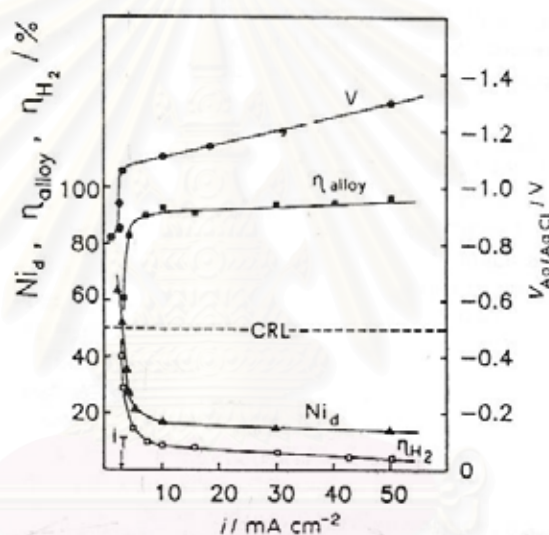


Figure 1.6 Polarization curve during alloy deposition (V/Ag/AgCl) and effect of current density on nickel content of deposits (Ni_d), on current efficiency for alloy deposition (η_{alloy}), and on current efficiency for hydrogen reduction (η_{H_2}), $Ni_b = 50\%$, $NH_4Cl = 250 \text{ g dm}^{-3}$, pH 5.8, $T = 40^\circ \text{ C}$.⁴⁵

The alloy composition depends mainly on the temperature, current density and nickel percentage in the bath. It is observed that at high current density, the alloy composition is uniform and does not depend on the current density as seen in Figure 1.6.

Transition from anomalous to normal codeposition occurs, at low current density. When current densities decrease, the temperature increases and the nickel percentage of the deposit becomes higher than that present in the bath. The current

efficiency of the alloy decreases and the cathodic potential shifts towards more positive values.

1.2.2b Potentiostatic Electrodeposition

For this experiment, Zn-Ni alloys were obtained at various temperature (25, 40 and 44 °C), under potentiostatic conditions using baths of the following compositions: ZnCl_2 7.8 -64.4 g dm^{-3} (0.06-0.47 M); $\text{NiCl}_2 \cdot 6\text{H}_2\text{O}$ 136.2-26.5 g dm^{-3} (0.57-0.11 M); H_3BO_3 26 g dm^{-3} ; KCl 220 g dm^{-3} ; pH 4.8. Zinc and nickel percentages in the bath were changed, while the total metal concentration was kept constant (M_{tot} 37.4 g dm^{-3}). Pure nickel or zinc deposition was also carried out from baths containing 37.4 g dm^{-3} in Ni or Zn⁴⁶.

Effect of Operating Variables on the Ni Percentage in the Coating

Figure 1.7 shows the polarization curves for potentiostatic electrodeposition carried out at 55 °C, using baths containing different nickel percentages and baths with only nickel or zinc ions. Zinc deposition from baths containing only zinc ions starts at about -1000 mV. At higher potentials, cathode surface analysis did not reveal the presence of zinc, indicating that the current is due to hydrogen discharge. Alloy deposition is strongly inhibited of pure nickel, but is enhanced compared to pure zinc deposition at potentials above -1000 mV.

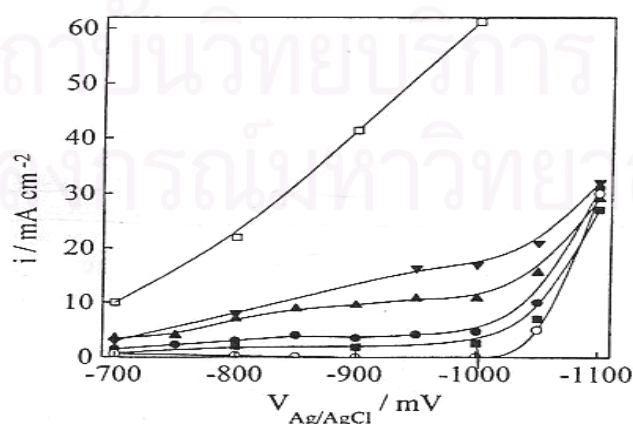


Figure 1.7 Polarization curves for potentiostatic depositions carried out from baths containing the following percentages of nickel (Ni_b): (□) 100%, (▼) 85%, (▲) 60%, (●) 30%, (■) 17.5%, (○) 0%. $T = 55^\circ\text{C}$.⁴⁶

Figure 1.8 presents the nickel and zinc partial current density curves obtained from the bath containing 30% nickel and the curves of pure nickel and zinc deposition from baths having the same concentrations. Zinc and nickel contents were determined by plasma spectrometer after stripping of the alloy by 1:3 HCl solution. These results show that zinc can be codeposited with nickel at potentials where it does not deposit in pure form. These results can be explained by the formation at low cathodic polarization, of a mixed intermediate which catalyses the deposition of nickel rich phases, as proposed by Fabri Miranda and all⁴⁷. And the other one by the induced codeposition, where a given element can be codeposited to form an alloy, but can not be deposited in pure form, interactions between the components in the deposit may shift the deposition potential of the less noble metal⁴⁸.

Figure 1.9 represents the percentage of nickel deposited in the alloys versus potentials at different nickel solution concentrations. Increasing the nickel bath concentration, the changes in composition of the deposits become gradually less dependent on the applied potential. The letters (a), (b) and (c) indicate alloys with the same percentage of nickel in the bath, that is the points where the transition from normal to anomalous occurs.

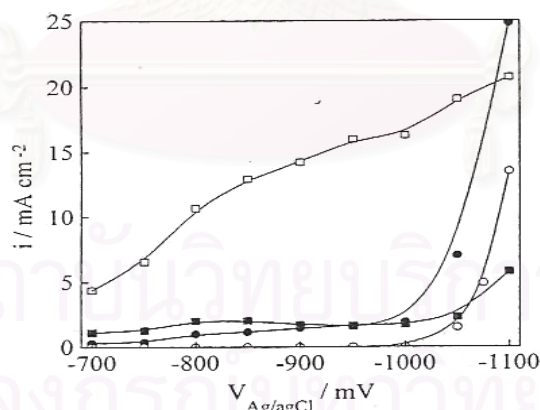


Figure 1.8 Partial current densities for nickel and zinc as a function of applied potential during Zn-Ni alloy deposition (bath containing 30% Ni) and pure metal deposition from baths containing the same zinc or nickel concentrations, $[\text{Ni}^{2+}] 0.19 \text{ M}$, $[\text{Zn}^{2+}] 0.40 \text{ M}$,

$T = 55^\circ \text{C}$; (\square) i_{Ni} , pure nickel deposition; (\blacksquare) i_{Ni} , alloy deposition;

(\circ) i_{Zn} , pure zinc deposition; (\bullet) i_{Zn} , alloy deposition.⁴⁶

On increasing the nickel percentage in the bath, the transition occurs at more positive potentials, the codeposition is anomalous at all potentials for the baths containing 85 and 90 % Ni. These results indicate that high nickel bath concentrations promote anomalous codeposition. The percentage of nickel deposition decreases according to the decrease of nickel and the constant of zinc.

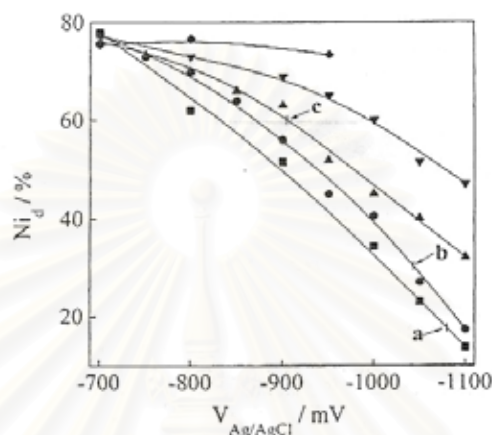


Figure 1.9 Effect of potential on the percentage of nickel (Ni_d) in zinc nickel alloys electrodeposited from bath containing the following percentages of nickel (Ni_b):

(\blacklozenge) 90%, (\blacktriangledown) 85%, (\blacktriangle) 60%, (\bullet) 30%, (\blacksquare) 17.5%, $T = 55^\circ\text{C}$.⁴⁶

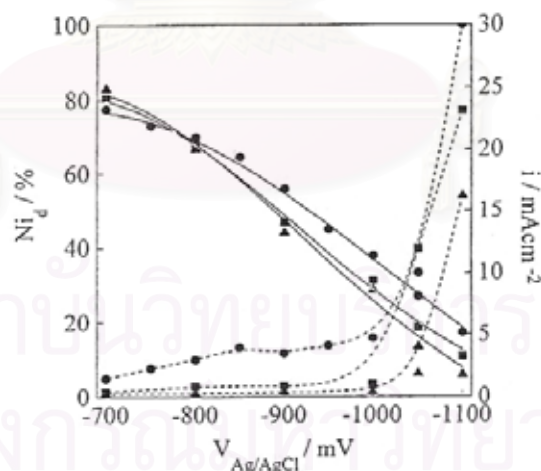


Figure 1.10 Polarization curves (-----) and nickel percentage (——) in the deposits obtained at various temperatures, T : (\bullet) 55, (\blacksquare) 40 and (\blacktriangle) 25 °C, Ni_b 30%²²

Figure 1.10 shows the effect of temperature on the polarization curves and nickel percentages in the deposits. The increase in temperature from 25 to 55 °C does not significantly change the composition of the deposits, which depends mainly on the potential, but leads to an increase in the deposition current density. As

previously found by R. Fratesi (1992)⁴⁵, the temperature increase favors nickel reduction compared to that of zinc.

Figure 1.11 shows the relation between nickel alloy compositions and nickel solution compositions at different potentials. The composition reference line (CRL) is also given. At a potential of -700 mV the alloy composition is almost constant and does not seem to depend on the bath composition. When the deposition potential decreases, the slope of the curves increases because zinc can be more codeposited with nickel and anomalous deposition is often obtained.

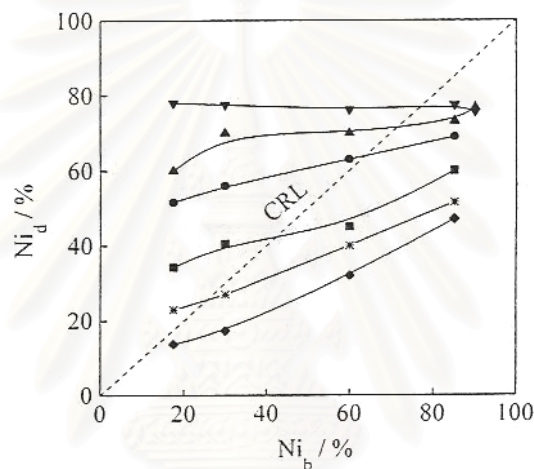


Figure 1.11 Effect of the nickel percentage in the bath (Ni_b) on the nickel percentage of the deposits (Ni_d) obtained at the following potential values: (\blacktriangledown) -700, (\blacktriangle) -800, (\bullet) -900, (\blacksquare) -1000, ($*$) -1050 and (\blacklozenge) -1100 mV, $T = 55^\circ \text{C}$ ⁴⁶

Two different mechanisms depending on the potential have been hypothesized by G. Roventi et al (2000)⁴⁶.

- (i) At low polarization, the production of Zn-Ni alloys is due to the underpotential discharge of Zn, driven by nickel ion reduction. In the potential range from -700 to about -900 mV / SCE, the i_{Zn}/i_{Ni} ratio changes only slightly and does not depend on the bath composition.
- (ii) At potential more negative than -900 mV/SCE, corresponding to the equilibrium potential of the zinc rich phase deposition, zinc and nickel reduction can occur separately, according to their respective exchange current densities.

1.2.3 Dependence of Zn-Ni Alloy Composition with Time

According to the literature review, there are a few authors to pay attention to the time duration of the experiment. In our laboratory, the deposition of different metals on the substrate can give the different properties. The effect of composition change of alloy with time has also been analysed. The following is the literature review of the time affecting on the alloy compositions.

In order to investigate the time duration, experiments were carried out in a three-electrode cell with a capacity of 0.1 dm^3 . ZnCl_2 concentrations $0.63 \text{ mole dm}^{-3}$ and $\text{NiCl}_2 \cdot 6\text{H}_2\text{O}$ of $0.25 \text{ mole dm}^{-3}$ and NH_4Cl of $4.11 \text{ mole dm}^{-3}$ were studied, at a pH of 5.6 by adding ammonia. The alloys were obtained by depositing the metals potentiostatically or galvanostatically onto electrodes of different diameters, glassy carbon (GC, $\phi = 3 \text{ mm}$), nickel ($\phi = 5 \text{ mm}$), and Armco iron ($\phi = 3$ and 7mm) mounted in a Teflon holder. The reference electrode was an $\text{Ag}/\text{AgCl}/\text{KCl}_{(\text{sat})}$ ⁴².

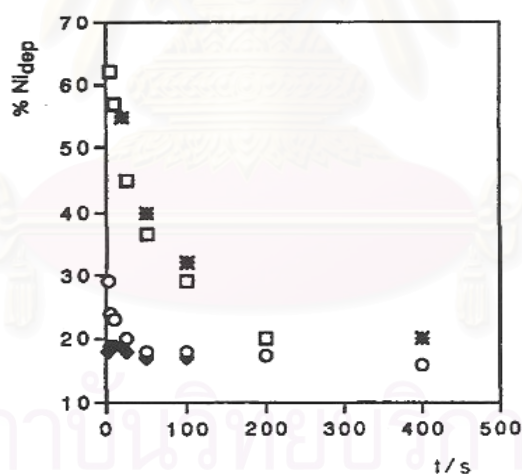


Figure 1.12 Dependence of the Ni content of the alloys on the deposition time for Zn-Ni deposits obtained under different conditions: (□), Fe at 10 mA cm^{-2} , (*) Fe at -1100 mV , (◆), GC at -1195 mV (area $7.1 \times 10^{-2} \text{ cm}^2$), (○) Ni at 13 mA cm^{-2} (area $3.14 \times 10^{-2} \text{ cm}^2$) ⁴¹

Figure 1.12 shows the dependence of the percentage of nickel according to the deposition time, for alloys of similar final composition obtained under potentiostatic or galvanostatic conditions on the three electrodes. The compositions of the coating were analysed by X-ray photoelectron spectroscopy. As shown in the figure, for the iron electrode, the composition of the alloy shows great variation with deposit

thickness. In this case, the nickel content is very high in the first deposit layers and decreases with deposition time until reaching a plateau around 12-15% at 400 s.

These experimental results indicate that, with the electrolyte and with plating conditions used in the present work, the composition of thick deposits corresponded to an anomalous deposition. The first stages of the process included the deposition of an α phase joined with hydrogen codeposition. This fact is confirmed by Yu-Po Lin⁴⁹ explaining nucleation analysis of the initial stage deposition of Zn-Ni alloy. This author also finds that there is a weak interaction between nickel and zinc nuclei at this stage. At longer times, the deposition of the zinc rich η and γ phases is favored, the hydrogen codeposition is also reduced and the current efficiency increases. Although the general behavior is similar to all substrates, the time needed to observe the formation of the γ phase is different. Iron required the longest time and glassy carbon the shortest. Therefore, the nature of the cathode surface determined to some extent the initial stages of the deposition process. If the time duration is long enough, this initial cathode surface effect disappears.

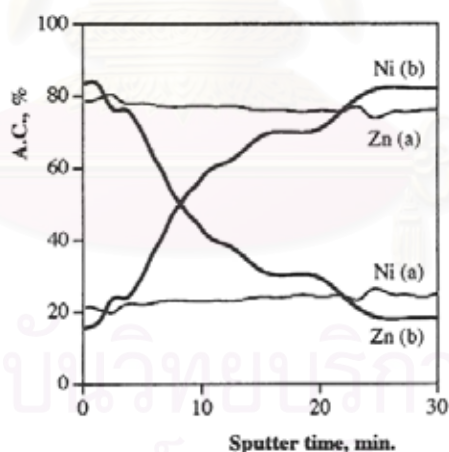


Figure 1.13 XPS depth profiles of Zn-Ni alloys at 20 mA cm^{-2} on commercial iron substrate: (a) $10 \mu\text{m}$ coating, (b) $2 \mu\text{m}$ coating. Rate of sputtering 0.04 min^{-1} ⁴³

Figure 1.13 shows the XPS concentration profiles of two Zn-Ni alloys of different thicknesses obtained on commercial iron⁴³. For a $1.2 \mu\text{m}$ coating (Figure 1.13, a-line), the upper part of the alloy appears a fairly uniform composition. Although the percentages are not quantitative since the alloys have preferential sputtering of zinc (the composition of this alloy determined by AA is 12% Ni).

However, for a 2 μm deposit obtained under the same conditions (Figure 1.13, b-line), XPS results indicate that the nickel content increases near the iron substrate. Thus, it can be concluded that the deposition process of Zn-Ni alloys really begins with the deposition of a very rich nickel layer, and often the Ni percentage then decreases with deposition time.

1.2.4 Conclusion – Experimental Investigation of Zn-Ni Alloy

The objective of the microscopic model part is to establish a model that predicts well the partial current depending on the alloy composition according to the Butler-Volmer equation under potentiostatic mode with the case study of Zn-Ni alloy anomalous deposition. Before establishing the effective model, the experimental investigation has to be carried out in order to understand clearly this deposition behavior.

According to the experimental results of the Zn-Ni alloy deposition from the literature review, nickel, which is the more noble metal, can be deposited firstly on the electrode surface and can then catalyse zinc deposition in the later state. At the potential less negative than the equilibrium potential of zinc, zinc deposition is induced by nickel. When the potential is more negative than the equilibrium potential of zinc, zinc can be deposited with the faster rate after nickel deposition. As well as the study of alloy composition with time, nickel can be deposited firstly on the electrode layer and reduced with time. In addition, the electrode layer has the strong effect on the initial stage of deposition.

It is clearly observed that nickel can catalyse zinc deposition and the substrate thus has an effect on the deposition behavior of Zn-Ni alloy. Zinc inhibits nickel deposition, and the substrate and time duration have effect on this alloy mechanism. According to many experiments of Zn-Ni alloy deposition system, they help towards an innovation of this alloy mechanism. The next topic considers the mathematical model, which is the key role to clearly explain the mechanism of normal or anomalous Zn-Ni deposition, as the literature review.

1.3 Mathematical Modeling investigation of Zn-Ni Alloy Deposition

Electrodeposition of binary alloys of the iron group metals exhibits anomalous codeposition, which the less noble metal electrodeposits preferentially, as stated by Brenner²⁷. Anomalous behavior for binary systems is most often associated with the mutual codeposition of the iron group metal (Fe, Ni or Co) and zinc or cadmium. In the system of Zn-Ni alloy and Fe-Ni alloy are normally the anomalous deposition behavior.

Many authors have studied the mechanism of anomalous codeposition of iron group metals and several hypotheses have been presented, but there is still no theory universally accepted. By this research, two models, the hydroxide suppression mechanism model and the property interface model, are categorized from many models of literature review.

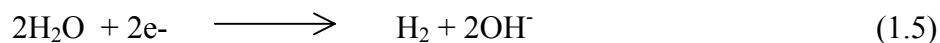
1.3.1 Mechanism Involving Hydroxide Species

1.3.1a Hydroxide Suppression Mechanism [H. Dahms and I. M. Croll, 1965]⁵⁰

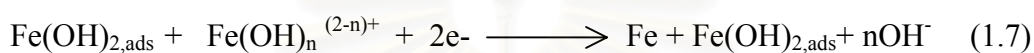
This model assumes the dependence of the anomalous codeposition of iron-nickel alloys on the pH at the cathode surface is investigated. An equation is derived to evaluate the surface pH as a function of bulk pH, rate of hydrogen evolution, buffer concentration, and diffusion mass conditions. The experimental results obtained on rotating disk electrodes show that anomalous codeposition is due to a suppression of nickel discharge and that suppression occurs only when the surface pH is high enough to cause hydroxide formation. They concluded that the increased hydroxide ion concentration near the surface should lead to the formation of ferrous hydroxide, which is adsorbed further on the cathode and suppresses the deposition of nickel and permits a high discharge rate of Fe^{2+} . The mechanism is proposed by which the adsorption of ferrous hydroxide suppresses the deposition of nickel, but permits a high rate of iron discharge.

Mechanism:

On the basis of the discussion given above, the following type of mechanism can be proposed.



At θ :



At $1-\theta$:



where θ is surface coverage of ferrous hydroxide.

Since anomalous codeposition is observed primarily in the electrodeposition of alloys containing one or more ions which are susceptible to form hydroxide (Fe, Co, Ni, Zn), the type of mechanism given above could be of general importance in anomalous plating. It explains the two most characteristic features of anomalous codeposition:

- (i) The sudden change of systems from normal to anomalous codeposition with increasing current density caused by the equally sudden change of the pH at the electrode surface.
- (ii) The strong influence of temperature, which affects the rate of evolution of hydrogen and the rate of diffusion to the electrode.

The Model Disadvantages:

- A large pH rise is not a prerequisite for anomalous codeposition⁵¹⁻⁵⁵ due to the fact that such anomalous codeposition could also be observed for low pH. This agrees with several authors.
- This theory does not explain the enhancement of zinc reduction observed in the normal deposition region, the high current efficiency during anomalous codeposition and the increase in nickel content in the alloy with increasing pH³⁵.

According to above disadvantages, this model is not taken into account for developing Zn-Ni alloy mechanism. Other mechanisms involving hydroxide species are those proposed by Wendy C. Grande and Jan B. Talbot.

1.3.1b The pH Dependent Competitive Adsorption of Monohydroxide Species, MOH^+ [Wendy C. Grande and Jan B. Talbot, 1993]⁵³

According to the explanation of anomalous mechanism was proposed by Dahms and Croll, their experimental results suggested that the onset of anomalous codeposition coincided with a rise in surface pH due to simultaneous hydrogen evolution and alloy deposition at the cathode. They concluded that the increased hydroxide ion concentration near the surface should lead to the formation of ferrous hydroxide which, when adsorbed on the cathode, suppresses the deposition of nickel and permits a high discharge rate of Fe^{2+} . Recently, experimental results⁵⁶⁻⁵⁸ and mathematical modeling^{51, 58} of nickel-iron deposition have shown anomalous behavior even at low hydrogen evolution rates, these studies suggest that a rise in surface pH is not necessarily required for anomalous codeposition to occur.

In this study, a mathematical model is developed to describe the codeposition of nickel and iron in a simple sulfate solution. The approach to analyze anomalous codeposition of Ni-Fe is comprised of two parts:

Equilibrium calculations have determined that the monohydroxide species, FeOH^+ and NiOH^+ , are more abundant than the hydroxide species, $\text{Fe}(\text{OH})_2$ and $\text{Ni}(\text{OH})_2$ by several orders of magnitude for pH ranging from 2 to 9. Therefore, the monohydroxide species may be responsible for anomalous codeposition. $\text{Fe}(\text{OH})_2$ and $\text{Ni}(\text{OH})_2$ are not likely to be key species in the Ni-Fe anomalous codeposition mechanism. A pH rise at the cathode is not necessary for anomalous codeposition of Ni-Fe.

Mechanism:

From this work, the following mechanism for the anomalous codeposition of Ni-Fe for deposition from a simple sulfate solution is proposed



The anomalous codeposition of nickel and iron occurs by charge transfer of their monohydroxide species.

The codeposition is controlled by a pH dependent competitive adsorption of monohydroxide species, MOH^+ , which may react in parallel to the hydrated metal ions of Fe or Ni, M^+ . According to this view, the inhibition of Ni by the codeposition Fe is related to the difference in hydrolysis constants, which favors formation of FeOH^+ at the expense of NiOH^+ .

The Model Disadvantage:

- The model cannot account for the enhancing effect of the less noble species on the more noble one observed recently^{46, 59}.

This model can explain well the disadvantage of hydroxide suppression mechanism and also establish the key species for anomalous deposition mechanism, which can be further used for developing the model of Zn-Ni alloy deposition. However, this model cannot explain the enhancing effect of the less noble species on the more noble one observed recently^{50, 59} and cannot take into account the substrate effect that is observed in Zn-Ni alloy deposition at the short time operation. Consequently, the research team does not take into account this model.

1.3.2 Property Interfaces Models

1.3.2a Underpotential Deposition [S. Swathirajan, 1987]³¹

Swathirajan suggested that the noble component on the alloy substrate might give rise to preferential deposition for underpotential deposition of the less noble metal. This model is taken into account strongly for the underpotential deposition relating to the structure of the deposit. In this case, Zn-Ni anomalous is often the anomalous deposition which is more useful for the industrial application. Consequently, this model is not found much favor since anomalous deposition usually occurs in the overpotential deposition region.

1.3.2b The Competitive Adsorption of Reaction Intermediates [M. Matlosz, 1993]

55

The hypothesis of this model differs from those of Dahms and Croll, and S. Hessami and Tobias. Rather than assuming physical blocking of the electrode surface by adsorbed hydroxides only at high pH, with the potential dependence of the nickel inhibition resulting from hydrogen kinetics, the approach taken here is to consider the adsorption process itself to be potential dependent as the first step in a two-step mechanism for metal ion reduction. Two-step reaction mechanisms involving adsorbed monovalent intermediate ions for the electrodeposition of iron and nickel as single metals can be combined to form a predictive model for the codeposition of iron-nickel alloy. The onset of nickel inhibition at a specific potential is then not related to hydrogen kinetics on the alloy but rather to interactions between the rates of

the electroadsorption step for each of the two metals depositing alone. This competitive adsorption approach provides a direct link between the kinetics for single-metal and alloy deposition. Inhibition of the more noble nickel in the presence of iron is caused by preferential surface coverage of the adsorbed iron intermediate resulting from a difference in Tafel constant for the electroadsorption step between the two elements.

Mechanism:

The basis of the model is the following two-step reaction mechanism for irreversible electrochemical reduction of either of the two metals depositing alone.



The rates for each step are taken to follow simple mass-action laws

$$r_{1,M} = k_{1,M} C_M^{2+} \theta_0 \quad (1.15)$$

$$r_{2,M} = k_{2,M} \theta_M \quad (1.16)$$

where symbol M denotes either Fe or Ni. C_M^{2+} denotes the surface concentration of species M^{2+} , θ_0 the relative fraction of free surface adsorption sites, θ_M the relative surface coverage of species M_{ads}^+ , and $k_{1,M}$ and $k_{2,M}$ potential dependent rate constants defined as follows

$$k_{1,M} = k_{1,M}^0 \exp(b_{1,M}V) \quad (1.17)$$

$$k_{2,M} = k_{2,M}^0 \exp(b_{2,M}V) \quad (1.18)$$

where $b_{1,M}$ and $b_{2,M}$ are Tafel constants, and $k_{1,M}^{\circ}$ and $k_{2,M}^{\circ}$ are pre-exponential factors. At steady state the material balances for the intermediate species yield $d\theta/dt = 0$.

The partial current expresses as a function of the kinetic constants

$$i_{Fe} = -F (r_{1,Fe} + r_{2,Fe}) \quad (1.19)$$

$$i_{Ni} = -F (r_{1,Ni} + r_{2,Ni}) \quad (1.20)$$

The Model Disadvantage:

- The model cannot account for the enhancing effect of the less noble species on the more noble one observed recently^{46, 59}.
- The Tafel slope taking into account the overpotential for the equilibrium potential of the metal species at 0 V/NHE in each applied potential, while the equilibrium potential of each iron group metal is not equal to zero.

According to this model, the inhibition of Ni by Fe can be explained without any further assumption as to the exact nature of the reacting species (hydrolyzed or not). Thus there is no conflict with previous model since the reacting species can be the hydrated metal ions or monohydroxides producing a pH dependent concentration. However, this model do not cover the enhancing effect of the less noble species and not take into account the equilibrium potential of each species. The research team thus has to continue studying the model, which is suitable for all behaviors of anomalous mechanism in Zn-Ni alloy deposition with the influence of substrate nature.

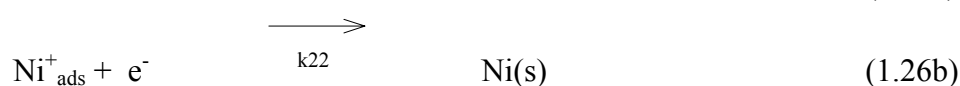
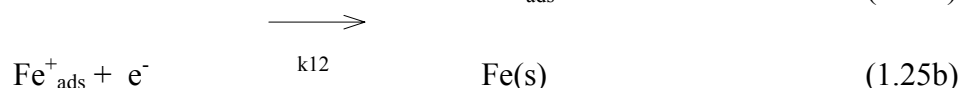
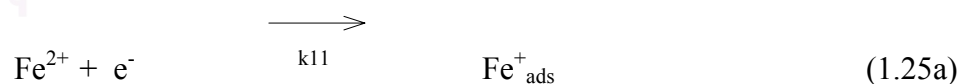
1.3.2c An Adsorbed Mixed Reaction Intermediate containing the Two Codepositing Species in Partly Reduced Form [N. Zech, E.J. Podlaha and D. Landolt, 1999]⁵⁹ and [E. Chasiang and R. Wiart]⁶⁰

The different models proposed further in the literature can explain the observed inhibition of Ni by Fe, but they cannot account for the enhancing effect of the less noble species on the more noble one observed recently by G. Roventi et al⁴⁶ and N. Zech⁵⁹. In this model, anomalous deposition model is presented and critically evaluated which includes both inhibiting effects and enhancing effects. The model assumes that the controlling mechanism for both inhibiting and enhancement involves the formation of an adsorbed mixed reaction intermediate containing the two codepositing species in partly reduced form.

A mathematical model for anomalous codeposition of iron group metals is presented which describes effects of inhibition and enhancement observed experimentally during codeposition of Fe-Ni alloy. The model assumes three parallel reaction paths, each one proceeding in two consecutive steps, and takes into account the effect of mass transport. The model assumes that deposition involved an adsorbed reaction intermediate containing both metal ions in partly reduced form. This reaction intermediate is responsible for both the inhibition of the more noble species and the enhancement of the less noble species.

Mechanism

The present model is based on the assumption that both single metals are reduced in two consecutive steps, as described by Matlosz⁵⁵.



In these equations, Ni^{2+} and Fe^{2+} are dissolved metal ion, hydroxide or not, Ni_{ads}^+ and Fe_{ads}^+ are monovalent adsorbed reaction intermediate which may or may not contain a hydroxyl group, and Ni(s) and Fe(s) are the deposited metals. The adsorbed reaction intermediate of Ni and Fe occupy a fraction θ_1 and θ_2 respectively.

According to the above reaction scheme, simultaneous deposition of two metals can result in inhibition of one or both of codepositing species, but there can be no increase of the reaction rate compared to single metal deposition. To allow an enhancing effect of codepositing species, the following catalytic reaction scheme is proposed which is assumed to take place in addition to the two first reactions.



In the first electron reaction step, an adsorbed mixed reaction intermediate, $[\text{FeNi}^{3+}]_{\text{ads}}$ is formed. The fraction surface coverage of the intermediate is θ_z . In the second electron reaction step, the mixed intermediate is reduced to yield metal Fe(s) and the original ionic species, Ni^{2+} . During codeposition, the metal Fe can be deposited according to two parallel reaction paths, Eqs. 1.25 and 1.27, and its rate of codeposition therefore can be higher than that during single metal deposition. Metal Ni is always deposited according to reaction Eq. 1.26, and can be inhibited but not catalyzed by metal Ni. The extent of the catalyzing and inhibiting effects will depend on the values of the rate constants of the different electrode reactions which determine the surface fractions θ_1 , θ_2 and θ_z of the adsorbed species Ni_{ads}^+ , Fe_{ads}^+ and $[\text{FeNi}^{3+}]_{\text{ads}}$ respectively.

At steady state, the material balances for the intermediate species yield $d\theta/dt = 0$.

The partial current expresses as a function of the kinetic constants

$$i_{\text{Fe}} = -F (r_{11} + r_{12} + r_{31} + r_{32}) \quad (1.28)$$

$$i_{\text{Ni}} = -F (r_{21} + r_{22}) \quad (1.29)$$

The Model Disadvantage

- The Tafel slope taking into account the overpotential for the equilibrium potential of the metal species at 0 V/MSE in each applied potentials, while the equilibrium potential of each metals in iron group metal is not equal to zero.
- The kinetic parameters for the mixed-intermediate reaction pathway can only be obtained from the experimental data of alloy deposition. Therefore, the model does not permit a prediction of anomalous codeposition behavior in case of single metal kinetics.
- The model cannot be used for the quantitative prediction of the effect of electrolyte concentration on the resulting alloy composition. This is due to uncertainties in the prevailing electrode reaction mechanisms and the interaction effects, which are uncalculated in case of single metal kinetics.

According to the present model, the inhibition of the more noble metal is due to a surface blocking effect of adsorbed species similar to that described by Matlosz⁵⁵. The enhancement of the deposition rate of the less noble metal is attributed to the formation of the adsorbed mixed intermediate. The results of this study show that the proposed model describes adequately the main features of the experimentally observed codeposition behavior of iron group metals, including both the inhibition and the enhancement of partial reaction rates due to the codepositing species. However, the theoretical predictions depend critically on the value of the kinetic constants, because the essential features of the model lie in the kinetic expressions and adsorption effects at the surface. The kinetic parameters for the mixed intermediate reaction pathway can only be obtained from alloy data. Therefore, the present model does not permit a prediction of anomalous codeposition behavior only from single metal kinetics. In addition, this model takes into account the equilibrium potential for all deposited species.

As the model shortcoming described above, this model is considered for developing the mechanism of anomalous deposition for Zn-Ni alloy by taking into account the enhancing effect.

1.3.3 Conclusion – Mathematical Model Investigation of Zn-Ni Alloy

Two kinds of model dealing with the mechanism model of Zn-Ni alloy have been investigated – the hydroxide suppression mechanism model and the property interfaces model.

According to the anomalous mechanisms described above, the competitive adsorption effects described by Matlosz is valuable to establish Zn-Ni alloy mechanism. This kind of model is namely the original model, studying of anomalous codeposition developed by combining two-step reaction mechanisms for the electrochemical reduction of the single metals depositing alone. In addition, N. Zech, E. J. Podlaha, and D. Landolt⁵⁹ have adapted this original model to establish the mixed species effect.

There is less observed the enhancing effect in the literature. The Matlosz model is therefore adapted to account for the enhancing effect of the less noble metal proposed by N. Zech. In addition, there is no mechanism model concerning the substrate effect and the composition evolution versus time observed in the recently review of Zn-Ni alloy deposition. The next chapter, all these mechanisms provide an idea to develop the experiments and mechanism model of Zn-Ni alloy system.

1.4 Conclusion

According to a large volume of literature review, it appears that the Zn-Ni alloy deposition is a complex process. Depending upon the operating conditions, deposits can change from normal to anomalous behavior as well as the changing mechanism model to explain in each behavior. It also shows that nickel deposition is inhibited when adding zinc to the solution and that zinc deposition is enhanced when nickel is in the solution. Furthermore, recent works have demonstrated that the layer's

composition changes with time at the beginning of the deposition process. These conclusions will be checked in the next part concerning to our experimental contribution of the study of Zn-Ni deposition. Concerning the mechanism involved in the codeposition process, a lot of mechanisms have been proposed, but no one actually considers these experimental observations. Even though, the observations can explain the inhibition of the more noble metal during the codeposition, less explain the enhancement of the less noble metal. Also, no one can reproduce the evolution of the layer's composition versus time. Thus, two proposal models will be determined in the chapter 3 of this part.

Further efforts in modeling anomalous codeposition should be focused on a critical evaluation of the Matlosz model taking into account the equilibrium potential dependent for each reacting species under steady state and their effluence on substrate nature. In order to establish well the mechanism model specifying the substrate effect, the experimental investigation of Zn-Ni alloy deposition has been carried out in the following chapter.



สถาบันวิทยบริการ
จุฬาลงกรณ์มหาวิทยาลัย

CHAPTER II

The Experimental Investigation of Zn-Ni Alloy Deposition

2.1 Introduction

Alloy coating on metal-based substrates provide desirable surface properties with respect to corrosion protection, wear resistance, and electromagnetic phenomena³⁴. For example, coatings of zinc-nickel on steel better protects corrosion than do pure zinc films³⁹.

According to Brenner's definition,²⁷ the electrodeposition of Zn-Ni alloy system is classified as anomalous codeposition. Zinc, less noble metal, is mostly preferentially deposited. However, normal Zn-Ni codeposition is possible on particular experimental conditions^{28, 45, 46}.

Until now, the codeposition mechanism of zinc with nickel is not clearly identified. At first, Dahms and Croll (1965)⁵⁰ proposed that anomalous codeposition was attributed to a local pH increase, which would induce zinc hydroxide precipitation and would inhibit the nickel discharge. However, several authors found that such large pH rise is not a prerequisite for anomalous⁵¹⁻⁵⁵. Another theory³¹ assumed that anomalous deposition is attributed to the underpotential deposition (UPD) of zinc, but usually anomalous deposition is observed in zinc by overpotential deposition region.

According to the literature reports, other mechanism models of Zn-Ni alloy involved several adsorbed intermediates⁶⁰. In normal deposition region, a mixed intermediate $(\text{NiZn})_{\text{ads}}^+$ acts as a catalyst for Ni^{2+} discharged ions, leading to a nickel rich phase at low cathodic polarization. Anomalous deposition appears when the polarization is increased. Zinc deposition becomes predominant and is incorporated thank to this intermediate into the deposit, leading to Zn rich phase. In anomalous mechanism model, the assumption of mixed intermediate species is applied for all anomalous deposition for iron group metals⁵⁹.

Recently, it has been shown that the electrode layer significantly affects the initial stage of Zn-Ni alloy deposition^{43, 49}. In addition, XPS study has been observed that the deposition process of Zn-Ni alloys really begins with the deposition of rich nickel layers and afterwards the percentage of nickel decreases in accordance with deposition time until reaching a constant value⁴². These facts synchronize with those mentioned by Lin (1993)⁴⁹ dealing with nucleation analysis of the initial stage deposition of Zn-Ni alloy. He found that codeposition of hydrogen and nickel occurs in the initial stage of deposition. Adsorption and evolution of hydrogen are significant, and cause the enhancement of nickel content. Consequently, the alloy composition is influenced not only by the electrodeposition rate (related to the operating conditions) but also, sometimes strongly, by the substrate layer. Most of recent Zn-Ni alloy mechanism has been focused on the mixed intermediate species but there is no studies dealing with the effect of substrate layer. This paper thus considers and clarifies the question of how substrate nature could determine electrodeposited Zn-Ni alloy composition, and hypothesizes a mechanism model of Zn-Ni alloy deposition. The main objective is to investigate in more details of substrate effect between zinc and nickel, and to provide experimental data suitable for theoretical models. Not only studying the substrate effect, but also giving the coherence of all previous considering models are also considered.

2.2 Experiment

In this study, Zn-Ni alloy potentiostatic electrodeposition was carried out from chloride bath for potential ranging from -700 to -1500 mV vs SCE, where both normal and anomalous codeposition occur. For these experiments, an electrochemical quartz microbalance (EQCM)⁶¹ was used. EQCM is a very sensitive probe allowing in situ mass measurements. Experiments of elemental and alloy deposition of Zn-Ni were performed in steady state and potentiostatic modes in order to simplify further modeling works.

A submerged impinging jet cell connecting with EQCM, as shown in Figure 2.1, is used. The nozzle is 8 mm in diameter, glass tube fitted on the cell axis. The

nozzle-electrode distance is 1 cm. The jet is delivered from the reservoir tank by a pump.

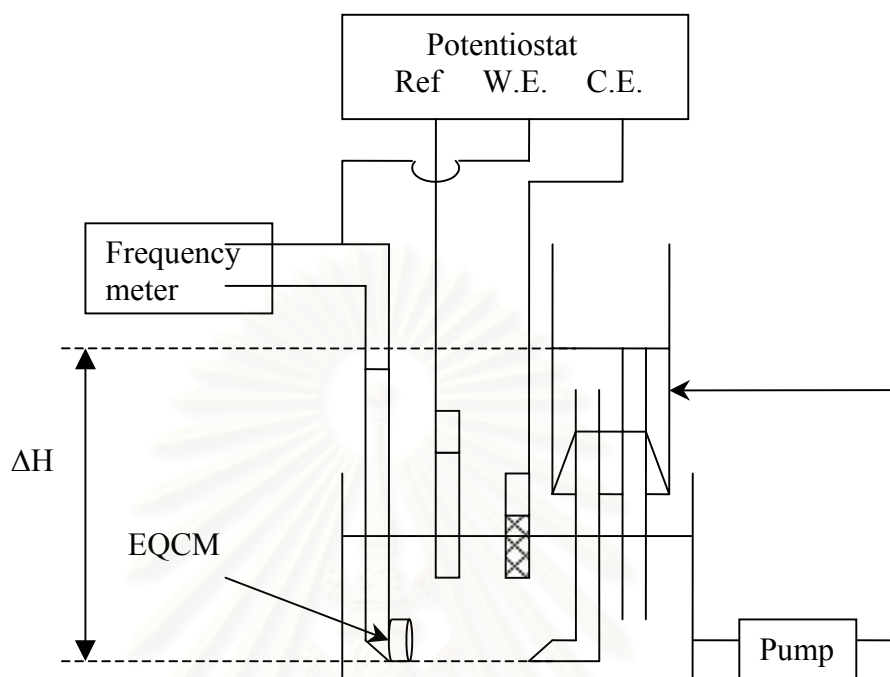


Figure 2.1 General scheme of the EQCM/SIJ setup

EQCM experiments were performed in a typical three-electrode cell. Quartz crystal coated with gold served as the working electrode and was connected with a frequency meter. The active area of the working electrode was $1.37 \times 10^{-4} \text{ m}^2$. The auxiliary electrode is a platinum grid of $25 \times 25 \text{ mm}^2$. All potentials were measured against a saturated calomel electrode. Electrochemical measurements (I,V) were carried out by a DEA 332 Digital Electrochemical analyzer (Radiometer), piloted by the software Master 2[®]. The mass variation was determined by an PM-740 plating monitor (Maxtek) interfaced with a computer.

Zn-Ni alloys were obtained at room temperature (25 °C). The bath composition was the following: ZnCl_2 0.05 mol/L (3.26 g/L); $\text{NiCl}_2 \cdot 6\text{H}_2\text{O}$ 0.05 mol/L (2.93 g/L); pH 4. Pure nickel and zinc depositions were also carried out with the same bath concentration used for the alloy depositions. For the study of the alloy deposition, 0.15 M ZnCl_2 and 0.15 M NiCl_2 were used. All solutions were purged with nitrogen during each experiment. The electrolyte flow rate was $7.26 \times 10^{-6} \text{ m}^3/\text{s}$ for all experiments.

2.2.1 Determination of the Metal Content of the Layer

2.2.1a Alloy Composition

After the deposition, the quartz crystal electrode were thoroughly washed with water and then acetone, hot air dried and weighted. To determine the composition of the electrodeposited alloys, the deposits were dissolved in a diluted nitric solution and nickel and zinc contents were determined by atomic absorption spectroscopy. By means of Faraday's law, the partial current densities of zinc, nickel and hydrogen were calculated.

2.2.1b Single Metal Composition

The current of zinc on zinc substrate, zinc on nickel substrate, nickel on nickel substrate and nickel on zinc substrate can be easily and rapidly obtained with the EQCM device by measuring mass change with times and using the Faraday's law.

Hydrogen evolution during electrodeposition could have a strong effect on the crystal growth mechanism. The total current density measured by the potentiostat is the sum of two partial current densities, $i = i_{\text{Zn or Ni}} + i_{\text{H}_2}$

Hydrogen evolution current can be calculated by this equation conveniently after determining the current of nickel or zinc single metal deposition by EQCM. Normally, the amount of metal is determined by atomic absorption spectroscopy that is delicate and time consuming. With EQCM device, similar results can be easily and rapidly obtained.

2.2.2 Determination of the Minimum Operating Time for Alloy Deposition

According to the XPS study reported by Benballa (2000)⁴³, Zn-Ni alloy composition changes with time, so the ratio of zinc and nickel deposition therefore changes with the operation time. Consequently, in order to simplify the further

modelling of this process, experiments investigating the range of operation time that the alloy deposition reaches the steady-state, have been established depending on the applied current quantity. In order to analyse the effect of operating time over a wide range of deposition, applied potentials at -1.2 and -1.5 V/ SCE are thus considering.

Figure 2.2 shows the current ratio of zinc to nickel deposition in the deposit versus the quantity of current at -1.2 and -1.5 V/ SCE applied potential. This figure shows that the zinc-nickel current ratio for both potentials starts to be constant for a current quantity of 5000 mC. According to this experiment, steady state alloy deposition can be carried out under potentiostatic mode until the applied current quantity reaches 5000 mC for investigated applied potentials.

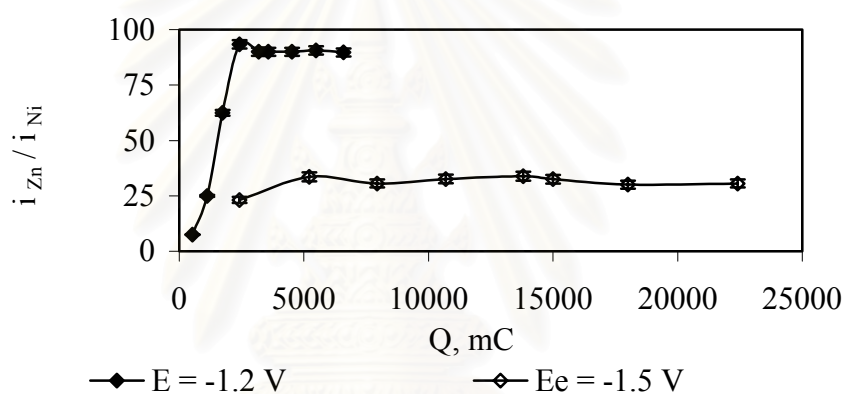


Figure 2.2 The current ratio of zinc to nickel versus current quantity

2.3 Results and Discussions

2.3.1 Changing Deposit Layer Composition in Zn-Ni Alloy with Varying Time

Changing composition of the deposit layer with time was analyzed at -1.2 and -1.5 V/SCE. Figures 2.3 and 2.4 show the partial currents of zinc, nickel and hydrogen evolution at -1.2 and -1.5 V/SCE respectively. i_{zn} is the partial current density of zinc, i_{ni} is the partial current density of nickel, and i_{H_2} is the hydrogen evolution current density. From these figures, they illustrate the two major electrode reactions are zinc deposition and hydrogen evolution. However, the hydrogen

evolution decays quickly from the initial stages of deposition. The nickel content in the alloy decreases sharply and is being steady at 800 and 400 seconds, by applying potential -1.2 and -1.5 V / SCE respectively.

2.3.1a Applied Potential at -1.2 V/SCE

With considering time ranging from 200 to 800 seconds, corresponding to the initial stages of alloy deposition, nickel and hydrogen evolution contents are reduced, while the current efficiency, zinc content and the ratio of Zn/Ni content are increased.

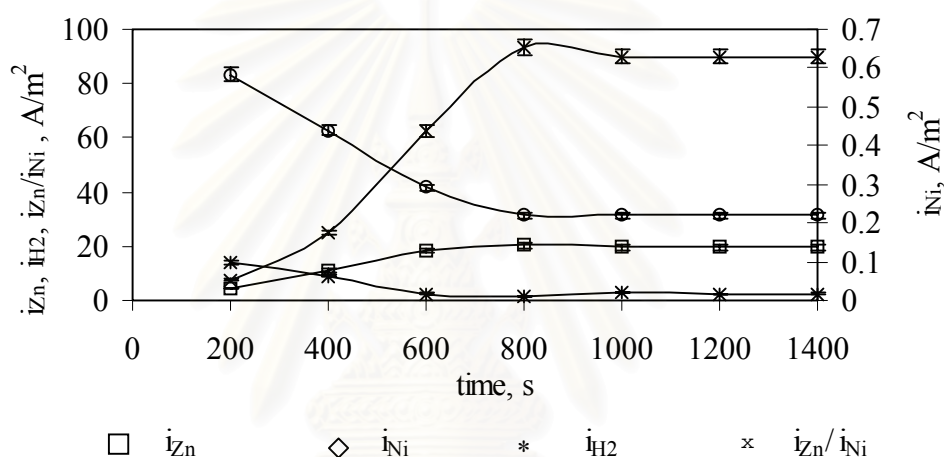


Figure 2.3 Nickel, zinc and hydrogen currents evolution versus the deposition time

$E_{app} = -1.2$ V/ SCE. $ZnCl_2$ 0.05 mol/L, $NiCl_2 \cdot 6H_2O$ 0.05 mol/L and pH of 4

These results are similar to those of Lin and Selman⁴⁹ and Benballa et. al.⁴³ which observed high nickel and hydrogen evolution in the initial stages of alloy deposition. Nickel will firstly deposit on substrate and act as catalyst for hydrogen co-deposition, resulting in the very low cathodic current efficiency and zinc content on the substrate. Afterwards, Zinc, being less catalytic than nickel, will increasingly act as catalyst while nickel deposition and hydrogen evolution is gradually reduced. Increasing both current efficiency and the surface coverage by zinc deposition reduces the nickel content of the alloy. After the time 800 seconds, the content of zinc, nickel, and hydrogen evolution are constant, and leads to a constant of Zn/Ni current ratio and to a steady state deposition.

The change of alloy composition observed with time relates to substrate effect. Nickel deposits firstly on the gold electrode due to the less surface free energy distribution. Zinc deposition on the preceding nickel substrate is the next step. Zinc is more induced by the preceding nickel substrate than the gold electrode according to the less surface free energy distribution taken by nickel⁴⁹.

According to this experiment, normal deposition mechanism was found at initial operating time, as indicated in the literature, less than 50 seconds for ammonium chloride bath⁴³. It can be explained by the substrate effect. In Benbella's works⁴³, the XPS analysis (surface analysis) was applied for a real time indicator. However, the cumulative indicator was used to analyze all the deposit composition content in this experiment. As a result, there is more time taken for reaching a steady state.

2.3.1b Applied Potential at -1.5 V/SCE

The mechanism of Zn-Ni alloy deposition can be explained as the applied potential at -1.2 V/ SCE, changing the nature of electrode surface with time.

At this potential, the reduction rates of zinc and nickel are high compared to -1.2 V/SCE. Zinc is able to deposit on the preceding nickel nuclei more rapidly. The substrate layer grows faster because both intensities are bigger leading to blocking and to decreasing of nickel content. Because of the high reduction of zinc at this potential, the total current reaches the steady state at 400 seconds, while 800 seconds are necessary for applied potential at -1.2 V/SCE.

These results indicate that the change of the electrode nature from gold substrate to zinc-nickel substrate with time, due to the alloy deposition, affects the total current relating to zinc and nickel contents on the electrode surface.

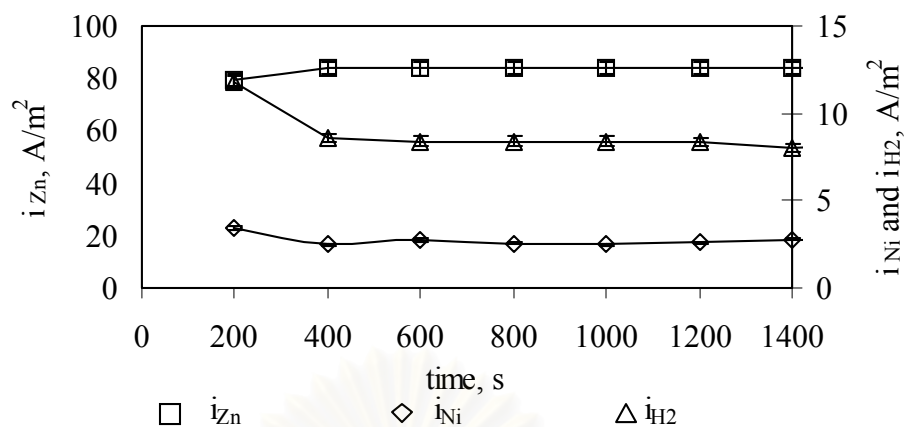


Figure 2.4 Nickel, zinc and hydrogen currents evolution versus the deposition time

$E_{app} = -1.5$ V / SCE. $ZnCl_2$ 0.05 mol/L, $NiCl_2 \cdot 6H_2O$ 0.05 mol/L and pH = 4.

Zn-Ni mechanisms of alloy deposition are therefore influenced by substrate nature. This dependence is attributed to the competing surface by blocking of zinc and nickel, as well as hydrogen adsorption/evolution enhanced by applied potential resulting in inhibiting and catalyzing effect in Zn-Ni alloy deposition as observed in literature report⁵⁹.

Nickel and zinc substrates are thus worthy to study the effect of substrate nature on Zn-Ni alloy deposition. The experiments are carried out by single zinc metal deposition on nickel substrate as well as on zinc substrate, and single nickel metal deposition on zinc substrate and on nickel substrate under potentiostatic operation in the potential range -0.5 to -1.5 V/ SCE by EQCM.

2.3.2 Elemental Deposition

Elemental experiments, single nickel and zinc depositions have been operated on different substrates of nickel and zinc, as shown in Table 2.1. The time duration in each experiment is designated by 10 min, focusing on observation of the substrate effect. The weight of each deposit can be correctly compared with the mass change obtained by EQCM data.

Table 2.1 Elemental deposition analysis focusing on the substrate effect

Elemental deposition	E_{app} , (V/SCE)	E_{eq} , (V/SCE)	Polarization
Ni_Ni [*]	-0.4 to -1.5	-0.536 ⁺	OPD
Zn_Zn ^{**}	-0.7 to -1.5	-1.05 ⁺	OPD
Ni_Zn ^{**}	-1.2 to -1.6 ^{***}	-0.536 ⁺	OPD
Zn_Ni [*]	-0.7 to -1.5	-0.7 ⁺⁺	UPD at -0.7 to -1.05 V OPD at -1.1 to -1.5 V

* Nickel or zinc deposition on nickel substrate. The electrode surface is modified by plating nickel on gold electrode of the quartz disk by chronopotentiometry method at an applied current of -0.02 A for 150 seconds. The plating bath composes of Rhodafac(Gaffre Chimie) 0.5 g/L, NiCl₂ 0.05 mol/L and pH = 4.

** Nickel or zinc deposition on zinc substrate. The surface electrode is modified by plating zinc on the gold electrode of the quartz disk, at an applied current of -0.003 A for 150 seconds (The value of applied current for zinc plating is lower than nickel due to the more rapid deposition of zinc on gold electrode). The plating bath composes of Rhodafac 0.5 g/L, ZnCl₂ 0.05 mol/L and pH = 4.

*** This potential zone is to prevent zinc nuclei oxidation at potentials less negative than zinc equilibrium potential.

⁺ The equilibrium potential is obtained by calculating from the Nernst equation.

⁺⁺ The equilibrium potential is estimated from experiments concerning zinc deposition during underpotential deposition.

The equilibrium potential of Zn_Zn, Ni_Ni and Ni_Zn are determined by the Nernst equation. It is found that the equilibrium potential of Zn_Zn and Ni_Ni is able to correctly compare to those of the experimental data. The equilibrium potential of Zn_Ni is estimated from experiment and shifted to less negative potential than Zn_Zn equilibrium potential. This phenomenon was attributed to the catalytic effect of nickel substrate for zinc deposition.

In each case, hydrogen evolution can be determined by calculating the difference between the total current and the current of nickel or zinc easily obtained by EQCM.

2.3.2a Hydrogen Evolution on Nickel and Zinc Substrates

The current density of hydrogen evolution versus potentials on zinc and nickel substrate is shown in Figure 2.5. The result shows that the rate of hydrogen evolution on nickel substrate is higher than those observed on zinc substrate for each applied potential, since hydrogen adsorption is much weaker on zinc⁴⁹. Consequently, nickel substrate inhibits less hydrogen evolution than zinc substrate.

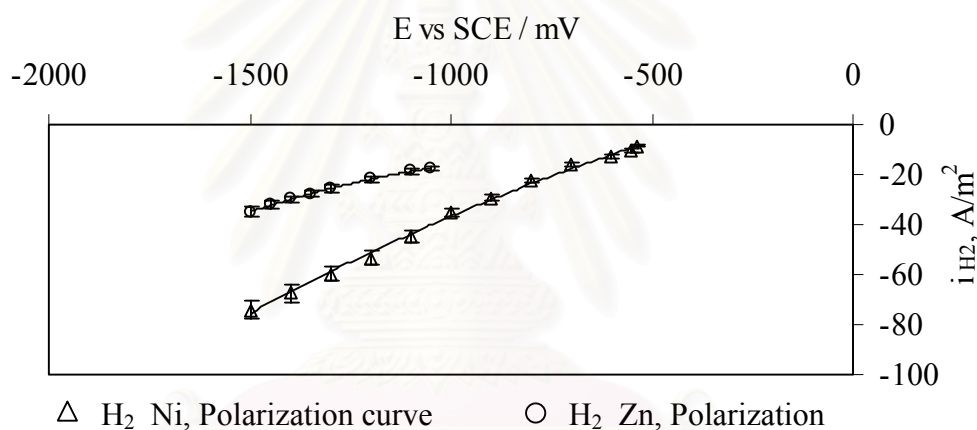


Figure 2.5 Hydrogen evolution on zinc and nickel substrates - Elemental experiment data;
 $C_{Ni}^b = 0.05$ M, $C_{Zn}^b = 0.05$ M.

2.3.2b Nickel Deposition on Nickel and Zinc Substrates

Figure 2.6 shows polarization curves and the current efficiency for potentiostatic depositions of nickel on nickel substrate comparing with those obtained on zinc substrate. It is clearly seen that nickel deposition rate on zinc substrate is higher than on its own substrate for each applied potential. It can be explained that the higher adsorbed hydrogen surface blocking deposition on nickel substrate than on zinc substrate which is clearly seen the more current efficiency observed on zinc substrate.

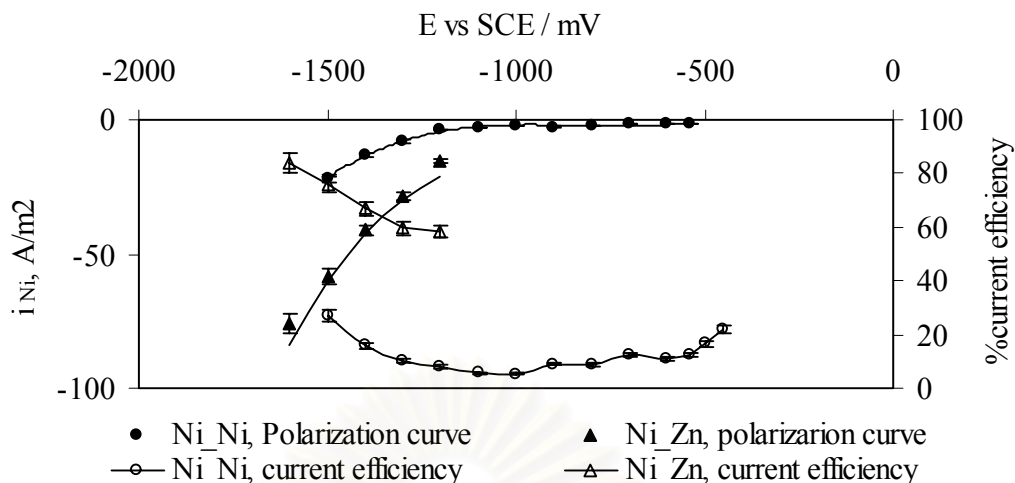


Figure 2.6 Nickel deposition on zinc and nickel substrates - Elemental experiment data;
 $C_{Ni}^b = 0.05 \text{ M}$

2.3.2c Zinc Deposition on Nickel and Zinc Substrates

Figure 2.7 shows polarization curves and the current efficiency for potentiostatic operations of zinc deposition on zinc substrate comparing with those obtained on nickel substrate. At potentials more negative than -1.2 V/SCE , zinc deposits at higher deposition rates on its own substrate than on nickel. At this potential, zinc can deposit less on nickel substrate due to the high rate of hydrogen evolution catalyzed by nickel substrate which is convenient with the more current efficiency observed on zinc substrate. Rate of zinc deposition on zinc substrate is thus higher than on nickel substrate. These results therefore show that for zinc deposition, no catalyzing effect by nickel substrate is observed for this potential range.

For potentials less negative than -1.05 V/SCE , on one hand there is no zinc deposition on zinc substrate and on the other hand, zinc deposition occurs on nickel substrate at potentials that are less negative than equilibrium potential of zinc (underpotential deposition).

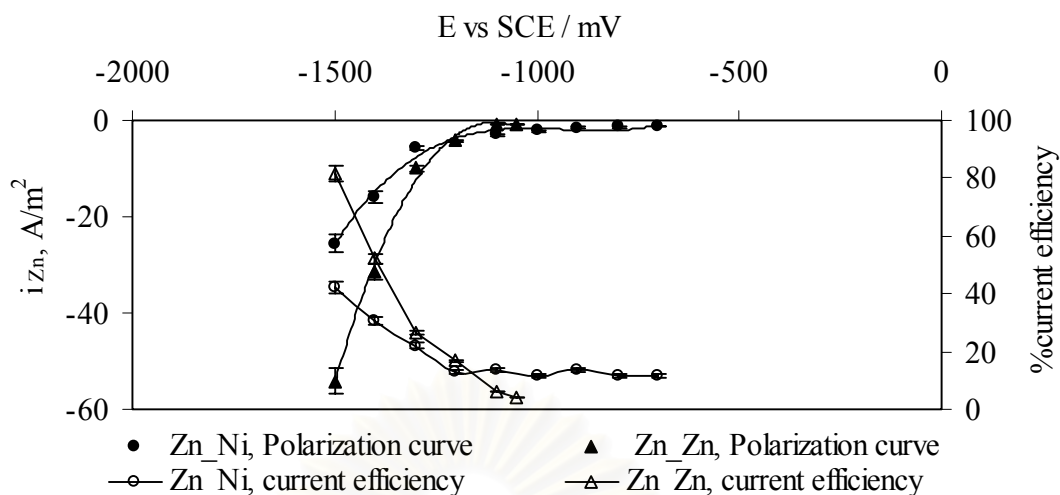


Figure 2.7 Zinc deposition on zinc and nickel substrates - Elemental experiment data;

$$C_{Zn}^b = 0.05 \text{ M.}$$

The equilibrium potential of zinc is thus shifted to less negative potential, when deposit occurs on nickel substrate. The underpotential deposition of the less noble metal, zinc ion, which deposits onto more noble metal, nickel substrate, can therefore explain the normal deposition of Zn-Ni alloy at very low applied potential (less than the equilibrium potential of zinc) and low applied current density (less than $1 \text{ mA}\cdot\text{cm}^{-2}$) reported in the literature^{28, 45}.

These results differ from those obtained by Chassaing and Wiart⁶⁰ who attributed the deposition of nickel rich alloys at low cathodic polarization (normal deposition) to the mixed intermediate ($\text{ZnNi}_{\text{ads}}^+$), which catalyses the reduction of Ni^+ ions.

This experiment can be concluded that single zinc deposition on nickel substrate is catalyzed by nickel for underpotential deposition. This behavior is attributed to a thermodynamic effect because zinc deposition is not normally observed in these potentials range. On the other hand, zinc can deposit faster on zinc substrate. This behavior is a kinetic effect, which is attributed to the lower hydrogen adsorption on zinc substrate than on nickel substrate. This fact is also observed for single nickel deposition that is faster on zinc substrate.

2.3.3 Alloy Deposition

Figure 2.8 represents hydrogen evolution current, the comparison of hydrogen evolution density polarization curve between elemental deposition on zinc and nickel substrates and alloy deposition are established.

At the potential -700 to -1000 mV, the hydrogen current density in alloy deposition is lower comparing to H_2_Ni substrate. In addition, at the potential that more negative than the equilibrium potential of zinc, hydrogen current density continue to decrease. This behavior of hydrogen current density in alloy deposition is also found by Chassaing and Wiart.

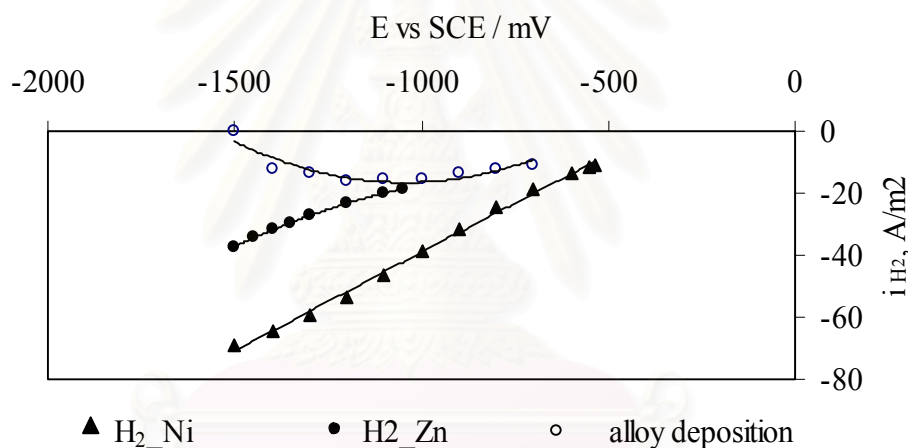


Figure 2.8 Hydrogen evolution current density for alloy and elemental experiments data;

$$C_{Ni}^b = 0.05 \text{ M}, C_{Zn}^b = 0.05 \text{ M}$$

Regarding the differences between elemental and alloy deposition intensities of hydrogen evolution observed, the mechanism is not therefore able to hypothesize by the substrate effect. The solution effect of mixed species, observed by Chassaing and Wiart at the overpotential deposition of zinc, is used to explain this behavior. The mixed species formed at the electrode can inhibit hydrogen evolution in alloy deposition comparing with the single metal deposition in nickel and zinc deposition.

Figure 2.9 shows the comparison of polarization curve of nickel current density between elemental deposition on zinc and nickel substrates and in the case of alloy deposition. The inhibiting effect in nickel alloy deposition is observed. It is found that current density of nickel in alloy deposition is 10 times lower comparing to those obtained for Ni_Ni elemental deposition and 40 times lower comparing to deposition Zn-Ni elemental deposition.

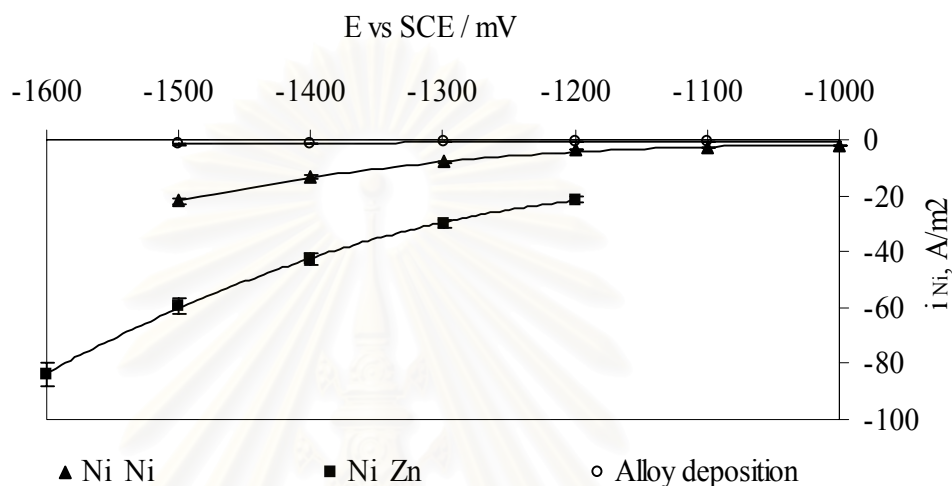


Figure 2.9 Nickel current density for alloy and elemental experiments data; $C_{Ni}^b = 0.05$ M, $C_{Zn}^b = 0.05$ M.

Figure 2.10 illustrates the comparison of zinc current density between elemental deposition on zinc and nickel substrates and alloy deposition. The enhancing effect in zinc alloy deposition is observed. For zinc deposition, it appears that zinc current density in alloy deposition is 3 times higher comparing to Zn_Ni and 1.5 times higher comparing to Zn_Zn elemental deposition.

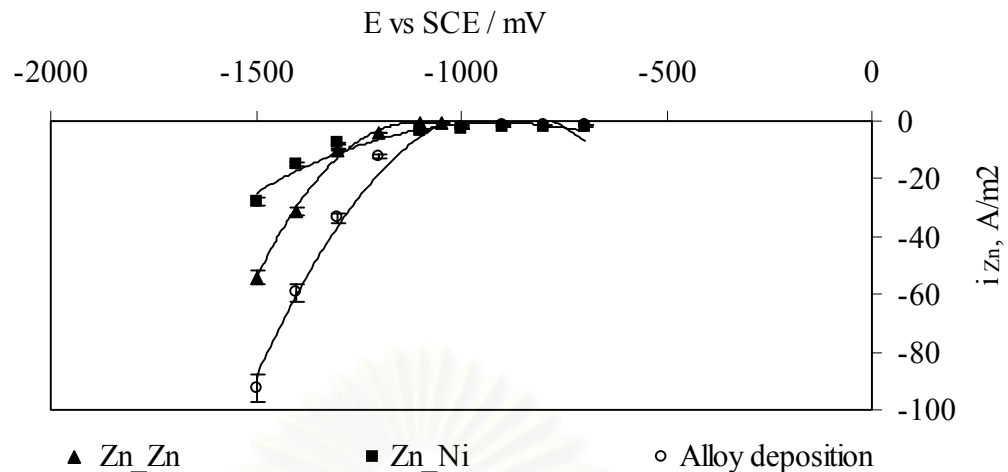


Figure 2.10 Zinc current density for alloy and elemental experiment data; $C_{Ni}^b = 0.05 \text{ M}$,
 $C_{Zn}^b = 0.05 \text{ M}$.

According to Figures 2.9 and 2.10, differences between elemental and alloy deposition intensities are observed. Alloy deposition are unrelated to the substrate effect, the positional graphs of the partial currents of nickel and zinc are not located between nickel and zinc elemental deposition. As this result, it is assumed that there must be a solution effect, with respect to the mixed species mechanism (Chassaing and Wiart).

Figure 2.11 and Figure 2.12 present the partial current density of nickel and zinc respectively observed during alloy deposition when the concentration of zinc and nickel in the bath are increased 3 times.

In Figure 2.11, the partial current density of nickel are considered during an increasing proportion of nickel and zinc concentration in the solution. It is observed that partial current density of nickel increases regarding the increasing of nickel concentration. Conversely, increasing zinc concentration leads to decreasing of nickel partial current density. This behavior is contrary with those observed for nickel elemental deposition on zinc substrate. Consequently, the inhibiting effect in nickel alloy deposition is not attributed to the substrate effect only but the solution effect must also be considered. Increasing zinc concentration leads to increasing zinc ion concentration, which can form the mixed species that catalyze further zinc deposition, inhibit the nickel deposition, and decrease the nickel content in the deposit.

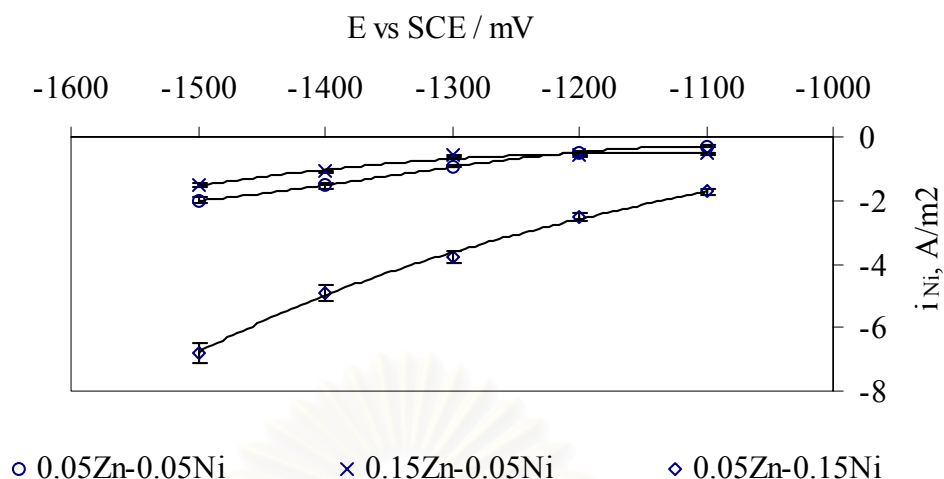


Figure 2.11 The influence of coelement concentration on nickel partial current density during Zn-Ni codeposition

For Figure 2.12, the partial currents of zinc are considered during an increasing proportion of nickel and zinc concentration in the solution. Increasing zinc concentration leads to the increase of the partial current density of zinc. On the other hand, when the nickel concentration is increased, the zinc partial current density is also increased. This behavior is contrary with those found in zinc elemental deposition on nickel substrate. Consequently, the enhancing effect of zinc, when codeposit with nickel, is not attributed to the substrate effect. Likewise, the inhibiting effect of nickel substrate to zinc deposition in the overpotential deposition is not found. Increasing nickel in the solution enhance zinc deposition. This fact is therefore attributed in this case to the solution effect, certainly due to mixed species of nickel and zinc ions. This result is in accord with those observed by Chassaing and Wiart.

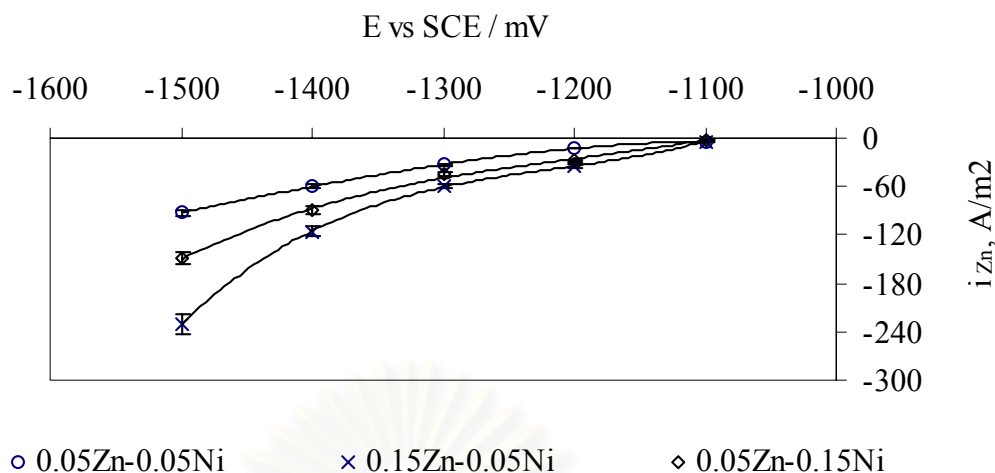


Figure 2.12 The influence of coelement concentration on zinc partial current density during ZnNi codeposition.

2.3.4 Mechanism of Normal and Anomalous Deposition in Zn-Ni Alloy

Regarding the experimental results, at the initial stage of Zn-Ni alloy deposition, zinc reduction following the preceding nickel deposition and hydrogen adsorption on the electrode surface is observed. Moreover, the underpotential deposition of zinc driven by the nickel substrate is observed in elemental deposition. The mechanism of normal and anomalous deposition of Zn-Ni alloy influenced by substrate nature can be then explained.

The normal deposition can be explained by the following mechanism. At the initial stage, a high deposition of nickel happens because nickel more noble properties and then catalyses hydrogen adsorption, leading to high nickel and hydrogen evolution observed in the beginning of Zn-Ni alloy deposit. In the later stage, the deposited nickel at the initial stage induces zinc reduction in an underpotential deposition mode. As a result, rich nickel content and low zinc content always occur in the low potential operation. In addition, Zinc reduction is still not high in this normal deposition.

However, when the applied potential is higher than the equilibrium potential of zinc, high zinc deposition rates occur, resulting in anomalous deposition. This circumstance could happen after hydrogen adsorption and nickel deposition in the

early stage of the deposition process. Nickel substrate does not catalyze zinc deposition at the overpotential of zinc, in the elemental deposition analysis. This means the enhancement of zinc deposition can not be explained by the substrate effect. Anomalous deposition therefore is not the substrate relate. According to the alloy deposition experiments, the anomalous deposition is explained by the solution effect. It's possible that zinc codeposits with nickel to form a mixed species of nickel and zinc ion leading to an enhancement of zinc deposition. The anomalous deposition is thus hypothesized by the mixed species effect in the high polarization.

2.4 Conclusion

Zn-Ni alloy potentiostatic electrodepositions in the range -0.7 to -1.5 V / SCE by EQCM and the study of Zn-Ni alloy composition changing with time have been analyzed. The mechanism of Zn-Ni alloy deposition depending on the applied potential and the scale time considered can be hypothesized.

- (i) Normal deposition mechanism in Zn-Ni alloy for low polarization is due to the underpotential deposition of zinc driven by the preceding nickel nuclei depositing at the initial deposition stage. (substrate effect)
- (ii) The enhancing effect of zinc and the inhibiting effect of nickel are found in alloy deposition. It leads to the anomalous deposition which attributes to the solution effect at the high polarization, due to the mixed species at the steady state.
- (iii) For time less than 800 seconds, the time deposition has an effect on the composition of the deposit. This effect was attributed to a substrate related.

CHAPTER III

Mathematical Modelling of Zn-Ni Alloy Deposition

According to the experimental results in chapter 2, the substrate has an effect on the mechanism of Zn-Ni deposition, especially at the initial stage deposition and the UPD of zinc on nickel substrate. On the other hand, the solution has an effect on the mechanism of Zn-Ni deposition at the overpotential deposition of zinc. The solution effect is due to the mixed species observed by Wiart and Zech in the literature reports. This chapter is composed of models explaining Zn-Ni mechanism in terms of substrate and solution effect.

3.1 Substrate Effect Model

3.1.1 Introduction

In chapter 2, the electrodeposition of Zn-Ni alloy is investigated. It is suggested that initial nuclei of nickel adsorbed on the electrode surface act as a substrate to catalyse zinc deposition, resulting in inhibiting nickel deposition. It is also shown that pure zinc cannot be electrodeposited from aqueous electrolytes at the UPD, but can be codeposited with nickel. These phenomena can be explained that nickel nuclei deposited firstly with hydrogen atom as an adsorbed species to catalyse zinc deposition. At more negative potential than equilibrium potential of zinc, zinc deposition rate is high enough, and inhibits nickel deposition resulting in “Anomalous deposition”. The purpose of this research is to verify the experimental result of Zn-Ni alloy codeposition taking into account the substrate effects, from chapter 1.

3.1.2 Model Assumption

In this chapter, a mathematical model describing the codeposition behaviour of nickel and zinc, in a more quantitative way, is presented. According to the experimental result of chapter 2, the adsorbed nuclei of nickel acting as a substrate to catalyse zinc deposition is of great value to make a model, Zn-Ni alloy mechanism

under the assumption of substrate effect. Although, Zn-Ni composition changes with time, the steady state condition is operated with respect to model simplification. The Matlosz's model was modified by means of focusing on the enhancing effect of zinc and the inhibiting effect of nickel. Zn-Ni alloy deposition is assumed to be substrate effect. Not only nickel affects on zinc deposition, but also zinc affects on nickel deposition.

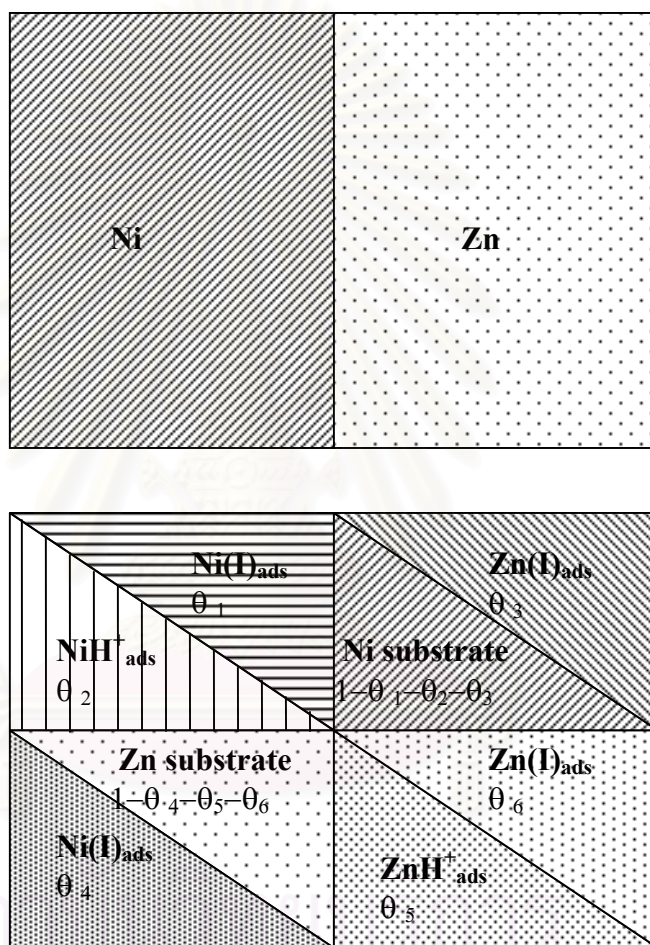


Figure 3.1 Diagram of Zn-Ni alloy codeposition

Figure 3.1 is a diagram representing the effect of different substrate coverage during Zn-Ni alloy codeposition. The electrode surface is firstly divided into two parts. The first one corresponds to θ_{Ni} which is the surface covered by nickel and the second one is the area covered by zinc, θ_{Zn} . Each of these elementary surfaces is further divided into four paths.

In case of nickel alloy deposition, $\theta_{Ni}\theta_1$ corresponds to the surface area of nickel substrate covered by $Ni(I)_{ads}$. $\theta_{Ni}\theta_2$ corresponds to the surface area of nickel substrate covered by NiH^+_{ads} . $\theta_{Ni}\theta_3$ corresponds to the surface area of nickel substrate covered by $Zn(I)_{ads}$. The free surface area $\theta_{Ni}(1-\theta_1-\theta_2-\theta_3)$ corresponds to the surface area of nickel substrate path.

In case of zinc alloy deposition, $\theta_{Zn}\theta_6$ corresponds to the surface area of zinc substrate covered by $Zn(I)_{ads}$. $\theta_{Zn}\theta_5$ corresponds to the surface area of zinc substrate covered by ZnH^+_{ads} . $\theta_{Zn}\theta_4$ corresponds to the surface area of zinc substrate covered by $Ni(I)_{ads}$. The free surface area $\theta_{Zn}(1-\theta_4-\theta_5-\theta_6)$ corresponds to the surface area of zinc substrate path.

3.1.3 Theoretical Model

3.1.3.1 General Mechanism of the Electrode Reaction

A reaction path has been developed by the basis of the substrate effect. The present model is assumed that the deposition of each individual component follows a two-step reaction as described by Matlosz. Nickel ion can deposit on its own substrate and on zinc's substrate according to reaction 1 and 2 respectively. Also, Zinc ion can deposit on zinc's substrate and on nickel's substrate as seen in reaction 4 and 5. In addition, the reactions of the hydrogenated blocking the adsorbent ZnH^+_{ads} and NiH^+_{ads} , are supposed to be strongly bonded to the electrode surface and taken into account as reaction 3 and 6 respectively.

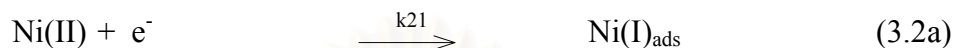
$Ni(II)$ will react to give NiH^+_{ads} and this adsorbed species will then react to deposit Ni. Also, $Zn(II)$ will react to give ZnH^+_{ads} and then this adsorbed species has to react to deposit Zn. Depending upon the substrate, the first step (adsorption) could have a different kinetics.

The following reducible reactions are assumed to take place.

$\text{Ni(I)}_{\text{ads}}$ adsorb on Ni substrate, $\theta_{\text{Ni}}\theta_1$



$\text{Ni(I)}_{\text{ads}}$ adsorb on Zn substrate, $\theta_{\text{Zn}}\theta_4$



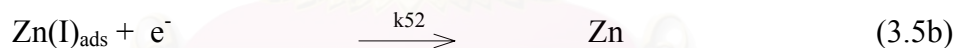
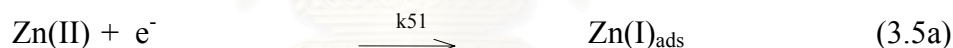
$\text{NiH(I)}_{\text{ads}}$ adsorb on Ni substrate, $\theta_{\text{Ni}}\theta_2$



$\text{Zn(I)}_{\text{ads}}$ adsorb on Zn substrate, $\theta_{\text{Zn}}\theta_6$



$\text{Zn(I)}_{\text{ads}}$ adsorb on Ni substrate, $\theta_{\text{Ni}}\theta_3$



$\text{ZnH(I)}_{\text{ads}}$ adsorb on Zn substrate, $\theta_{\text{Zn}}\theta_5$



Ni(II) and Zn(II) are dissolved in metal ion, hydrolyzed or not. $\text{Ni(I)}_{\text{ads}}$ and $\text{Zn(I)}_{\text{ads}}$, which may or may not contain a hydroxyl group, are monovalent adsorbed reaction intermediate. Ni and Zn are the deposited metal of nickel and zinc respectively.

This substrate model differs from those of Matlosz because it takes into account the deposition of nickel on zinc substrate and zinc on nickel substrate. In

addition, this model explains both the inhibition effect of nickel deposition and the enhancing effect of zinc deposition, observed in Zn-Ni alloy codeposition.

3.1.3.2 Mass Transfer Effect

The model further assumes steady state conditions. Concentration variations are restricted to a thin boundary layer near the electrode surface. Mass transport across this layer is governed by diffusion. Migration effects are considered to be negligible.

The steady state material balances within the diffusion layer for species Ni(II), Zn(II) and H^+ , $0 < x < d$, can be written in order to investigate the concentration in the diffusion layer.

$$\nabla \cdot N_{Ni(II)} = 0 \quad (3.7)$$

$$\nabla \cdot N_{Zn(II)} = 0 \quad (3.8)$$

$$\nabla \cdot N_{H^+} = 0 \quad (3.9)$$

$$K_w = C_{OH^-} \cdot C_{H^+} \quad (3.10)$$

Assuming a constant diffusion coefficient, D , the flux of each species i , in the diffusion layer is $N_i = -D dC_i / dx$. The assumed values of the diffusion coefficients are $4 \times 10^{-10} \text{ m}^2 \text{ s}^{-1}$ for Ni(II), $5.09 \times 10^{-10} \text{ m}^2 \text{ s}^{-1}$ for Zn(II), and $9.3 \times 10^{-9} \text{ m}^2 \text{ s}^{-1}$ for solvated protons, and $5.5 \times 10^{-9} \text{ m}^2 \text{ s}^{-1}$ for hydroxide ions⁵⁹.

The intermediate species, $Ni(I)_{ads}$, NiH^+_{ads} , $Zn(I)_{ads}$ and ZnH^+_{ads} exist only at the electrode surface so their concentration are equal to zero in the solution. At the electrode surface ($x = 0$), the partial current densities are related to the species fluxes by the following reaction:

$$N_{\text{Ni(II)}} - \frac{i_{11}}{F} - \frac{i_{21}}{F} = 0 \quad (3.11)$$

$$N_{\text{Zn(II)}} - \frac{i_{41}}{F} - \frac{i_{51}}{F} = 0 \quad (3.12)$$

$$N_{\text{H}^+} - \frac{i_{31}}{F} - \frac{i_{32}}{F} - \frac{i_{61}}{F} - \frac{i_{62}}{F} = 0 \quad (3.13)$$

At the edge of the Nernst diffusion layer, $x = \delta$, all concentrations are equal to the bulk concentrations values.

$$C_{\text{Ni(II)}}|_{x=\delta} = C_{\text{Ni(II)}}^b \quad (3.14)$$

$$C_{\text{Zn(II)}}|_{x=\delta} = C_{\text{Zn(II)}}^b \quad (3.15)$$

The diffusion layer is assumed to change for all the species according to their diffusion coefficient.

$$\delta_N = \delta_p \left[\frac{D}{\nu} \right]^{1/3}$$

δ_N was determined by the experimental results of Fe(CN)_6^{4-} and Fe(CN)_6^{3-} in solution with the same device of those used in Zn-Ni alloy experiment. The diffusive equation is first discretely and iteratively solved, the calculation is stopped when the relative variation between two consecutive iterations is lower than 1×10^{-5} .

3.1.3.3 Electrochemical Kinetic

Charge transfer kinetics is assumed to obey the Butler Volmer equation. Far from equilibrium, the anodic reaction can be neglected. A modified Tafel expression describing the electrochemical reaction rate on the surface is therefore adapted to calculate the partial current.

As an example, the first step reaction of nickel deposition on nickel substrate, the partial current densities, i_{11} , can be expressed as $i_{11} = -F k_{11}^0 C_{\text{Ni}^{2+}} \theta_{\text{Ni}} (1 - \theta_1 - \theta_2 - \theta_3) \exp(-b_{11} \eta_{11})$. The corresponding electrochemical rate

expressions are summarised in Table 3.1. At steady state, the material balances for the intermediate species yield to equations 3.16 – 3.21. In addition, all the step coverage is constant, so the first and second steps of the reaction give the same rate.

Table 3.1 Electrochemical rate expressions for Zn and Ni alloy simulation

Tafel rate equation		Reaction
i_{11}	$= -F k_{11}^o C_{Ni(II)} \theta_{Ni} (1-\theta_1-\theta_2-\theta_3) \exp(-b_{11}\eta_{11})$	3.1a
i_{12}	$= -F k_{12}^o \theta_{Ni} \theta_1 \exp(-b_{12}\eta_{12})$	3.1b
i_{21}	$= -F k_{21}^o C_{Ni(II)} \theta_{Zn} (1-\theta_4-\theta_5-\theta_6) \exp(-b_{21}\eta_{21})$	3.2a
i_{22}	$= -F k_{22}^o \theta_{Zn} \theta_4 \exp(-b_{22}\eta_{22})$	3.2b
i_{31}	$= -F k_{31}^o C_H^+ \theta_{Ni} (1-\theta_1-\theta_2-\theta_3) \exp(-b_{31}\eta_{31})$	3.3a
i_{32}	$= -F k_{32}^o C_H^+ \theta_{Ni} \theta_2 \exp(-b_{32}\eta_{32})$	3.3b
i_{41}	$= -F k_{41}^o C_{Zn(II)} \theta_{Zn} (1-\theta_4-\theta_5-\theta_6) \exp(-b_{41}\eta_{41})$	3.4a
i_{42}	$= -F k_{42}^o \theta_{Zn} \theta_6 \exp(-b_{42}\eta_{42})$	3.4b
i_{51}	$= -F k_{51}^o C_{Zn(II)} \theta_{Ni} (1-\theta_1-\theta_2-\theta_3) \exp(-b_{51}\eta_{51})$	3.5a
i_{52}	$= -F k_{52}^o \theta_{Ni} \theta_3 \exp(-b_{52}\eta_{52})$	3.5b
i_{61}	$= -F k_{61}^o C_H^+ \theta_{Zn} (1-\theta_4-\theta_5-\theta_6) \exp(-b_{61}\eta_{61})$	3.6a
i_{62}	$= -F k_{62}^o C_H^+ \theta_{Zn} \theta_5 \exp(-b_{62}\eta_{62})$	3.6b

$$\frac{d\theta_1}{dt} = \frac{i_{11}}{F} - \frac{i_{12}}{F} = 0 \quad (3.16)$$

$$\frac{d\theta_2}{dt} = \frac{i_{31}}{F} - \frac{i_{32}}{F} = 0 \quad (3.17)$$

$$\frac{d\theta_3}{dt} = \frac{i_{51}}{F} - \frac{i_{52}}{F} = 0 \quad (3.18)$$

$$\frac{d\theta_4}{dt} = \frac{i_{21}}{F} - \frac{i_{22}}{F} = 0 \quad (3.19)$$

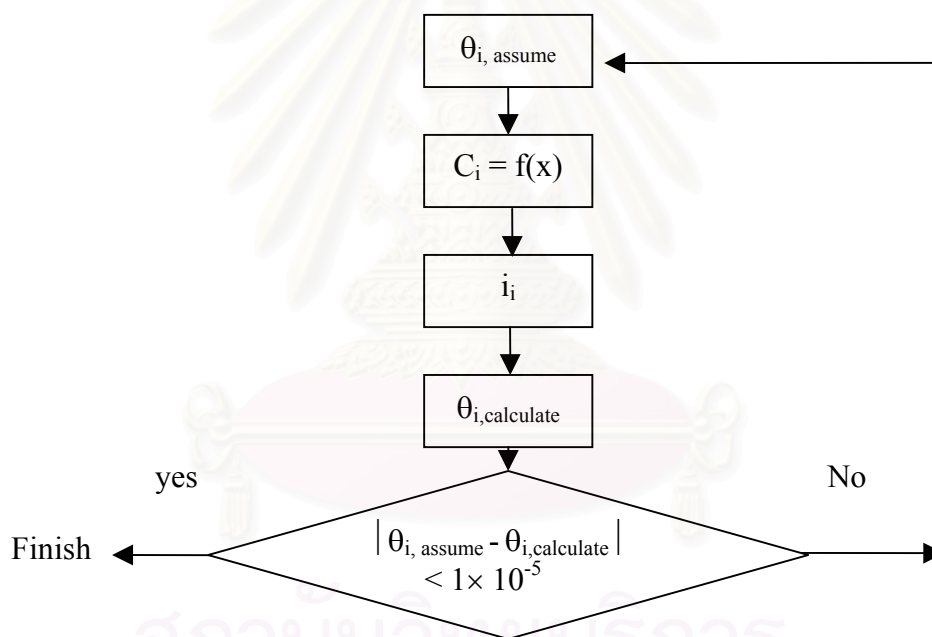
$$\frac{d\theta_5}{dt} = \frac{i_{61}}{F} - \frac{i_{62}}{F} = 0 \quad (3.20)$$

$$\frac{d\theta_6}{dt} = \frac{i_{41}}{F} - \frac{i_{42}}{F} = 0 \quad (3.21)$$

There are ten unknowns in this system, $C_{Ni(II)}$, $C_{Zn(II)}$, C_H^+ , C_{OH^-} , θ_1 , θ_2 , θ_3 , θ_4 , θ_5 , and θ_6 . The system of Eq. 3.11 – 3.21 is solved.

The consecutive reaction model yields such a dependence only when adsorption is low, meaning that the first reaction step is rate limiting. Therefore, in the model calculations it was assumed that the second reaction step (Eq. 3.1b, 3.2b, 3.3b, 3.4b, 3.5b and 3.6b) is fast compared to the first step. (Eq. 3.1a, 3.2a, 3.3a, 3.4a, 3.5a and 3.6a). The rate constants determined from the single metal deposition, were used for the simulation of alloy deposition.

As the organigram given below, the different kinetic parameters are further determined by fitting the experimental data of elemental simulation.



After the simulation is completed, the partial current densities for each metal and side reaction are determined from Eq. 3.22 – 3.29

$$i_{Ni} = i_{11} + i_{12} + i_{21} + i_{22} \quad (3.22)$$

$$i_{Zn} = i_{41} + i_{42} + i_{51} + i_{52} \quad (3.23)$$

$$i_{H_2/Ni} = i_{31} + i_{32} \quad (3.24)$$

$$i_{\text{H}_2/\text{Zn}} = i_{61} + i_{62} \quad (3.25)$$

$$\eta = (i_{\text{Ni}} \pm i_{\text{Zn}}) / (i_{\text{Ni}} \pm i_{\text{Zn}} + i_{\text{H}_2}) \quad (3.26)$$

$$\theta_{\text{Ni}} = i_{\text{Ni}} / (i_{\text{Ni}} + i_{\text{Zn}}) \quad (3.27)$$

$$\theta_{\text{Zn}} = i_{\text{Zn}} / (i_{\text{Ni}} + i_{\text{Zn}}) \quad (3.28)$$

$$\theta_{\text{Ni}} + \theta_{\text{Zn}} = 1 \quad (3.29)$$

3.1.4 Elemental Simulation

To determine the kinetic parameters necessary for alloy deposition modelling, the elemental simulation is developed. Overall, the deposition can be divided into four elemental mechanisms with respect to the assumption of substrate effect; nickel deposition on nickel substrate, zinc deposition on zinc substrate, nickel deposition on zinc substrate, and zinc deposition on nickel substrate.

3.1.4.1 Nickel Deposition on Nickel Substrate

3.1.4.1a Mechanism Model

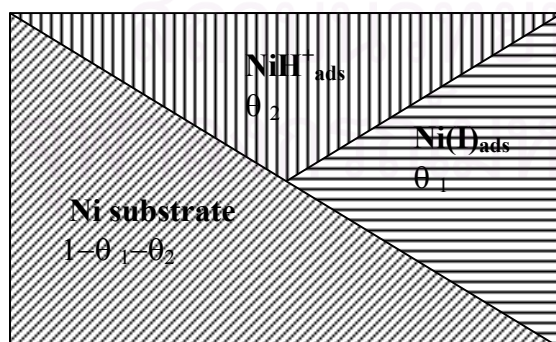
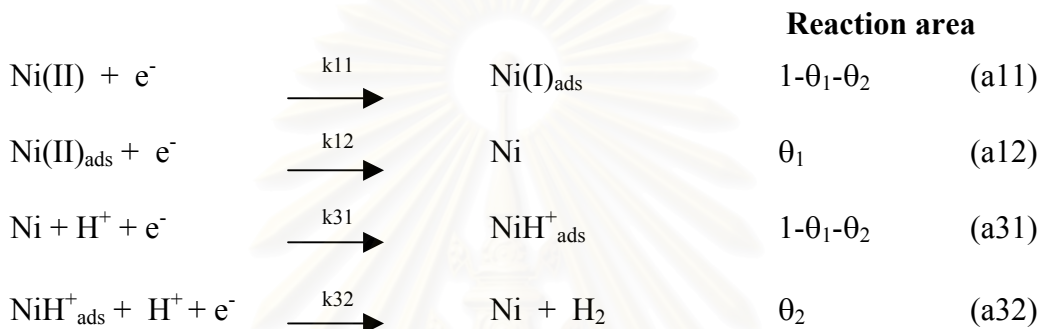


Figure 3.2 Scheme of nickel deposition on nickel substrate

Figure 3.2 shows the diagram representing nickel deposition on nickel substrate. The nickel sheet is divided into three parts. The first part, θ_1 , corresponds to the area concerned by the adsorbed reaction intermediate of $\text{Ni(I)}_{\text{ads}}$. The second part is the surface fraction θ_2 occupying by the adsorbed species $\text{NiH}^+_{\text{ads}}$. The third part is the fraction of free surface area, $(1-\theta_1-\theta_2)$.

The following reduction reactions are assumed to take place.



3.1.4.1b Mass Transfer Effect

The assumptions of Zn-Ni alloy are applied for Ni-Ni. In this case, the material balances within the diffusion layer, $0 < x < \delta$, are as follows:

$$\nabla \cdot \mathbf{N}_{\text{Ni(II)}} = 0 \quad (\text{a1})$$

$$\nabla \cdot \mathbf{N}_{\text{H}^+} = 0 \quad (\text{a2})$$

$$\nabla \cdot \mathbf{N}_{\text{OH}^-} = 0 \quad (\text{a3})$$

$$K_{\text{w}} = C_{\text{OH}^-} \cdot C_{\text{H}^+} \quad (\text{a4})$$

Assuming a constant diffusion coefficient, D , the flux of each species i , in the diffusion layer is $N_i = -D \, dC_i / dx$. The assumed values of the diffusion coefficients are $4 \times 10^{-10} \text{ m}^2 \text{ s}^{-1}$ for Ni(II) , $5.09 \times 10^{-10} \text{ m}^2 \text{ s}^{-1}$ for solvated protons, and $5.5 \times 10^{-9} \text{ m}^2 \text{ s}^{-1}$ for hydroxide ions⁵⁹.

At the electrode surface ($x = 0$), the partial current densities are related to the species fluxes by the following reactions:

$$N_{\text{Ni(II)}} - \frac{i_{11}}{F} = 0 \quad (\text{a5})$$

$$N_{\text{H}^+} - \frac{i_{31}}{F} - \frac{i_{32}}{F} = 0 \quad (\text{a6})$$

At the edge of the Nernst diffusion layer ($x = \delta$), all concentrations are equal to the bulk concentrations values

$$C_{\text{Ni(II)}}|_{x=\delta} = C_{\text{Ni(II)}}^b \quad (\text{a7})$$

$$C_{\text{H}^+}|_{x=\delta} = C_{\text{H}^+}^b \quad (\text{a8})$$

At steady state, the species arrive at the electrode surface by diffusion layer and are consumed according to the reactions a5 and a6.

3.1.4.1c Electrochemical Kinetic

This part is dedicated to the determination of the different parameter involved in the electrochemistry considered for Zn-Ni alloy deposition, the same laws (Tafel laws) are used here. The corresponding electrochemical rate expressions are summarized in Table 3.2

Table 3.2 Electrochemical rate expressions for nickel deposition on nickel substrate simulation

Tafel rate equation	Reaction
$i_{11} = -F k_{11}^0 C_{\text{Ni(II)}} (1-\theta_1-\theta_2) \exp(-b_{11}\eta_{11})$	a11
$i_{12} = -F k_{12}^0 \theta_1 \exp(-b_{12}\eta_{12})$	a12
$i_{31} = -F k_{31}^0 C_{\text{H}^+} (1-\theta_1-\theta_2) \exp(-b_{31}\eta_{31})$	a31
$i_{32} = -F k_{32}^0 C_{\text{H}^+} \theta_2 \exp(-b_{32}\eta_{32})$	a32

There are five unknowns in this system, $C_{\text{Ni(II)}}$, C_{H^+} , C_{OH^-} , θ_1 , and θ_2 . The system of Eqs. a1-a8 is solved for different potentials. After the simulation is completed the partial current densities for nickel metal and the side reactions are determined from Eq. a9-a10.

$$i_{\text{Ni}} = i_{11} + i_{12} \quad (\text{a9})$$

$$i_{\text{H}_2/\text{Ni}} = i_{31} + i_{32} \quad (\text{a10})$$

To determine the different electrochemical constants, two times of operating are needed. Firstly, curve of $\log i$ versus E in which i corresponds to the partial current density of the reaction is drawn. From this curve, Tafel slope and equilibrium potential of the considered reaction are determined, assuming Tafel slope and equilibrium potential of the second step is equal to the first step.

In a second time, the first reaction is assumed to be a limiting step, so the kinetic parameter of the second step is 10^{10} higher than the first one. The electrochemical kinetic parameter of the first step, is determined by trial & error method using the same routine presented for Zn-Ni alloy. Table 3.3 reports the value of different kinetic parameters that have been determined by this procedure.

Table 3.3 Kinetic parameters of Ni₂Ni and H₂Ni

Reaction constants	Inverse Tafel slope, V ⁻¹	Reactions
$k_{11} = 9.89 \times 10^{-7} \text{ cm s}^{-1}$	$b_{11} = 6.05$	a11
$k_{12} = 9.89 \times 10^2 \text{ mol cm}^{-2} \text{ s}^{-1}$	$b_{12} = 6.05$	a12
$k_{31} = 3.00 \times 10^{-3} \text{ cm s}^{-1}$	$b_{31} = 3.8$	a31
$k_{32} = 3.00 \times 10^6 \text{ mol cm}^{-2} \text{ s}^{-1}$	$b_{32} = 3.8$	a32

Figures 3.3 and 3.4 provide a comparison of the simulation results to the experimental data for Ni₂Ni and H₂Ni system at a flow rate of $7.26 \times 10^{-6} \text{ m}^3/\text{s}$ and pH 4. Nickel and zinc concentrations are 0.05 M.

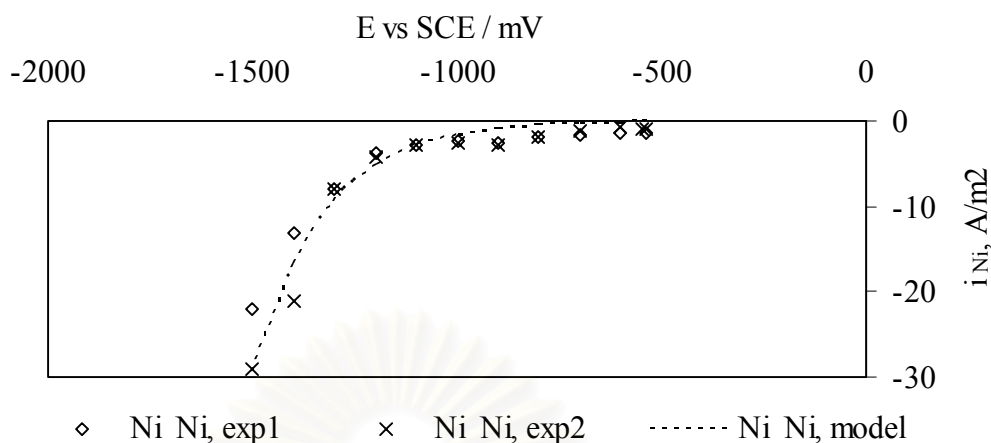


Figure 3.3 The experiment and model simulation of Ni_Ni. (Dashed line stands for simulation results and symbols for experimental measurements)

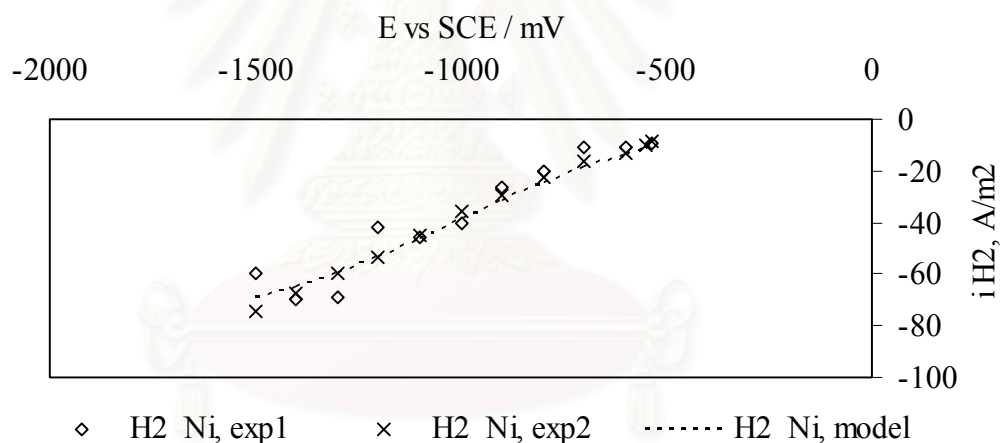


Figure 3.4 The experiment and model simulation of H₂_Ni (Dashed line stands for simulation results and symbols for experimental measurements)

From these figures, it appears that the experimental result is agreed with the theoretical result. This means that the kinetic parameter and the approach are correct.

After determining the equilibrium potential, kinetic parameters for nickel deposition on nickel substrate are investigated, as the same as the study for zinc deposition on zinc substrate.

3.1.4.2 Zinc Deposition on Zinc Substrate

3.1.4.2a Mechanism Model

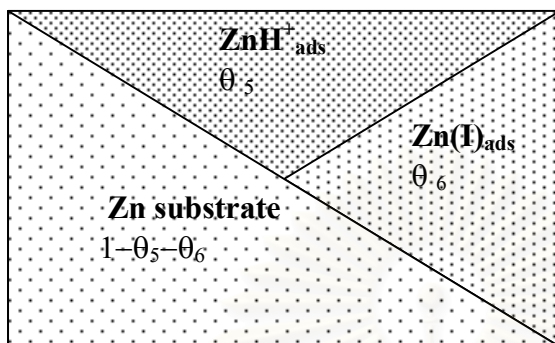
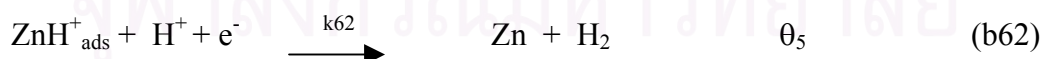
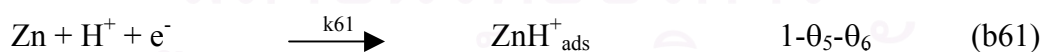
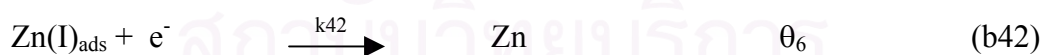
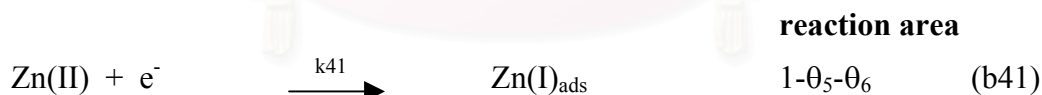


Figure 3.5 Scheme of zinc deposition on zinc substrate

Figure 3.5 shows the diagram representing zinc deposition on zinc substrate. The zinc sheet is divided into three parts. The first part is the adsorbed reaction intermediate of $\text{Zn(I)}_{\text{ads}}$ depositing on nickel substrate occupy a fraction θ_6 . The second part is the surface fraction θ_5 occupying by the adsorbed specie $\text{ZnH}^+_{\text{ads}}$. The third part is thus the fraction of free surface area, $(1-\theta_5-\theta_6)$.

The following reduction reactions are assumed to take place.



3.1.4.2b Mass Transfer Effect

The same assumptions that those hypothesized for Zn=Ni alloy are made. In this case, the material balances within the diffusion layer, $0 < x < d$, can be written

$$\nabla \cdot N_{Zn(II)} = 0 \quad (b1)$$

$$\nabla \cdot N_{H^+} = 0 \quad (b2)$$

$$\nabla \cdot N_{OH^-} = 0 \quad (b3)$$

$$K_W = C_{OH^-} \cdot C_{H^+} \quad (b4)$$

Assuming a constant diffusion coefficient, D , the flux of each species i , in the diffusion layer is $N_i = -D \, dC_i / dx$. The assumed values of the diffusion coefficients are $4 \times 10^{-10} \, m^2 \, s^{-1}$ for Zn(II), and $9.3 \times 10^{-9} \, m^2 \, s^{-1}$ for solvated protons, and $5.5 \times 10^{-9} \, m^2 \, s^{-1}$ for hydroxide ions⁵⁹.

At the electrode surface ($x = 0$), the partial current densities are related to the species fluxes by the following reaction:

$$N_{Zn(II)} - \frac{i_{41}}{F} = 0 \quad (b5)$$

$$N_{H^+} - \frac{i_{61}}{F} - \frac{i_{62}}{F} = 0 \quad (b6)$$

At the edge of the Nernst diffusion layer ($x = \delta$), all concentrations are equal to the bulk concentrations values.

$$C_{Zn(II)}|_{x=\delta} = C_{Zn(II)}^b \quad (b7)$$

$$C_{H^+}|_{x=\delta} = C_{H^+}^b \quad (b8)$$

3.1.4.2c Electrochemical Kinetic

This part is dedicated to the determination of the different parameter involved in the electrochemistry considered for Zn-Ni alloy deposition, the same laws (Tafel laws) are used here. The corresponding electrochemical rate expressions are summarized in Table 3.4

Table 3.4 Electrochemical rate expressions for zinc deposition on zinc substrate simulation

Tafel rate equation	Reaction
$i_{41} = -F k_{41}^0 C_{Zn(II)} (1-\theta_5-\theta_6) \exp(-b_{41}\eta_{41})$	b41
$i_{42} = -F k_{42}^0 \theta_6 \exp(-b_{42}\eta_{42})$	b42
$i_{61} = -F k_{61}^0 C_{H^+} (1-\theta_5-\theta_6) \exp(-b_{61}\eta_{61})$	b61
$i_{62} = -F k_{62}^0 C_{H^+} \theta_5 \exp(-b_{62}\eta_{62})$	b62

There are five unknowns in this system, $C_{Zn(II)}$, C_{H^+} , C_{OH^-} , θ_5 , and θ_6 . The system of Eq.b1-b8 is solved for different potentials. After the simulation is completed the partial current densities for zinc metal and the side reaction are determined from Eq. b9-b10

$$i_{Zn} = i_{41} + i_{42} \quad (b9)$$

$$i_{H_2/Zn} = i_{61} + i_{62} \quad (b10)$$

Table 3.5 reports the values of different kinetic parameters that have been determined with respect to this procedure and that will be used in further calculation.

Table 3.5 Kinetic parameters of Zn_Zn and H₂_Zn

Reaction constants	Inverse Tafel slope, V ⁻¹	Reactions
$k_{41} = 7.51 \times 10^{-6} \text{ cm s}^{-1}$	$b_{41} = 10$	b41
$k_{42} = 7.51 \times 10^3 \text{ mol cm}^{-2} \text{ s}^{-1}$	$b_{43} = 10$	b42
$k_{61} = 3.00 \times 10^{-2} \text{ cm s}^{-1}$	$b_{61} = 1.5$	b61
$k_{62} = 3.00 \times 10^7 \text{ mol cm}^{-2} \text{ s}^{-1}$	$b_{62} = 1.5$	b62

Figure 3.6 and 3.7 compare the model simulation to the experimental results for the Zn_Zn and H₂_Zn system at $7.26 \times 10^{-6} \text{ m}^3/\text{s}$ and pH of 4. The nickel and zinc

concentrations are 0.05 M. The kinetic parameters obtained by Tafel law can fit well with the experimental data and are listed in Table 3.5.

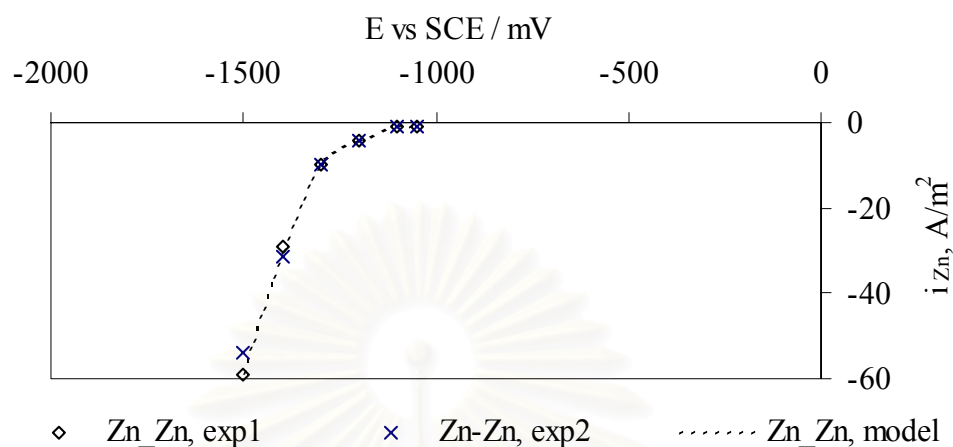


Figure 3.6 The experimental and model simulation of Zn_Zn (Line stands for simulation and symbols for measurement)

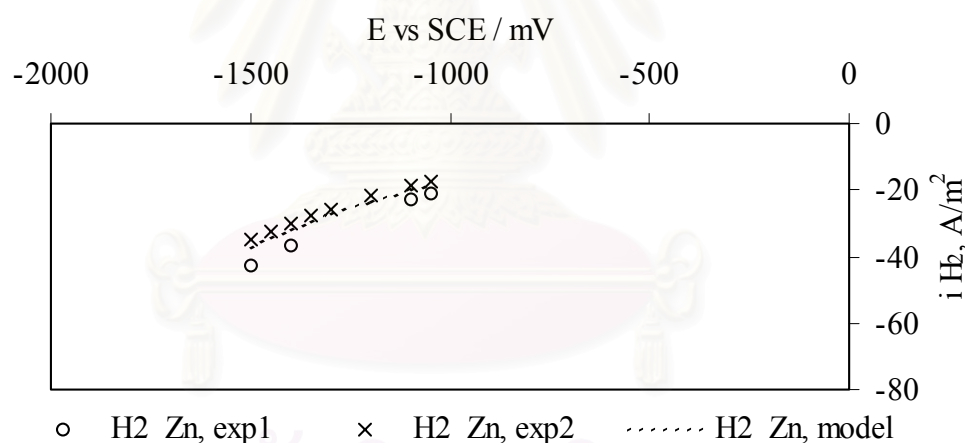


Figure 3.7 The experimental and model simulation of H₂_Zn (Line stands for simulation and symbols for measurement)

From these figures, it appears that the experimental result is agreed with theoretical result. This means that the kinetic parameter and the approach are correct.

Figure 3.8 presents the total current versus time duration of the elemental deposition, Zn_Ni and Ni_Zn. The total current of Zn_Ni less than Ni_Zn is due to the more hydrogen evolution catalyzed by nickel substrate. It appears that the total currents of Zn_Ni and Ni_Zn change with time. The composition of the surface

therefore changes versus time and the system is not under the steady-state control. Deposition of zinc on the different substrate (in this case is nickel) or deposition of nickel on the different substrate (in this case is zinc) leads to the composition and total current, changing with time. The kinetic of zinc on nickel is only short initial state of the process. Afterwards, Zinc can quickly deposit on its own substrate. As this result, there is a difficulty determining the kinetic constant from this kind of behavior.

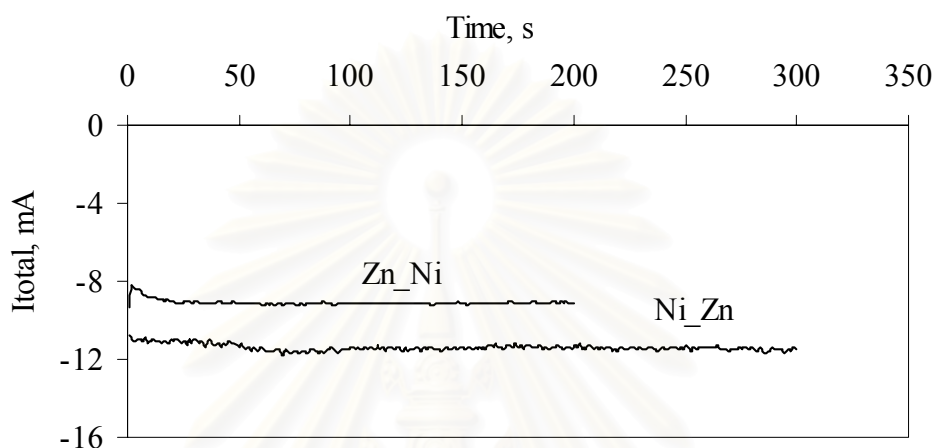


Figure 3.8 Chronoamperogram of Zn-Ni and Ni_Zn elemental deposition at $E_{app} = -1.5$ V/SCE

3.1.4.3 Nickel Deposition on Zinc Substrate

3.1.4.3a Mechanism Model

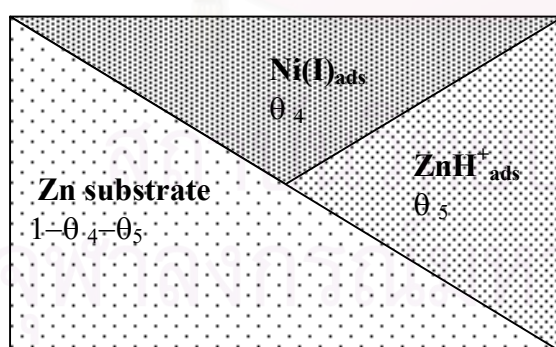
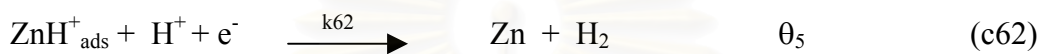
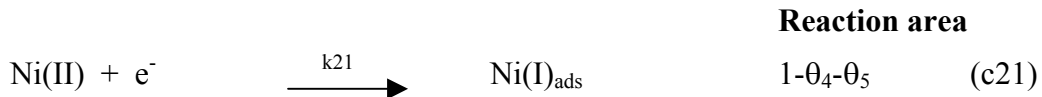


Figure 3.9 Sketch of the mechanism assumed for nickel deposition on zinc substrate

Figure 3.9 shows the diagram representing nickel deposition on zinc substrate. The zinc sheet is divided into three parts. The first part is the adsorbed reaction intermediate of Ni(I)_{ads} depositing on zinc substrate occupy a fraction θ_4 . The second

part is the surface fraction θ_5 occupying by the adsorbed specie $\text{ZnH}_{\text{ads}}^+$. The third part is thus the fraction of free surface area, $(1-\theta_4-\theta_5)$.

The following reduction reactions are assumed to take place.



3.1.4.3b Mass Transfer Effect

The same assumptions that those hypothesized for Zn-Ni alloy are made. In this case, the material balances within the diffusion layer, $0 < x < d$, can be written.

$$\nabla \cdot \mathbf{N}_{\text{Ni(II)}} = 0 \quad (\text{c1})$$

$$\nabla \cdot \mathbf{N}_{\text{H}^+} = 0 \quad (\text{c2})$$

$$\nabla \cdot \mathbf{N}_{\text{OH}^-} = 0 \quad (\text{c3})$$

$$K_{\text{W}} = C_{\text{OH}^-} \cdot C_{\text{H}^+} \quad (\text{c4})$$

Assuming a constant diffusion coefficient, D , the flux of each species i , in the diffusion layer is $N_i = -D \, dC_i / dx$. The assumed values of the diffusion coefficients are $4 \times 10^{-10} \, \text{m}^2 \, \text{s}^{-1}$ for Ni(II), and $9.3 \times 10^{-9} \, \text{m}^2 \, \text{s}^{-1}$ for solvated protons, and $5.5 \times 10^{-9} \, \text{m}^2 \, \text{s}^{-1}$ for hydroxide ions⁵⁹.

At the electrode surface ($x = 0$), the partial current densities are related to the species fluxes by the following reactions:

$$N_{\text{Ni(II)}} - \frac{i_{21}}{F} = 0 \quad (\text{c5})$$

$$N_{\text{H}^+} - \frac{i_{61}}{F} - \frac{i_{62}}{F} = 0 \quad (\text{c6})$$

At the edge of the Nernst diffusion layer ($x = \delta$), concentrations are equal to the bulk concentrations values.

$$C_{\text{Ni(II)}}|_{x=\delta} = C_{\text{Ni(II)}}^b \quad (\text{c7})$$

$$C_{\text{H}^+}|_{x=\delta} = C_{\text{H}^+}^b \quad (\text{c8})$$

3.1.4.3(c) Electrochemical Kinetic

This part is to determine the different parameter involving in the electrochemistry laws, considered for Zn-Ni alloy deposition. The same laws (Tafel laws) applied and the corresponding electrochemical rate expressions are summarized in Table 3.6

Table 3.6 Electrochemical rate expressions for nickel deposition on zinc substrate simulation

Tafel rate equation	Reaction
$i_{21} = -F k_{21}^0 C_{\text{Ni(II)}}(1-\theta_4-\theta_5) \exp(-b_{21}\eta_{21})$	c21
$i_{22} = -F k_{22}^0 \theta_4 \exp(-b_{22}\eta_{22})$	c22
$i_{61} = -F k_{61}^0 C_{\text{H}^+}(1-\theta_4-\theta_5) \exp(-b_{61}\eta_{61})$	c61
$i_{62} = -F k_{62}^0 C_{\text{H}^+} \theta_5 \exp(-b_{62}\eta_{62})$	c62

There are five unknowns in this system, $C_{\text{Ni(II)}}$, C_{H^+} , C_{OH^-} , θ_4 , and θ_5 . The system of Eq.c1-c8 is solved for different potentials. After the simulation is completed the partial current densities for zinc metal and the side reaction are determined from Eq. c9-c10

$$i_{\text{Ni}} = i_{21} + i_{22} \quad (\text{c9})$$

$$i_{\text{H}_2/\text{Zn}} = i_{61} + i_{62} \quad (\text{c10})$$

Table 3.7 reports the values of different kinetic parameters that have been determined with respect to this procedure and will be used in further calculation.

Table 3.7 Kinetic parameters of Ni_Zn and H₂_Zn

Reaction constants			Inverse Tafel slope, V ⁻¹		Reactions	
k ₂₁	=	2.33×10 ⁻⁵ cm s ⁻¹	b ₂₁	=	3.6	c21
k ₂₂	=	2.33×10 ⁴ mol cm ⁻² s ⁻¹	b ₂₂	=	3.6	c22
k ₆₁	=	3.00×10 ⁻² cm s ⁻¹	b ₆₁	=	1.5	c61
k ₆₂	=	3.00×10 ⁷ mol cm ⁻² s ⁻¹	b ₆₂	=	1.5	c62

Figure 3.10 and 3.11 compare the model simulation to the experimental results for the Ni_Zn and H₂_Zn system at 7.26×10⁻⁶ m³/s and pH 4. The nickel and zinc concentrations are 0.05 M. The kinetic parameter obtained by Tafel law can fit well with the experimental data and are listed in Table 3.7.

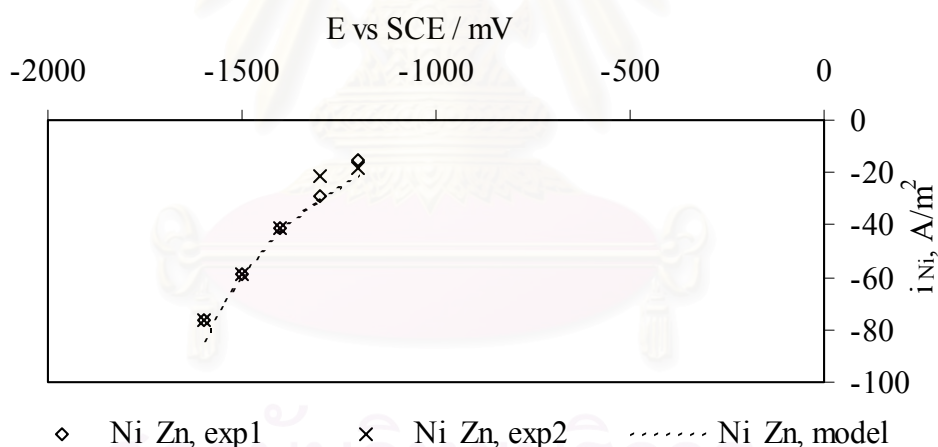


Figure 3.10 The experimental and model simulation of Ni_Zn (Line stands for simulation and symbols for measurement)

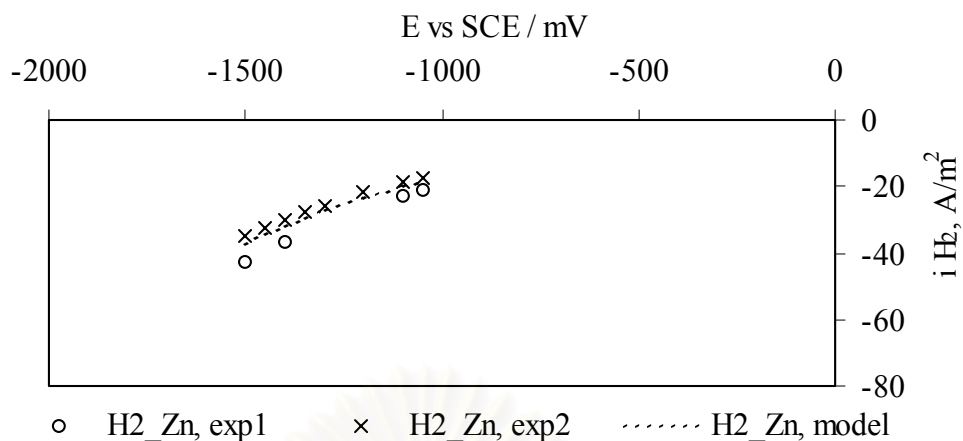


Figure 3.11 The experimental and model simulation of H_2_Zn (Line stands for simulation and symbols for measurement)

From these figures, it appears that the experimental result is agreed with the theoretical result. This means that the kinetic parameter and the approach are correct.

3.1.4.4 Zinc Deposition on Nickel Substrate

3.1.4.4a Mechanism Model

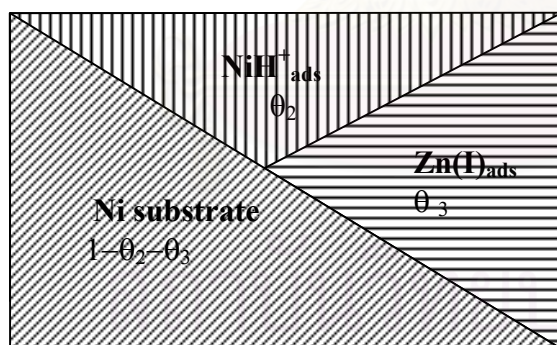
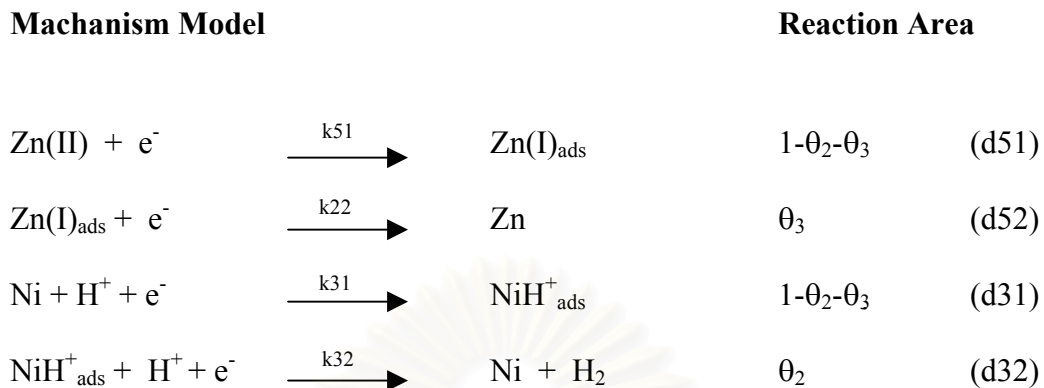


Figure 3.12 Sketch of the mechanism assumed for zinc deposition on nickel substrate

Figure 3.12 shows a diagram representing zinc deposition on nickel substrate. The nickel sheet is divided into three parts. The first part is the adsorbed reaction intermediate of $Zn(I)_{ads}$ depositing on nickel substrate occupy a fraction θ_3 . The second part is the surface fraction θ_2 occupying by the adsorbed specie NiH^+_{ads} . The third part is thus the fraction of free surface area, $(1-\theta_2-\theta_3)$.

The following reduction reactions are assumed to take place.



3.1.4.4b Mass Transfer Effect

The same assumptions that those hypothesized for Zn-Ni alloy are made. In this case, the material balances within the diffusion layer, $0 < x < d$, can be written.

$$\nabla \cdot N_{\text{Zn(II)}} = 0 \quad (\text{d1})$$

$$\nabla \cdot N_{\text{H}^+} = 0 \quad (\text{d2})$$

$$\nabla \cdot N_{\text{OH}^-} = 0 \quad (\text{d3})$$

$$K_{\text{W}} = C_{\text{OH}^-} \cdot C_{\text{H}^+} \quad (\text{d4})$$

Assuming a constant diffusion coefficient, D , the flux of each species i , in the diffusion layer is $N_i = -D \, dC_i / dx$. The assumed values of the diffusion coefficients are $4 \times 10^{-10} \text{ m}^2 \text{ s}^{-1}$ for Zn(II), and $9.3 \times 10^{-9} \text{ m}^2 \text{ s}^{-1}$ for solvated protons, and $5.5 \times 10^{-9} \text{ m}^2 \text{ s}^{-1}$ for hydroxide ions⁵⁹.

At the electrode surface ($x = 0$), the partial current densities are related to the species fluxes by the following reaction:

$$N_{\text{Zn(II)}} - \frac{i_{51}}{F} = 0 \quad (\text{d5})$$

$$N_{\text{H}^+} - \frac{i_{31}}{F} - \frac{i_{32}}{F} = 0 \quad (\text{d6})$$

At the edge of the Nernst diffusion layer ($x = \delta$) all concentrations are equal to the bulk concentrations values.

$$C_{Zn(II)}|_{x=\delta} = C_{Zn(II)}^b \quad (d7)$$

$$C_{H^+}|_{x=\delta} = C_{H^+}^b \quad (d8)$$

3.1.4.4c Electrochemical Kinetic

At this part is to determine the different parameter involved in the electrochemistry laws considered for Zn-Ni alloy deposition, the same laws (Tafel laws) are used here. The corresponding electrochemical rate expressions are summarized in Table 3.8

Table 3.8 Electrochemical rate expressions for zinc deposition on nickel substrate simulation

Tafel rate equation	Reaction
$i_{51} = -F k_{51}^0 C_{Zn^{2+}} (1-\theta_2-\theta_3) \exp(-b_{51}\eta_{51})$	d51
$i_{52} = -F k_{52}^0 \theta_3 \exp(-b_{52}\eta_{52})$	d52
$i_{31} = -F k_{31}^0 C_{H^+} (1-\theta_2-\theta_3) \exp(-b_{31}\eta_{31})$	d31
$i_{32} = -F k_{32}^0 C_{H^+} \theta_2 \exp(-b_{32}\eta_{32})$	d32

There are five unknowns in this system, $C_{Zn(II)}$, C_{H^+} , C_{OH^-} , θ_2 , and θ_3 . The system of Eq.d1-d8 is solved for different potentials. After the simulation is completed the partial current densities for zinc metal and the side reaction are determined from Eq. d9-d10

$$i_{Zn} = i_{51} + i_{52} \quad (d9)$$

$$i_{H2/Ni} = i_{31} + i_{32} \quad (d10)$$

Table 3.9 reports the values of different kinetic parameters that have been determined by this procedure and that will be used in further calculation.

Table 3.9 Kinetic parameters of Zn₂Ni and H₂Ni

Reaction constants			Inverse Tafel slope, V ⁻¹		Reactions	
k ₅₁	=	1.67×10 ⁻⁵ cm s ⁻¹	b ₅₁	=	9.8	d51
k ₅₂	=	1.67×10 ⁴ mol cm ⁻² s ⁻¹	b ₅₂	=	9.8	d52
k ₃₁	=	3.00×10 ⁻³ cm s ⁻¹	b ₃₁	=	3.8	a31
k ₃₂	=	3.00×10 ⁶ mol cm ⁻² s ⁻¹	b ₃₂	=	3.8	a32

Figures 3.13 and 3.14 compare the model simulation to the experimental results for the Zn₂Ni and H₂Ni system at 7.26×10⁻⁶ m³/s and pH of 4. Nickel and zinc concentrations are 0.05 M. The kinetic parameters obtained by Tafel law can fit well with the experimental data and are listed in Table 3.9.

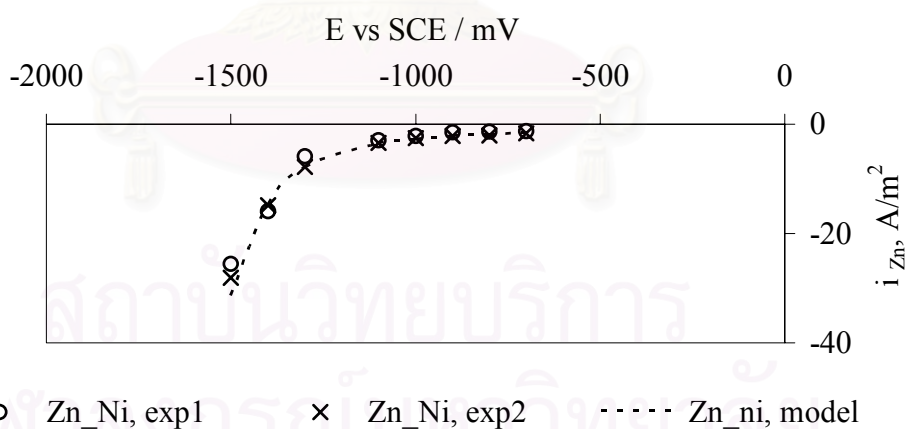


Figure 3.13 The experimental and model simulation of Zn₂Ni (Line stands for simulation and symbols for measurement)

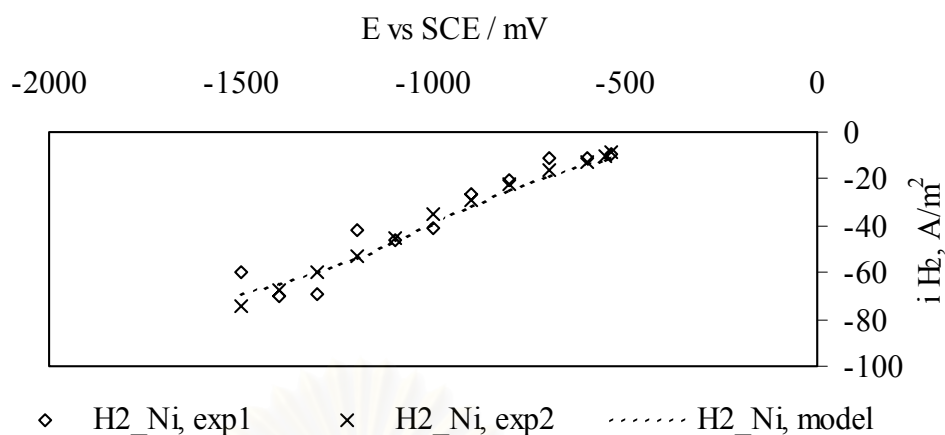


Figure 3.14 The experimental and model simulation of H₂_Ni (Line stands for simulation and symbols for measurement)

From these figures, it appears that the experimental result is agreed with the theoretical result. This means that the kinetic parameter and the procedure are correct.

3.1.5 Results of the Global Model

According to the assumption of substrate effect, nickel deposition on nickel substrate, zinc deposition on zinc substrate, nickel deposition on zinc substrate, and zinc deposition on nickel substrate are carried out in elemental simulation. After determining the electrochemical parameter for individual deposits, these parameters have been in a model of the alloy deposition. The partial current simulations are compared with the experimental data in the following section.

3.1.5.1 Comparison between Experimental Results and Theoretical Results

3.1.5.1a With Previously Determined Kinetic Parameters from Elemental Deposition

The kinetic parameters of each elemental mechanisms that have been previously determined, are now used to model the alloy deposition regarding the proposed mechanisms. Comparison between the partial current densities of nickel, zinc and hydrogen from model simulation and the experimental results of the Zn-Ni

system at $7.26 \text{ cm}^3 \text{ s}^{-1}$ and $\text{pH} = 4$ is presented in Figures 3.15, 3.16 and 3.17. Nickel and zinc concentrations are 0.05 M . From these figures, it appears that the partial currents of zinc, nickel and hydrogen evolution differ significantly from the experiments. The simulated partial current densities of zinc are less than the experimental observations, while the simulated partial current densities of nickel and hydrogen are higher than the experimental results. Figure 3.18 shows a comparison between the simulation results and experimental results of the deposited nickel percentage, the higher value for simulation is also observed.

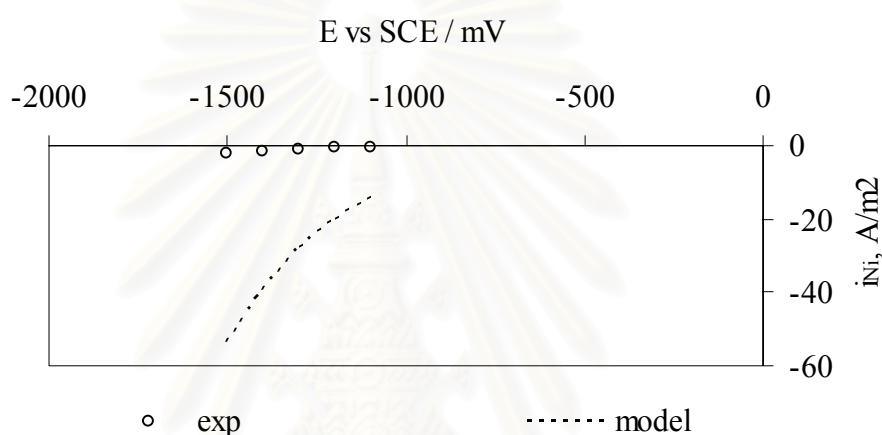


Figure 3.15 Nickel partial current density in alloy simulation and experimental data; C_{Ni} and $C_{\text{Zn}} = 0.05 \text{ M}$, $7.26 \text{ cm}^3 \text{ s}^{-1}$ pH of 4

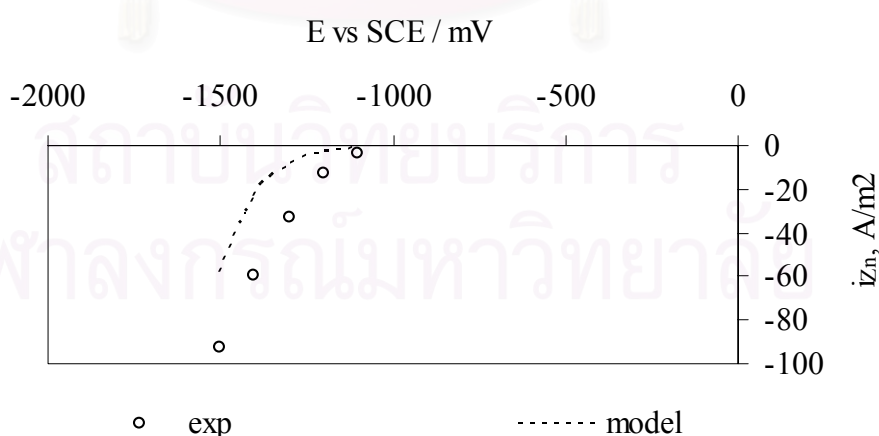


Figure 3.16 Zinc partial current density in alloy simulation and experimental data; C_{Ni} and $C_{\text{Zn}} = 0.05 \text{ M}$, $7.26 \text{ cm}^3 \text{ s}^{-1}$ pH of 4

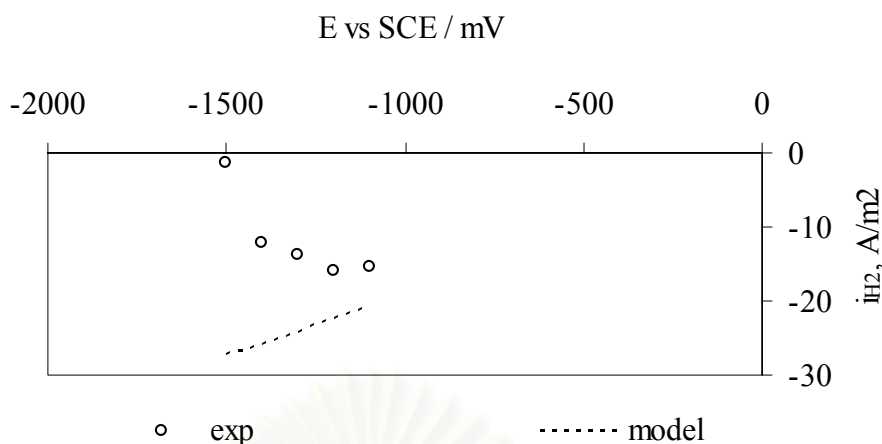


Figure 3.17 Hydrogen partial current density in alloy simulation and experimental data; C_{Ni} and $C_{Zn} = 0.05$ M, $7.26 \text{ cm}^3 \text{ s}^{-1}$ pH of 4

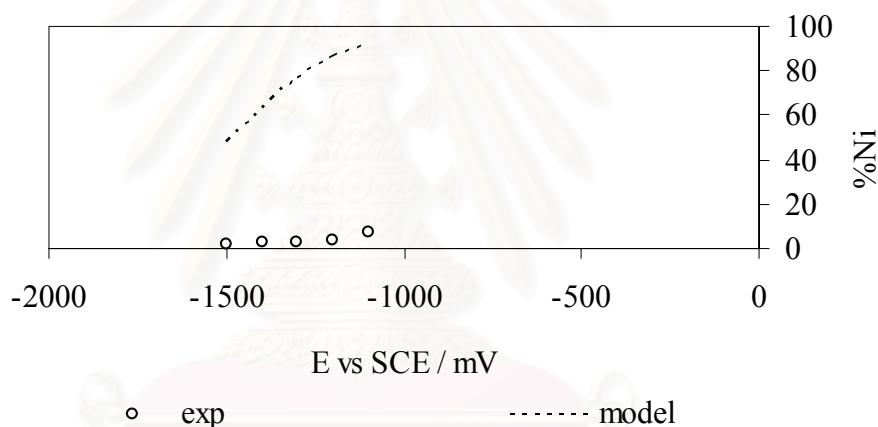


Figure 3.18 Percentage of nickel in alloy simulation and experimental data; C_{Ni} and $C_{Zn} = 0.05$ M, $7.26 \text{ cm}^3 \text{ s}^{-1}$ pH of 4

The difference between the experiments and simulation results can be explained by the uncertainty kinetic constants obtained for the Tafel law in zinc deposition on nickel substrate, and nickel deposition on zinc substrate elemental deposition.

For Zn_Zn and Ni_Ni elemental deposition, it is supposed that there is no change of deposit structure with time. Consequently, the composition of the deposit does not change with time, or the system is under steady-state control. The rate constants can be directly calculated from the Tafel slopes.

For Zn_Ni and Ni_Zn, there is the problem to determine the kinetic constant according to the composition change with time. The Tafel law cannot be taken into account for estimating a kinetic value. The kinetic parameter is determined to fit well with the experimental data of Zn_Ni and Ni_Zn.

3.1.5.1b Results Obtained by Trial & Error Method

According to the sensitivity analysis, the kinetic constant has less an effect on the model variation comparing with the Tafel slope. The kinetic constants are thus modified by Trial & Error method. The kinetic constant of Ni_Zn is first determined by a Trial & Error method, using mathematical function of goal-seek method. This value was changed until the current density of nickel fit well with the experimental results. The same routine is made for the kinetic constant of zinc deposition on nickel substrate.

Then, the kinetic constants are further used in the simulation. These constants are listed in Table 3.10. Only kinetic constants linked with Ni_Zn and Zn_Ni: k_{21} , k_{22} , k_{51} , and k_{52} , are changed.

Table 3.10 Kinetic parameters

Reaction constants	Inverse Tafel slope, V^{-1}	Reactions
$k_{11} = 9.89 \times 10^{-7}$	$b_{11} = 6.05$	a11
$k_{12} = 9.89 \times 10^2$	$b_{12} = 6.05$	a12
$k_{21} = 4.20 \times 10^{-7}$	$b_{21} = 3.6$	c21
$k_{22} = 4.20 \times 10^2$	$b_{22} = 3.6$	c22
$k_{31} = 3.00 \times 10^{-3}$	$b_{31} = 3.8$	a31
$k_{32} = 3.00 \times 10^6$	$b_{32} = 3.8$	a32
$k_{41} = 7.51 \times 10^{-6}$	$b_{41} = 10$	b41
$k_{42} = 7.51 \times 10^3$	$b_{43} = 10$	b42
$k_{51} = 3.04 \times 10^{-4}$	$b_{51} = 9.8$	d51
$k_{52} = 3.04 \times 10^5$	$b_{52} = 9.8$	d52
$k_{61} = 3.00 \times 10^{-2}$	$b_{61} = 1.5$	b61
$k_{62} = 3.00 \times 10^7$	$b_{62} = 1.5$	b62

Figures 3.19, 3.20 and 3.21 show the comparison of the partial current densities of zinc, nickel and hydrogen evolution by the estimated kinetic constants determined experimentally and those coming from the experimental result. In particular, these models found the enhancement of the zinc deposition and the inhibiting of the nickel deposition. From these figures, it appears that the modelling results fit well with the experimental data. Figure 3.22 shows also the percentage of the deposited nickel content observation

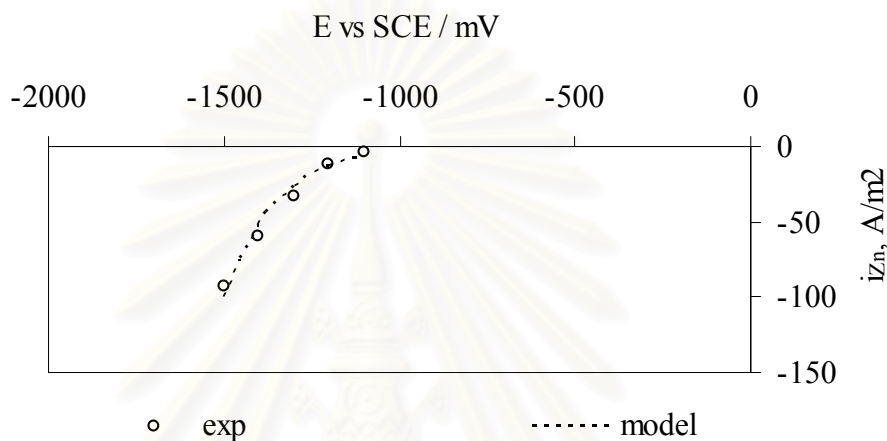


Figure 3.19 Partial current density of zinc in alloy simulation and experimental obtained by Trial & Error method for the kinetic constant of Zn_Ni and Ni_Zn;
 C_{Ni} and $C_{Zn} = 0.05$ M, $7.26 \text{ cm}^3 \text{ s}^{-1}$, pH of 4

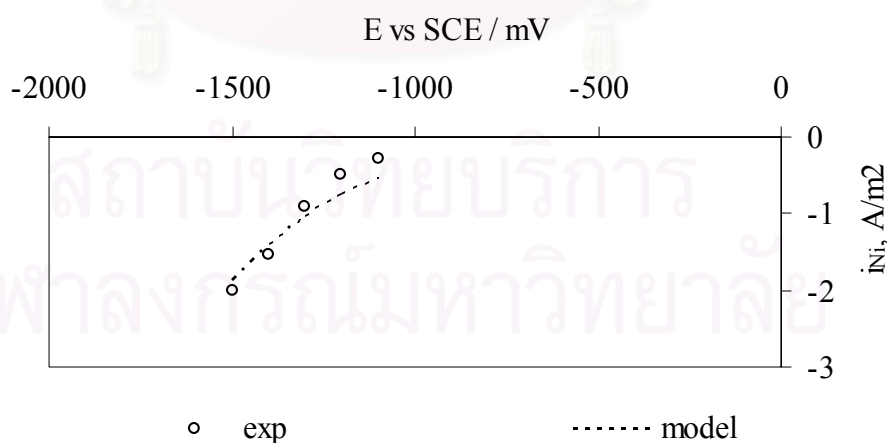


Figure 3.20 Partial current density of nickel in alloy simulation and experimental data obtained by Trial & Error method for the kinetic constant of Zn_Ni and Ni_Zn;
 C_{Ni} and $C_{Zn} = 0.05$ M, $7.26 \text{ cm}^3 \text{ s}^{-1}$, pH of 4

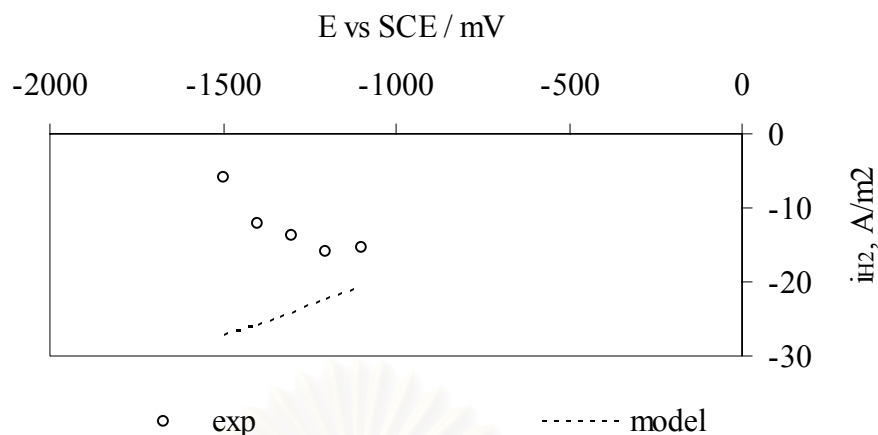


Figure 3.21 Partial current density of hydrogen in alloy simulation and experimental data obtained by Trial & Error method for the kinetic constant of Zn_{Ni} and Ni_{Zn}; C_{Ni} and $C_{Zn} = 0.05$ M, $7.26 \text{ cm}^3 \text{ s}^{-1}$, pH of 4

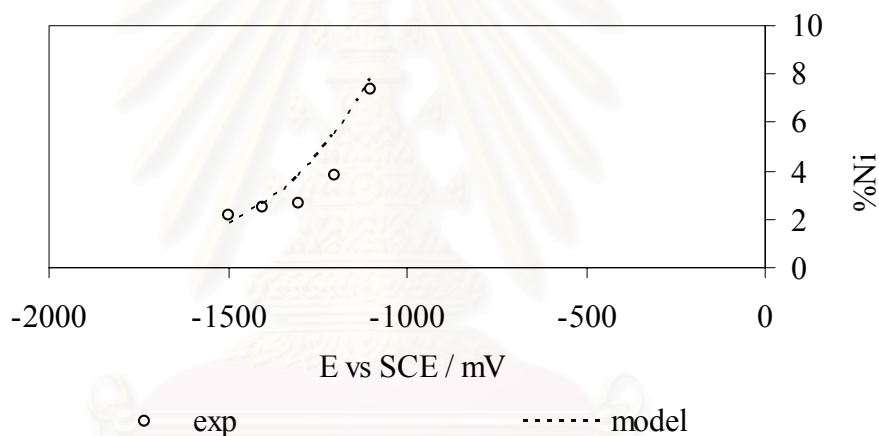


Figure 3.22 Percentage of nickel in alloy simulation and experimental data obtained by Trial & Error method for the kinetic constant of Zn_{Ni} and Ni_{Zn}; C_{Ni} and $C_{Zn} = 0.05$ M, $7.26 \text{ cm}^3 \text{ s}^{-1}$, pH of 4

Figure 3.21 presents the hydrogen evolution in alloy deposition. The model results and experimental results are significantly different. The hydrogen evolutions, obtained by the experiments, are not reasonable. This is because the problem of the partial current of hydrogen evolution, which is analysed by different kinds of equipment, atomic absorption spectroscopy and the potentiostat. On the other hand, the simulation of nickel, zinc and the percentage of nickel results predicts well with the experimental data under the role of substrate.

3.1.5.1c Model Validation by Testing the Influence of Bath Concentration

In this part, the model is validated with changing bath concentration of nickel and zinc. The simulation using the estimated kinetic constant obtained by Trial & Error method is thus run for the different bath concentrations.

Comparison of experimental and simulated partial currents for Zn-Ni alloy at different bulk concentrations is shown in Figure 3.23 and 3.24 respectively. The influence of the concentration of the codeposition element on the extent of inhibition and enhancement in Zn-Ni alloy is observed with previous works⁴⁷. The result of Figure 3.23 shows that the predicted inhibition of nickel increases with increasing zinc concentration in solution. On the other hand, figure 3.24 demonstrates the catalytic effect of nickel on zinc, depending upon increasing nickel concentration.

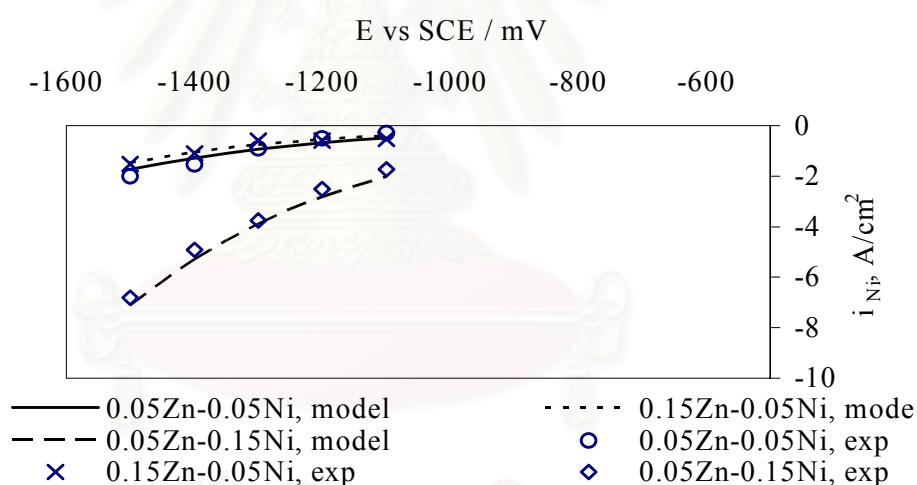


Figure 3.23 Predicted influence of coelement concentration on nickel partial current during Zn-Ni codeposition, $0.76 \text{ cm}^3 \text{ s}^{-1}$, pH of 4

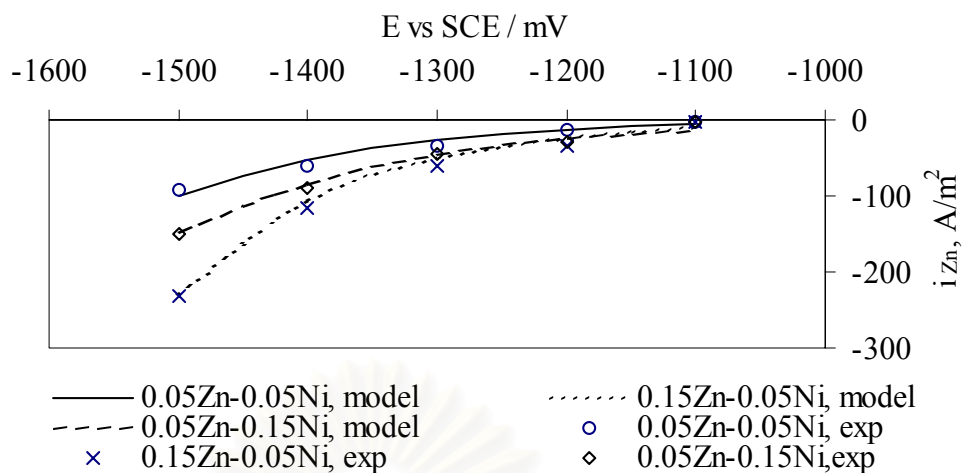


Figure 3.24 Predicted influence of coelement concentration on zinc partial current during ZnNi codeposition, $0.76 \text{ cm}^3 \text{ s}^{-1}$, pH of 4

The influence of metal ion concentration can be explained clearly by Table 3.11.

Table 3.11 Ratio of partial current alloy at different metal concentration at $-1.4 \text{ V } E_{\text{app}}$

Partial current	0.15 Zn, 0.05 Ni	0.05 Zn, 0.15 Ni
	0.05 Zn, 0.05 Ni	0.05 Zn, 0.05 Ni
$i_{11}+i_{12}$ (Ni_Ni)	0.358	5.69
$i_{21}+i_{22}$ (Ni_Zn)	0.704	1.94
$i_{41}+i_{42}$ (Zn_Zn)	3.06	0.869
$i_{51}+i_{52}$ (Zn_Ni)	1.3	2.2

Table 3.11 shows the ratio of partial current when increasing zinc and nickel bulk concentration in the electrolyte by three times. Increasing zinc concentration considering at high deposition (-1.4 V) results in higher content of zinc deposition on zinc substrate than deposition of zinc on nickel substrate, clearly seen from 3.06 times and 1.3 times higher of $i_{41}+i_{42}$ and $i_{51}+i_{52}$ respectively. On the other hand, nickel is inhibited by increasing of surface blocking effect, $\text{Zn(I)}_{\text{ads}}$, and higher strong effect on the deposition of nickel on nickel substrate. The increasing of zinc concentration

therefore has a strong effect on enhancing rate of zinc deposition on zinc substrate and inhibiting rate of nickel on nickel substrate.

Increasing nickel concentration results in higher content of nickel deposition on nickel substrate than deposition of nickel on zinc substrate, clearly seen from 5.69 times and 1.94 times higher of $i_{11}+i_{12}$ and $i_{21}+i_{22}$ respectively. The result shows the higher rate of zinc deposition that is able to deposit on nickel substrate as seen from 2.2 times higher of $i_{51}+i_{52}$. On the other hand, zinc is inhibited by increasing of surface blocking effect, $Ni(I)_{ads}$, but only the deposition of zinc on zinc substrate. Increasing of nickel concentration therefore has a strong effect on enhancing rate of zinc deposition on nickel substrate, nickel on nickel substrate and inhibiting rate of zinc on zinc substrate.

3.1.6 Discussion

The present theoretical model gives a satisfactory description of observed experimental results for different metal concentration of zinc and nickel. This indicates that the basic physical assumptions underlying the model are reasonable. According to the present model, the inhibition of the more noble metal, nickel, is due to a surface blocking effect of adsorbed species similar to that described by Matloz. The enhancement of the deposition rate of the less noble metal, zinc, is attributed to the catalyzing of zinc deposition current by nickel nuclei and the fresh nickel nuclei that is the substrate related through Eq. 5a. The theoretical predictions depend critically on the value of the kinetic contents, because the essential features of the model lie on the kinetic expressions and adsorption effects at the surface. The kinetic parameters for all reaction pathways can be obtained from single metal kinetics. The model can therefore be used for the quantitative prediction of the effect of electrolyte concentration on the resulting alloy composition. In addition, this model taking into account the overpotential for determining the partial current by the Tafel equation. The equilibrium potential depends on the substrate, which metal ions deposit on. The equilibrium potentials of nickel, depositing on both nickel substrate and zinc substrate, are -0.53 V. Conversely, the equilibrium potentials of zinc, depositing on zinc substrate and nickel substrate, are different, as indicated -1.05 V and -0.07 V

respectively. The overpotentials in each partial current, in relation to substrate effect, give more correct calculation of simulated partial currents.

3.1.7 Conclusion

The model entails a mathematical framework for the description of the codeposition of Zn-Ni alloy lying on substrate effect for different electrolyte concentration and applied potentials. The inhibition effect observed in nickel deposition is attributed to the partial surface blocking by the adsorbed intermediates, and the enhancing effect of zinc deposition is attributed to the catalyzing of zinc deposition current by nickel nuclei. The model is able to simulate the influence of potential, electrolyte concentration, and diffusion mass transport on the partial currents and the resulting alloy codeposition.

Although it is found that the substrate model predicts well with the experimental data. According to the experimental results of Zn-Ni alloy in chapter 2, the mechanism model can be proposed in the role of mixed species effect. In the next chapter, modelling the Zn-Ni mechanism under the role of mixed species will be performed, as proposed by N. Zech. In this part, the model is modified in order to predict the deposit content in the quantitative way.

3.2 Mixed Species Model

3.2.1 Introduction

In the first section of this chapter, the effect of substrate has been considered for the modelling. As previously said, although the results of this model fit well with the experimental evolution, there is no conclusive evidence that the nickel nuclei are responsible for the enhancement of zinc deposition rate. Consequently, examining and improving models with mixed species are taken into account. The experiment went onto the modelling of Zn-Ni alloy, regarding the mixed species proposed by Wiart⁶⁰ and later by Zech⁵⁹. The partial currents of nickel, zinc and hydrogen are calculated as a function of different bath concentrations. The partial currents determine the alloy composition and current efficiency, which are compared to the experimental results.

3.2.2 Model Assumption

According to the experimental results in chapter 2, enhancing of zinc alloy deposition and inhibiting of nickel alloy deposition, comparing with the elemental deposition, are possible due to Zn-Ni mixed species. In this chapter, the mathematical model describing the codeposition behaviour of nickel and zinc is therefore presented. The model is essentially based on two general principles, as the following:

- (1) Interfacial kinetics of the adsorbed species of nickel, zinc, Zn-Ni mixed species, and hydrogen evolution on Zn-Ni substrate. In addition, the adsorbed species can form at the electrode surface.
- (2) Mass transport assuming a Nernst diffusion layer.

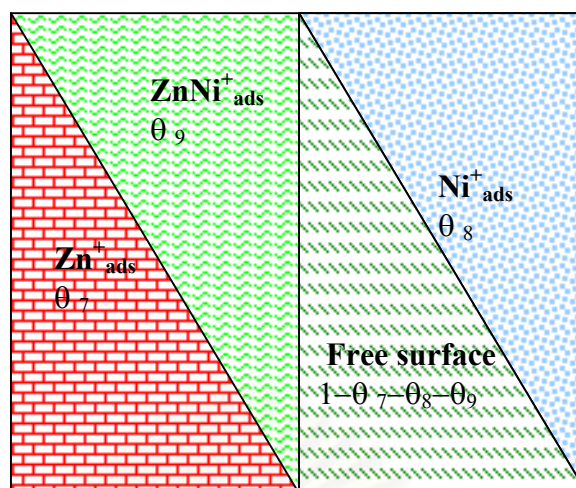


Figure 3.25 Diagram of Zn-Ni alloy codeposition

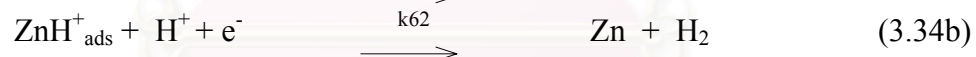
Figure 3.25 shows the diagram representing the effect of substrate on Zn-Ni alloy codeposition. The electrode surface is divided into four parts, the surface fractions θ_7 , θ_8 and θ_9 of the adsorbed species Ni^+_{ads} , Zn^+_{ads} , and $ZnNi^+_{ads}$ respectively and the free surface fraction, $1 - \theta_7 - \theta_8 - \theta_9$.

3.2.3 Theoretical Model

3.2.3.1 General Mechanism of the Electrode Reaction

A reaction path has been developed by the basis of the assumption that both single metals of zinc and nickel are reduced in two consecutive steps, as described by Matloz⁵⁵. Nickel ion can deposit on a substrate according to reaction 3.30. As well as the deposition of zinc ion is seen in reaction 3.31. The mixed species of $ZnNi(III)_{ads}$ leading to enhancement of zinc and reducing nickel adsorption is assumed to take place according to reaction 3.32. In addition, reduction of protons and water molecules may occur as a side reaction and for this reason they are also included in the model as seen in reaction 3.33 and 3.34

The model is assumed to be under steady-state conditions. Concentration variations are restricted to a thin boundary layer near the electrode surface. Mass transport across this layer is governed by diffusion. Migration effects are considered to be negligible. The following reduction reactions are assumed to take place.



Ni(II) and Zn(II) dissolved metal ion, hydrolyzed or not, Ni^+_{ads} and Zn^+_{ads} are monovalent adsorbed reaction intermediate which may or may not contain a hydroxyl group. Ni and Zn are respectively nickel deposited metal and zinc deposited metal. $[\text{ZnNi(III)}]_{\text{ads}}$ is the mixed species adsorbed reaction intermediate.

3.2.3.2 Mass Transfer Effect

The model is assumed to be under steady-state conditions. Concentration variations are restricted to a thin boundary layer near the electrode surface. Mass transport across this layer is governed by diffusion. Migration effects are considered to be negligible.

The steady-state material balances within the diffusion layer for species Ni(II), Zn(II) and H⁺, 0<x<d, can be written in order to investigate the concentration in the diffusion layer.

$$\nabla \cdot N_{\text{Ni(II)}} = 0 \quad (3.35)$$

$$\nabla \cdot N_{\text{Zn(II)}} = 0 \quad (3.36)$$

$$\nabla \cdot N_{\text{H}^+} = 0 \quad (3.37)$$

$$K_w = C_{\text{OH}^-} \cdot C_{\text{H}^+} \quad (3.38)$$

Assuming a constant diffusion coefficient, D, the flux of each species *i*, in the diffusion layer is $N_i = -D \, dC_i / dx$. The assumed values of the diffusion coefficients are $4 \times 10^{-10} \text{ m}^2 \text{ s}^{-1}$ for Ni(II), $5.09 \times 10^{-10} \text{ m}^2 \text{ s}^{-1}$ for Zn(II), and $9.3 \times 10^{-9} \text{ m}^2 \text{ s}^{-1}$ for solvated protons³⁵.

The intermediate species, Ni(I)_{ads}, NiH(I)_{ads}, ZnNi(III)_{ads}, Zn(I)_{ads} and ZnH(I)_{ads}, exist only at the electrode surface so their concentrations are equal to zero in the solution. At the electrode surface (x = 0), the partial current densities are related to the species fluxes by the following reactions:

$$N_{\text{Ni(II)}} - \frac{i_{71}}{F} - \frac{i_{91}}{F} - \frac{i_{92}}{F} = 0 \quad (3.39)$$

$$N_{\text{Zn(II)}} - \frac{i_{81}}{F} - \frac{i_{91}}{F} = 0 \quad (3.40)$$

$$N_{\text{H}^+} - \frac{i_{31}}{F} - \frac{i_{32}}{F} - \frac{i_{61}}{F} - \frac{i_{62}}{F} = 0 \quad (3.41)$$

At the edge of the Nernst diffusion layer, x = δ, all concentrations are equal to the bulk concentrations values

$$C_{\text{Ni(II)}}|_{x=\delta} = C_{\text{Ni(II)}}^b \quad (3.42)$$

$$C_{\text{Zn(II)}}|_{x=\delta} = C_{\text{Zn(II)}}^b \quad (3.43)$$

The diffusion layer, δ_N is assumed to change for all the species according to their diffusion coefficients.

$$\delta_N = \delta_p \left[\frac{D}{\nu} \right]^{1/3}$$

δ_N was determined by the experimental data of $\text{Fe}(\text{CN})_6^{3-}$ and $\text{Fe}(\text{CN})_6^{4-}$ in solution with the same device of those used in Zn-Ni alloy experiment. The diffusion equation is first discretized and iteratively solved, the calculation is stopped when the relative variation between two consecutive iterations is lower than 1×10^{-5} .

3.2.3.3 Electrochemical Kinetic

Charge transfer kinetics is assumed to obey the Butler-Volmer equation. Far from equilibrium the anodic reaction can be neglected and, therefore, a modified Tafel expression describes the electrochemical reaction rate at the surface and is used to calculate the partial current.

As an example, in the case of nickel deposits on nickel substrate of the first step, the partial current densities, i_{71} , can thus be expressed as $i_{71} = -F k_{71}^0 C_{\text{Ni}^{2+}} \theta_{\text{Ni}} (1-\theta_7-\theta_8-\theta_9) \exp(-b_{71}\eta_{71})$. The corresponding electrochemical rate expressions are summarized in Table 3.12. At steady state, the material balances for the intermediate species yield to equations 3.44 – 3.46. In addition, all the step coverage is constant, so the first and second step of the reaction gave the same rate.

Table 3.12 Electrochemical rate expressions for Zn and Ni alloy simulation

Tafel rate equation	Reaction
$i_{71} = -F k_{71}^0 C_{Ni}^{2+} (1-\theta_7-\theta_8-\theta_9) \exp(-b_{71}\eta_{71})$	3.30a
$i_{72} = -F k_{72}^0 \theta_8 \exp(-b_{72}\eta_{72})$	3.30b
$i_{81} = -F k_{81}^0 C_{Zn}^{2+} (1-\theta_7-\theta_8-\theta_9) \exp(-b_{81}\eta_{81})$	3.31a
$i_{82} = -F k_{82}^0 \theta_7 \exp(-b_{82}\eta_{82})$	3.31b
$i_{91} = -F k_{91}^0 C_{Ni}^{2+} C_{Zn}^{2+} (1-\theta_7-\theta_8-\theta_9)^2 \exp(-b_{91}\eta_{91})$	3.32a
$i_{92} = -F k_{92}^0 \theta_9 \exp(-b_{92}\eta_{92})$	3.32b
$i_{31} = -F k_{31}^0 C_H^+ \theta_{Ni} (1-\theta_1-\theta_2-\theta_3) \exp(-b_{31}\eta_{31})$	3.33a
$i_{32} = -F k_{32}^0 C_H^+ \theta_{Ni} \theta_2 \exp(-b_{32}\eta_{32})$	3.33b
$i_{61} = -F k_{61}^0 C_H^+ \theta_{Zn} (1-\theta_4-\theta_5-\theta_6) \exp(-b_{61}\eta_{61})$	3.34a
$i_{62} = -F k_{62}^0 C_H^+ \theta_{Zn} \theta_5 \exp(-b_{62}\eta_{62})$	3.34b

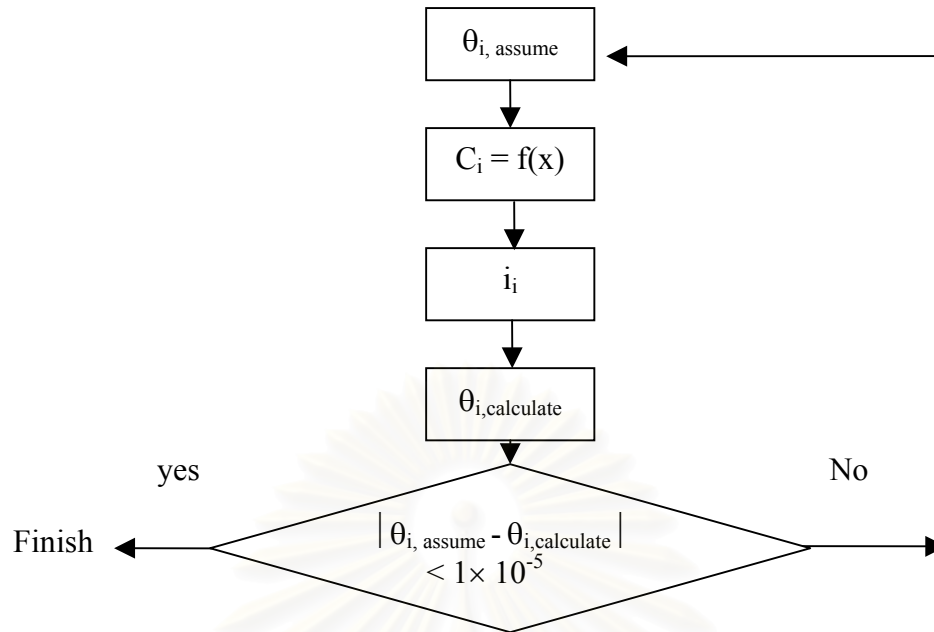
Due to its larger molecular size, the mixed species intermediate was assumed to occupy the space of two surface sites, Therefore the current density in Eq 3.32a varies with the square of the free surface (Table 3.12).

$$\frac{d\theta_7}{dt} = \frac{i_{71}}{F} - \frac{i_{72}}{F} = 0 \quad (3.44)$$

$$\frac{d\theta_8}{dt} = \frac{i_{81}}{F} - \frac{i_{82}}{F} = 0 \quad (3.44)$$

$$\frac{d\theta_9}{dt} = \frac{i_{91}}{F} - \frac{i_{92}}{F} = 0 \quad (3.46)$$

There are seven unknowns in this system, $C_{Ni(II)}$, $C_{Zn(II)}$, C_H^+ , C_{OH^-} , θ_7 , θ_8 and θ_9 , system of Eq. 3.35 – 3.46 is solved. As the organigram given below, the different kinetic parameters are further determined by fitting the experimental data during elemental deposition.



After the simulation is completed the partial current densities for each metal and the side reaction are determined from Eq. 3.48 – 3.52

$$i_{Ni} = i_{71} + i_{72} \quad (3.48)$$

$$i_{Zn} = i_{81} + i_{82} + i_{91} + i_{92} \quad (3.49)$$

$$i_{side} = i_{10} + i_{11} \quad (3.50)$$

$$i_{total} = i_{Ni} + i_{Zn} \quad (3.51)$$

$$\eta = (i_{Ni} + i_{Zn}) / (i_{Ni} + i_{Zn} + i_{H2}) \quad (3.52)$$

The Tafel constants for single metal deposition of Ni and Zn were determined experimentally from a plot of the logarithm of current density vs. potential. It was assumed that the Tafel slopes for the two consecutive one-electron steps were the same. The rate constants, k_{71}^0 , k_{81}^0 , k_{72}^0 , k_{82}^0 were obtained by fitting the simulation to the experimental data for single metal deposition. These rate constants are the same that those use in the substrate model. The consecutive reaction model yields such a dependence only when adsorption is low, meaning that the first reaction step is rate

limiting. Therefore, in the model calculations it was assumed that the second reaction step (Eq. 7b and 8b) is fast compared to the first step (Eq. 7a and 8a). The rate constants determined for single metal deposition were used for the simulation of alloy deposition. The value of constants, k_{91}^0 , k_{92}^0 were assumed to fit well with the experimental results of the alloy data by Trial & Error method.

Table 3.13 List of the kinetic parameters

Reaction constants			Inverse Tafel slope, V^{-1}		Reactions	
k_{71}	=	$9.89 \times 10^{-7} \text{ cm s}^{-1}$	b_{71}	=	6.05	3.30a
k_{72}	=	$7.51 \times 10^2 \text{ mol cm}^{-2} \text{ s}^{-1}$	b_{72}	=	6.05	3.30b
k_{81}	=	$7.51 \times 10^{-6} \text{ cm s}^{-1}$	b_{81}	=	10	3.31a
k_{82}	=	$7.51 \times 10^3 \text{ mol cm}^{-2} \text{ s}^{-1}$	b_{82}	=	10	3.31b
k_{91}	=	$3.00 \times 10^2 \text{ cm s}^{-1}$	b_{41}	=	6	3.32a
k_{92}	=	$3.00 \times 10^{-9} \text{ mol cm}^{-2} \text{ s}^{-1}$	b_{43}	=	6	3.32b
k_{31}	=	$3.00 \times 10^{-3} \text{ cm s}^{-1}$	b_{31}	=	3.8	3.33a
k_{32}	=	$3.00 \times 10^6 \text{ mol cm}^{-2} \text{ s}^{-1}$	b_{32}	=	3.8	3.33b
k_{61}	=	$3.00 \times 10^{-2} \text{ cm s}^{-1}$	b_{61}	=	1.5	3.34a
k_{62}	=	$3.00 \times 10^7 \text{ mol cm}^{-2} \text{ s}^{-1}$	b_{62}	=	1.5	3.34b

3.2.4 Results of the Global Model

3.2.4.1 Comparison between Experimental Results and Theoretical Results

Figure 3.26, 3.27, 3.28 compare the model simulation to the experimental results for the ZnNi system at $7.26 \text{ cm}^3 \text{ s}^{-1}$ and $\text{pH} = 4$ for nickel, zinc and hydrogen respectively. The nickel and zinc concentrations are 0.05 M. From these figures, it appears that the partial currents of zinc and nickel fit well the experimental results. On the other hand, the partial currents of hydrogen evolution significantly differ from those coming from experiments. The experiment of hydrogen evolution is not reasonable, and this species is not the objective for modelling. The modelling of hydrogen evolution will improve in the perspective work. The simulation partial

current densities of zinc is less than the experimental observation, while the simulation partial current densities of nickel and hydrogen are higher than the experimental results.

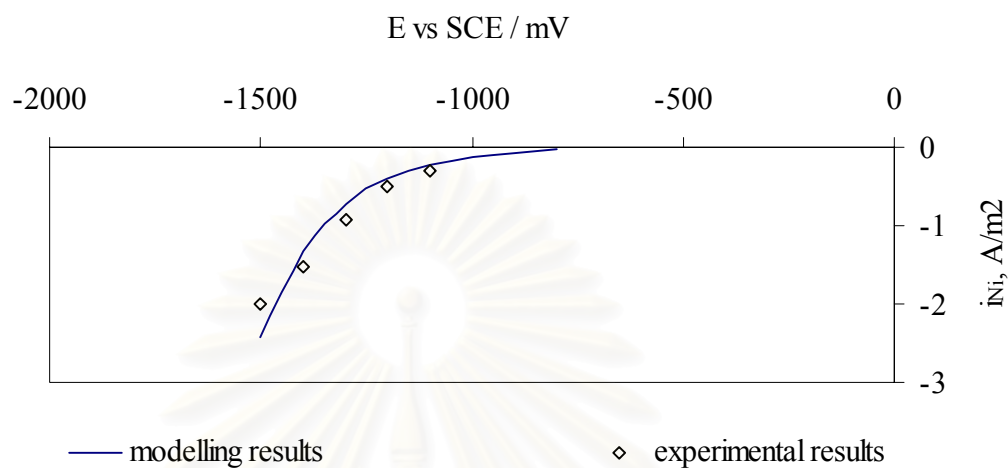


Figure 3.26 Nickel partial current density in alloy simulation and experimental data; C_{Ni} and $C_{Zn} = 0.05$ M, 7.26 cm³ s⁻¹, pH of 4

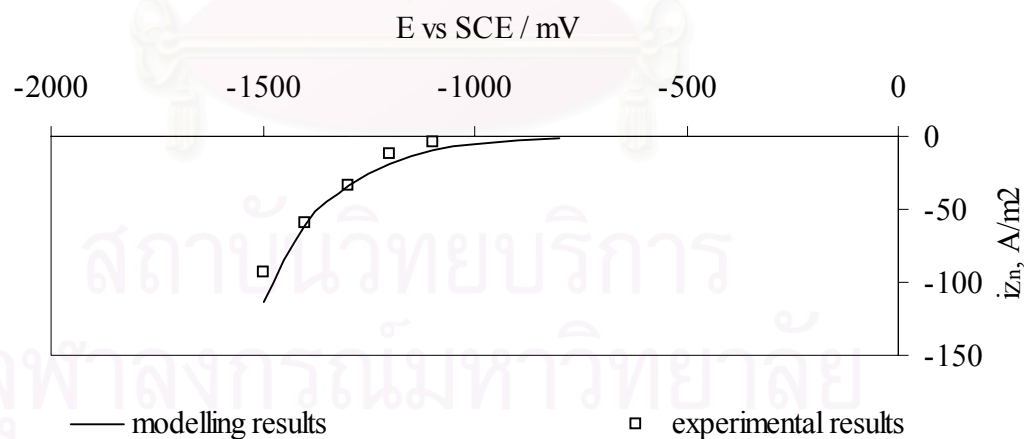


Figure 3.27 Zinc partial current density in alloy simulation and experimental data; C_{Ni} and $C_{Zn} = 0.05$ M, 7.26 cm³ s⁻¹, pH of 4

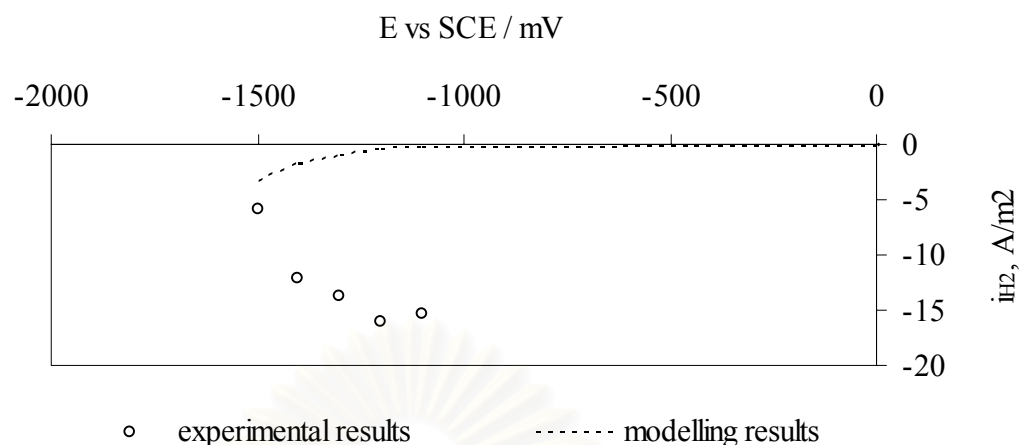


Figure 3.28 Hydrogen evolution partial current density in alloy simulation and experimental data; C_{Ni} and $C_{\text{Zn}} = 0.05 \text{ M}$, $7.26 \text{ cm}^3 \text{ s}^{-1}$, pH of 4

3.2.4.2 Model Validation

Changing bath concentrations is to validate the model. The simulation using the estimated kinetic constant of the mixed species obtained by Trial & Error method is thus tested under the different bath concentration.

Figures 3.29 and 3.30 show the comparison of partial currents between the simulation results and the experimental results, for nickel and zinc respectively, in terms of Zn-Ni alloy deposition at different bulk concentrations. The experimental results can be represented by the modeling results. Increasing zinc concentration leads to increasing of partial current of zinc and inhibit partial current of nickel. In addition, increasing nickel concentration leads to increasing nickel partial current and enhance zinc partial current.

The enhancement of the deposition rate of the less noble metal, Zn, is due to the formation of the adsorbed metal intermediate through Eq 9a, similarly as proposed by Wiart⁶⁰ and Zech⁵⁹ for Zn-Ni deposition and iron metal anomalous deposition respectively. The results of this study show that the proposed model describes adequately the main features of the experimentally observed codeposition behavior of

iron group metals, including both the inhibition and the enhancement of partial reaction rates due to the codepositing species.

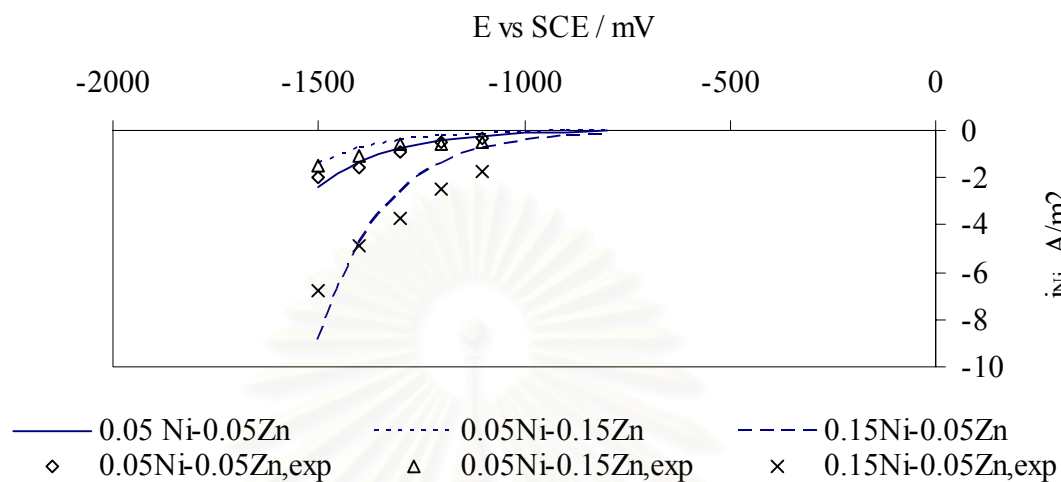


Figure 3.29 Predicted influence of coelement concentration on nickel partial current during ZnNi codeposition, $0.76 \text{ cm}^3 \text{ s}^{-1}$, pH of 4

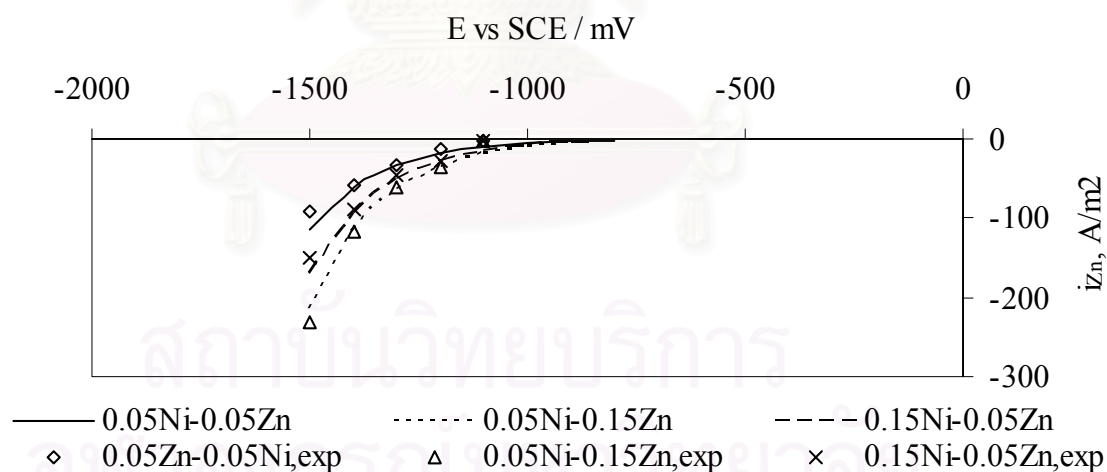


Figure 3.30 Predicted influence of coelement concentration on zinc partial current during ZnNi codeposition, $0.76 \text{ cm}^3 \text{ s}^{-1}$, pH of 4

3.2.5 Discussion

The present theoretical model gives a satisfactory description of observed experimental results for different metal concentration of zinc and nickel. This indicates that the basic physical assumptions underlying the model are reasonable. According to the present model, the inhibition of the more noble metal, nickel, is due to a surface blocking effect of adsorbed species similar to that described by Matloz. The enhancement of the deposition rate of the less noble metal, zinc, is attributed to the mixed species through Eq. 9a. It is found that this model could use for the quantitative prediction, comparing to the model of Zech⁵⁹ which has the disadvantage of quantitative prediction when changing the bath concentration. The different Tafel parameters in each partial current, relating to thermodynamic effects of each species, result in better quantitative prediction than Zech model.

3.2.6 Conclusion

The model provides a mathematical framework for the description of the codeposition of Zn-Ni alloy lying on solution effect for different electrolyte concentration and applied potentials. The inhibition effect observed in nickel deposition is attributed to the partial surface blocking by the adsorbed intermediates, and the enhancing effect of zinc deposition is attributed to the mixed species. The model is able to simulate the influence of potential, electrolyte concentration, and diffusion mass transport on the partial currents, resulting in predicting quantitative ratios of alloy codeposition.

The two models, the substrate effects and the mixed species effects, can describe electrode surface phenomenon. However, there is a difference between these two models, the substrate effect is assumed to be modified adsorption kinetic and the mixed species effect is adsorbed at the electrode. Both models predict an enhancement of zinc deposition and an inhibition of nickel deposition.

In addition, the substrate effect model is developed from the Matloz's model, thereby generating the enhancing effect of the less noble metal. The mixed species effect model is developed from the N. Zech's model in order to predict the alloy content in the quantitative way.

3.3 Effect of Complexing Agent on Zn-Ni Alloy Deposition

3.3.1 Introduction

According to chapter 2 of the third part of this thesis, the experimental investigation and mathematical modeling of Zn-Ni alloy electrodeposition have been carried out. In this part, the complexing agent imposing on the Zn-Ni alloy mechanism is focused. Consequently, the electrodeposition of Zn-Ni alloy from potassium chloride bath under potentiostatic mode was studied in order to enhance knowledge of this process and to establish a mathematical model of complexing agent effect on Zn-Ni alloy deposition.

Comprehensive studies have been carried out on such electrodepositions from different baths, including cyanide¹, sulfate²⁻³ and chloride baths⁴⁻⁶. In recent years, there has been a preference for chloride-based solutions since it is probably easier to obtain NiCl precipitation of 10%-15%, nickel-containing layers. Some of these chloride electrolytes also contain other species acting as a buffer and / or complexing agent, such as boric acid³⁸⁻⁴⁰, acetic acid^{44, 45} or ammonium chloride^{41, 46}. Now, the alkaline bath developed by Muller is preferred and mainly used for corrosion protection.

From the assumption of the anomalous behavior is attributed to the formation of a zinc hydroxide film on the electrode surface, which suppresses the discharge of nickel ions. The zinc hydroxide formation arises from the local increase in pH due to the hydrogen reduction. Presence of NH₄Cl in the chloride bath therefore prevents the precipitation of zinc hydroxide and increases the reduction of nickel, and then increases the nickel content in the deposit. This suggests the formation of ammonium complexes, such as [Zn(NH₃)₄]²⁺ and [Ni(NH₃)₆]²⁺ which prevent hydroxide precipitation⁴⁷.

The other assumption of chloride bath is the adsorption of chloride ion, Cl⁻ and the chloride complex. Zinc can be complex by chloride such as [ZnCl⁺], [ZnCl₂], [ZnCl₃⁻] and [ZnCl₄²⁻], while nickel is not complex by chloride ion. This chloride

complexing behavior of zinc is also able to increase more nickel depositing on the electrode surface⁴⁸.

The objective of this work is to model Zn-Ni alloy deposition, which takes into account the role of complexing effect of chloride ion comparing with the experiment of KCl bath. The salt, KCl has been used in Zn-Ni deposition and investigated how it can affect the system. Consequently, this study is the previous proposal dealing with how the salt involves in the complexing effect.

3.3.2 Experiment

Experiments are carried out with an EQCM. The alloy content is determined by atomic adsorption spectroscopy. The electroplating solution contained 0.05 mole dm^{-3} ZnCl_2 , 0.05 mole dm^{-3} , $\text{NiCl}_2 \cdot 6\text{H}_2\text{O}$ for the bath with no complexing agent effect. In order to study the effect of complexing agent, KCl 1 and 2 mole dm^{-3} is added to the electrolyte. The pH of the electrolyte is kept constantly at pH 4.

The alloys are obtained at 25 °C by depositing the metals potentiostatically onto the crystal quartz gold electrode with a diameter of 1.37 cm^2 . The electrolyte flow rate is 0.76 $\text{cm}^3 \text{s}^{-1}$. The reference electrode is the saturated calomel electrode, and a platinum mesh is used as a counter electrode.

3.3.3 Results and Discussions

Figure 3.31 shows the current – time dependence for the deposition of Zn-Ni alloy comparing with and without KCl complexing agent at -1.4 V of applied potential. The increase of total current resulted only from adding KCl,

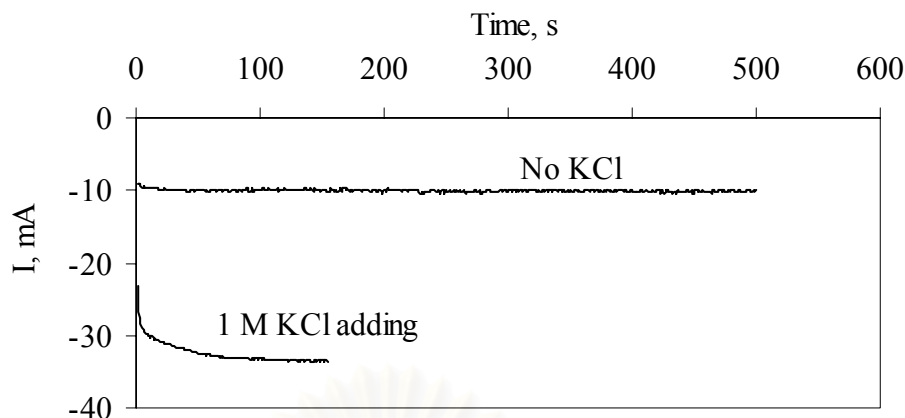


Figure 3.31 Effect of KCl complexing agent on the Chronoamperogram of Zn-Ni alloy deposition at -1.4 V/SCE

From Table 3.14, it appears that all partial currents of zinc, nickel and hydrogen evolution increase about 3 times. According to Table 3.14 and 3.15, which show the partial currents observed in potentiostatic and galvanostatic mode respectively, the complexing effect is observed in both cases. Presumably, decreasing of zinc contents was resulted from the formation of zinc and the complexing agent.

Increasing partial currents, in KCl bath under potentiostatic, results in facing difficulty of mathematical model development. According to the Butler-Volmer equation, the partial current depends on the kinetic parameters of single metal deposition in each applied potential under potentiostatic mode. One or more of these parameters is affected by the adjunction of the salt.

Table 3.14 Partial current of alloy obtained at -1.4 V for various operating conditions

Zn-Ni alloy Electrolytic bath	I_{Zn} , A	I_{Ni} , A	I_{tot} , A	I_{H_2} , A	current efficiency	% Ni _{dep}	% Zn _{dep}	time, s
No complexing agent	0.0082	0.0002	0.0100	0.0017	83.46	2.51	97.49	500
KCl	0.0276	0.0017	0.0343	0.0050	85.45	5.83	94.17	835
KSO ₄	0.0262	0.0039	0.0348	0.0047	86.41	12.92	87.08	502
NaSO ₄	0.0296	0.0020	0.0337	0.0021	93.78	6.26	93.74	667

Table 3.15 Partial current of alloy obtained at -0.01 A and various operating conditions

Zn-Ni alloy Electrolytic bath	I_{Zn}, A	I_{Ni}, A	I_{tot}, A	I_{H_2}, A	current efficiency	% Ni _{dep}	% Zn _{dep}	time, s
No complexing agent	0.0082	0.0002	0.0100	0.0017	83.46	2.51	97.49	500
KCl	0.0082	0.0004	0.0100	0.0014	85.68	4.14	95.86	500

In order to understand clearly the reason of increasing partial current in each applied potential under potentiostatic mode, some assumptions are omitted and the salt effect is considered.

3.3.4 Ionic Strength Effect

According to the effect of salt species that increases the total current, the ionic strength is considered. The ionic strength as well as the type of supporting electrolyte can have an important influence on the rate of reaction⁶²⁻⁶⁶. Martin and Hill⁶³ measured the effect of ionic strength on the rate of manganese and iron catalyzed oxidation of S(IV) and found that the rate constant is very sensitive to the ionic strength. In order to test the influence of ionic strength to the system of salt species effect, the rate constant can be written as a function of the ionic strength in the form of an extended Debye-Hückel equation:

$$\log \tilde{\alpha}_i = -0.5Z_i^2 \frac{I^{1/2}}{1 + I^{1/2}} \quad 3.53$$

A simpler form due to Guntelberg⁶⁷ (Robinson and Stokes, 1959), which gives a fair representation of the behavior of a number of electrolytes up to $I = 0.1 \text{ mole}^{-1}$.

$$\log(k_1/k_0) = A' \sqrt{I_1} / (1 + \sqrt{I_1}) \quad 3.54$$

where k_1 is the rate constant at ionic strength I , k_0 is the rate constant at infinite dilution and A' is a constant (function of the absolute temperature, of the dielectric constant, and of the charge of the ionic reactants).

The ionic strength of the solution is defined the concentration C_i and the different charge of ionic species in solution as in Eq 3.55. We can also define the activity coefficient as in Eq. 3.56:

$$I = 0.5 \sum (z_i^2 c_i) \quad 3.55$$

$$\log \gamma_i = -0.51 z_i^2 \sqrt{I} \quad 3.56$$

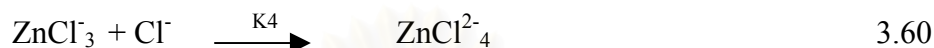
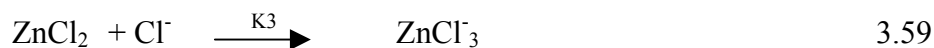
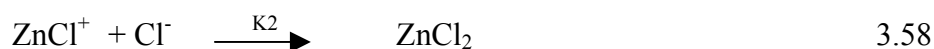
All ions present charge, z_i , and concentration, c_i and the activity coefficient, γ_i .

In order to determine the effect of ionic strength, the electrolytic bath of Zn-Ni electrolyte with and without KCl are performed. Under consideration of zinc and nickel percentage, as shown in Table 3.14, the complexing effect observation in zinc is demonstrated, but not for nickel, agreeing with literature data mentioned. This can explain a decrease in zinc concentration when forming a complex with chloride ion. On the other hand, increasing of nickel can be explained by the ionic strength effect of the salt species. Increasing potassium chloride concentration in the bath, also increases complexing effect on zinc and the ionic strength effect on nickel and zinc.

In nickel, there is no balance between the salt effect and the complexing effect, so that increasing of nickel partial current is found, due to the ionic strength effect. On the other hand, there is a balance in the zinc case so that less zinc partial current is found, due to the complexing effect.

In summary, the complexing effect and the ionic strength effect of the salt species totally result from KCl complexing agent.

For the complexing effect, the different form of zinc can be complex by chloride ion according to the following equation.



K_i is the equilibrium constant of complex Zn-Cl in Zn-Ni electrolyte.

Table 3.16 Concentration of the equilibrium constant (K_i) of complex Zn-Cl in Zn-Ni electrolyte with and without potassium chloride

Equilibrium constant	With KCl	Without KCl
K_1	1.04	1.38
K_2	1.25	1.55
K_3	0.5	0.3
K_4	1.13	1.03

According to equation 3.57 to 3.60, and the value of the equilibrium constant (Table 3.16), the concentration of zinc is determined in different bath concentrations, as shown in Table 3.17. In addition, it is found that increasing KCl concentration leads to decreasing zinc ion concentration in the electrolyte, resulting in occurring less zinc deposition on the electrode. The content of zinc in bath 3 which is the highest KCl concentration, (Table 3.18) is therefore lower comparing to bath 2 and 1.

Table 3.17 Calculated parameter in each bath condition according to equation 4.2 and 4.3, and the Butler-Volmer equation

Electrolytic bath	$C_{Ni^{2+}}$ (M)	$C_{Zn^{2+}}$ (M)	C_{Cl^-} (M)	I (M)	$k_{Ni^{2+}}$ ($cm\ s^{-1}$)	$k_{Zn^{2+}}$ ($cm\ s^{-1}$)	$I_{Ni^{2+}}$ A	$I_{Zn^{2+}}$ A	I_{tot} A
bath 1*	0.05	0.04	0.195	0.3	1.70E-07	4.66E-05	0.0002	0.0082	0.0125
bath 2**	0.05	0.007	1.115	1.3	1.45E-05	8.96E-04	0.0017	0.0276	0.0343
bath 3***	0.05	0.001	2.090	2.3	2.59E-05	1.32E-03	0.0304	0.0084	0.0625

A' of zinc = 2.41

A' of nickel = 3.62

* bath 1 : 0.05 M NiCl₂ 6H₂O, 0.05 M ZnCl₂

** bath 2 : 0.05 M NiCl₂ 6H₂O, 0.05 M ZnCl₂ + 1M KCl

*** bath 3 : 0.05 M NiCl₂ 6H₂O, 0.05 M ZnCl₂ + 2M KCl

Table 3.18 The percentage of nickel and zinc deposition obtained in different bath concentrations

Electrolytic bath	%Zn	%Ni
Bath1: 0.05 M NiCl ₂ 6H ₂ O, 0.05 M ZnCl ₂	97.62	2.38
Bath 2: 0.05 M NiCl ₂ 6H ₂ O, 0.05 M ZnCl ₂ + 1M KCl	94.20	5.80
Bath 3: 0.05 M NiCl ₂ 6H ₂ O, 0.05 M ZnCl ₂ + 2M KCl	21.68	78.32

Table 3.17 presents the calculated parameters from Debye-Hückel equation and the Butler-Volmer equation. According to equation 3.54, the partial current of zinc and nickel and the ionic strength value measured from the experiments of bath 1 and 2 are

used to calculate the kinetic parameters and A' of zinc and nickel. These parameters are then used to calculate the partial current of nickel and zinc for the bath 3.

In order to prove the effect of the ionic strength, in bath 3 condition, the partial currents of zinc and nickel are determined by Butler-Volmer equation as shown in Table 3.1, Part 3. The kinetic parameters of zinc and nickel in the Butler-Volmer equation are calculated by equation 3.54, whereas the ionic strength is determined from the experiments. The concentration of zinc used in the Butler-Volmer equation is calculated with respect to the complexing effect. As mentioned above, the summation of zinc and nickel partial current from the calculation is not exceed the total current. The ionic strength effect and the complexing effect by KCl are thus able to explain this behavior.

According to Table 3.17, the rate constant of zinc and nickel calculated by the Debye-Huckel equation is increased, in accordance with an increase of added KCl concentration. This can be explained that salt species has an effect on catalyzing rate of zinc and nickel deposition in Zn-Ni electrolyte. On the other hand, there is the complexing effect of chloride ion on zinc. Decreasing of zinc and increasing of nickel content on the deposit, shown in Table 3.18, are therefore due to the complexing effect and the ionic strength effect respectively.

3.3.5 Conclusion

According to the assumption, the complexing agent is able to form a complex with zinc ion in the solution in many forms with chloride ion, while nickel is not complexed by chloride ion. There is an increase of complexing effect to zinc with respect to increasing KCl concentration in the bath, while no effect on nickel. Decreasing of zinc content on the deposit is thus explained by the complexing effect. On the other hand, increasing nickel leads to more nickel on the deposit, and can be explained by the ionic strength of the salt species. This work is the first research studies investigating the salt effect on the growth rate of Zn-Ni alloy. It is recommended that the further study should be conducted and followed in the perspective work.

GENERAL CONCLUSION

This research devoted to the analysis of the electrochemical reactors. A multi-scale approach, from the macroscale to the microscale, was applied. At the first stage, macroscopic scale application is geared towards predicting a link between the outlet reactor and the inlet reactor, depending upon the operating conditions. This model has been developed for the recovery of a heavy metal in solution. In this case, copper was removed from an acidic solution. Experimental results have been compared with data coming from the model. It was found that theoretical data fit well with the experimental ones, especially when the device operates in mass transfer limitation. The model can use to explain experimental results and provide a predictive model, particularly for design and operation of electrical plating. In particular, this model can determine a proper time of adding species in the bath, as well as a proper time of replacing the bath. Moreover, this model could be used to design and conduct device for electrosynthesis applications.

In a second time, a development of more local approach dealing with the current distribution is performed. This work is principally experimental; nevertheless, some theoretical results performed in the research team are presented. Two kinds of cells are tested to determine the best device, resulting in characterizing electroplating baths. The first one is modified Mohler cell. This cell was designed, built and tested for copper deposition from acid bath. By positioning an insulating screen between the parallel electrodes, the electric field was distorted in such a way to produce a distribution of currents across the cathode of Mohler cell. In this cell, mass transfer is imposed by electrolyte flow parallel to the electrodes. This cell can thus be used to simulate electroplating under industrial hydrodynamic conditions, especially for modern types of industrial cells which mass transfer is imposed by circulation. Except for edge effect at the inlet and outlet of the cathode, the ratio of the maximum to minimum current densities studied was low, ranging from 1 to 2. This fact was confirmed by the results of a model simulating a primary current distribution. It could be concluded that this cell is not very useful as a bath control cell where a large range of current densities occurs. However, large area cathode allows study of the influence

of current on the deposit structure. Alternatively, a Rotating Cylinder Hull cell (RCH) has been tested using the same electrolyte. Experimental results agree well with the empirical formula and theoretical results determined for primary current distribution. In this case, the ratio of the maximum to the minimum current is equal to 7 and covers wider range than that observed from the Mohler cell. It was also shown the effect of the stirring rate. In case of low stirring rate, the secondary current distribution is obtained and the ratio between the maximum to the minimum current density will be distinctly reduced to around 2. It could be concluded that this RCH cell constitutes an appropriate reactor to bath control to elaborate and test new plating baths.

The last part of this work is devoted to analysis of the Zn-Ni alloy codeposition. The mathematical model in combination with numerical simulation is an invaluable tool for the study of alloy deposition phenomena. It allows one to study the interactions between different phenomena and to simulate the effect of critical variables. Modeling can thus contribute significantly to the advancement of the fundamental understanding of codeposition mechanisms and to a better control of alloy deposition process. A general framework for modeling charge-transfer, coupled with codeposition phenomena has been presented based on the consideration of simultaneously occurring inhibiting and catalytic interactions. The proposed approach permits the mathematical modeling of “normal” and “anomalous” codeposition phenomena in a unifying way based on one set of kinetic equations. To achieve this goal, the hypothesis should be proposed with respect to reduction of a codepositing metal. It can take place by two different approaches. On one hand, a codepositing metal can be deposited on its own and on the other nuclei substrate surface by using the substrate effect model. On the other hand, it may be reduced by a catalytic reaction, involving both metals and proceeding through an adsorbed mixed intermediate, by using the mixed species model. Reacting metal is reduced in two consecutive steps and taken into account the equilibrium potential of each codepositing metal. Depending on the relative value of the rate constants for the two reaction paths, codeposition of a given metal may be catalysed or inhibited.

The presented approach to modeling codeposition phenomena was shown to describe correctly the main features of codeposition of zinc and nickel alloy. Furthermore, theoretical models for alloy deposition available at present are generally

capable to predict the alloy compositions at different electrolyte compositions. On the other hand, the proposed approach is subject to certain limitations. First of all, the underlying reaction mechanisms are deduced from observed overall deposition behavior, but no independent confirmation of the postulated reaction intermediates is available, regarding the mixed species model. Moreover, a large number of kinetic parameters established in the substrate effect model are necessary to define.

In mathematical modeling of alloy deposition processes, it is generally concluded that using a larger number of fitting parameters can improve model accuracy, but at the expense of a loss of physical insight. On the other hand, if a model is too simple, it may become irrelevant from a practical point of view. Future work should aim towards testing the proposed approach, modeling of alloy deposition, over a wider range of experimental conditions and at the characterization of adsorbed reaction intermediates by independent methods.

REFERENCES

- 1 Greef, R. Instrumental Methods in Electrochemistry. (vol.1). New York: John Wiley & Sons, 1985.
- 2 Greef, R. Instrumental Methods in Electrochemistry. (vol.2). New York: John Wiley & Sons, 1985.
- 3 Bard, J. and Faulkner, R. Electrochemical Methods. New York: John Wiley & Sons, 1980.
- 4 Farkas, J. and Mitchell, G. D. A Novel Electrochemical Treatment Process for Heavy Metal Recovery from Wastewaters. New York: Melville, 1984.
- 5 Scott, K.; and Walsh, F. C. Chemistry and Industry. 13 (1993): 473.
- 6 Walsh, F. C. Industrial Electrochemistry 2nd ed. New York: Chapman & Hall, 1990.
- 7 Walsh, F. C.; and Robinson, D. Chemical Technology Europe 16 (May/June 1995).
- 8 Genders, J. D.; and Weinberg, N. L. Electrochemical Technology for a Cleaner Environment. Lancaster, New York: Electrosynthesis Company, 1992.
- 9 Gabe, D. R.; Walsh, F. C.; Wilcox G. D.; and Conzalez-Garcia, J. J. Applied Electrochem 28 (1998): 759.
- 10 Trinidad, P.; and Walsh, F. Int. J. Engng Ed. 14 (1998): 431.
- 11 Pickett, D. J. Electrochemical Reactor Design. Elsevier Scientific Publishing, 1979.

- 12 Gerth L.; and Lapicque, F. J. electrochem. Soc. 143 (1996): 3910-3917.
- 13 Landolt, D. Electrochim. Acta. 39 (1993): 1075.
- 14 Hull, R. O. AM Electroplat Soc. 27 (1939): 52-60.
- 15 Kadija, I.; and Abys, J. A.; Chinchankar, V.; and Straschil, H. K. Plat. and Surf. Fin. 78 (July, 1991): 60-67.
- 16 Durney, L. J. Electroplating Engineering Handbook. New York: Van nostrand Reinhold, 1984.
- 17 Lu , P. Y. Plat. and Surf. Fin. 78 (Oct., 1991): 62-65.
- 18 Yen, S. C.; and Lu, I. M. Plat. and Surf. Fin. 81 (1994): 56-59.
- 19 Madore, C.; Matlosz, M.; and Landolt, D. J. Appl. Electrochem. 22 (1992) :1155.
- 20 Lacourcelle, L. Information à L'usage du Concepteur. fiche 24. Paris: Librairie du traitement de surface, 1997.
- 21 Faust, E. Stage Recherche. Toulouse : INP, July 2001.
- 22 Dupuy, F.; Vergnes, H.; Fenouillet, B.; and Duverneuil, P. ECCE 4th European congress of chemical engineering. Granada Spain (Sep 2003) : 21-25.
- 23 Dupuy, F.; Vergnes, H.; Fenouillet, B.; and Duverneuil, P. Saint-Nazaire (Sep 2003): 9-11
- 24 Madore, C.; and Landolt, D. Plat. and Surf. Fin. 80 (1993): 73-78.

- 25 Madore, C.; West, A. C.; Matlosz, M.; and Landolt, C. Electrochim. Acta 37 (1991): 69-74.
- 26 Ibl, N. Comprehensive Treatise of Electrochemistry. (Edited by E. Yeager). Vol. 6. New York: Plenum Press, 1983.
- 27 Brenner, A. Electrodeposition of alloys. Vol. 1&2. New York: Academic Press, 1963.
- 28 Hall, D. E. Plating Surf. Finish. 71 (1983): 59.
- 29 Gorbunova, M.; and Polukarov, Yu. M. in Delahay, P.; and Tobias, C. W. (Eds.) Advances in Electrochemistry and Electrochemical Engineering. Vol.5. New York: Wiley-Interscience, 1996.
- 30 Ramachar, T. L. Electroplat. 1 (1959): 165.
- 31 Swathirajan, S. J. Electroanal. Chem. 221 (1987): 211.
- 32 Crotty, D. Met. Finish. 94 (1996): 54.
- 33 Bruet-Hotellaz; Bonino, J.P.; and Rousset, A. J. Mat. Sc. 34 (1999): 881-886.
- 34 Bories, C.; Bonino, J.P.; and Rousset, A. J. Appl. Electrochem. 29 (1999): 1045 -1051.
- 35 Fabri Miranda, F. J.; Barcia, O.E.; Mattos, O.R.; and Wiart, R. J. Electrochem. Soc. 144 (1997): 3441.
- 36 Pouderoux, P; Bonino, J.P.; Rousset, A. Proceeding of the Surface Finishing International Congress “ Interfinish 92”, SAOPAULO (1992): 451-463.
- 37 Tsuda, T. and Kuremoto, T. U.S.patent 4-249-999 (1981).

- 38 Zaki, N. Metal Fin. 87(6) (1989): 57-60.
- 39 Kalantary, M. R. Plating Surf. Finish. 71 (1994): 80-88.
- 40 Verberne, W.W.J.C. Proc. 60th Int'l Conf. On Surf. Fin. Telford, UK (Sept., 1992) : 158-169.
- 41 Barcelo, G.; Garci, J.; Muller, C.; and Pregonas, J. Metal Finish. 90 (1992): 1249.
- 42 Elkhatabi, F.; Barcelo, G.; Sarret, M.; and Muller, C. J. Electroanal. Chem. 419 (1996): 71-76.
- 43 Benballa, M.; Nils, L.; Sarret, M.; and Muller, C. Surf. Coat. Technol. 123 (2000): 55.
- 44 Fukushima, H.; Akiyama, T.; Higashi, K.; Kammel. R.; and Karimkhani, M. Metall. 42 (1988): 242.
- 45 Fratesi, R.; and Roventi, G. J. Appl. Electrochem. Soc. 112 (1965): 657.
- 46 Roventi, G.; Fratesi, R.; Guardia, R. A. D.; and Barucca, G. J. Appl. Electrochem. 30 (2000): 173.
- 47 Mathias, M. F.; and Chapman, T.W. J. Electrochem. Soc. 134 (1987):1408.
- 48 Chassaing, E.; Quang, K. Vu. ; and Wuart, R. J. Appl. Electrochem. 19 (1989):893.
- 49 Lin, Y. P.; and Robert Selman, J. J. Electrochem. Soc. 140 (1993):1304.
- 50 Dahms, H.; and Croll, J. M. J. Appl. Electrochem. 122 (1965): 771.

- 51 Hessami, S.; and Tobias, C. W. J. Electrochem. Soc. 136 (1989): 3611.
- 52 Gangasingh, D.; and Talbot, J. B. J. Electrochem. Soc. 138 (1994): 3605.
- 53 Grande, W.; and Talbot, J. B. J. Electrochem. Soc. 140 (1993): 675.
- 54 Sasaki, K.; and Talbot, J. B. J. Electrochem. Soc. 142 (1995): 775.
- 55 Matlosz, M. J. Electrochem. Soc. 140 (1993): 2272.
- 56 J. Horkans, J. Electrochem. Soc. 126 (1979) 1861.
- 57 Andricacos, P.; Arana, C.; Tabib, J.; Dukovic, J. and Romankiw, L. T. J. Electrochem. Soc. 136 (1989): 1989.
- 58 Gangasingh, D.; and Talbot, J. B. J. Electrochem. Soc. 138 (1994): 3605.
- 59 Zech, N.; Podlaha E. J.; and Landolt, D. J. Electrochem. Soc. 146 (1999): 2892.
- 60 Chassang, E.; and Wiart, R. Electrochimica. Acta. 37 (1992): 545.
- 61 Arkam, C.; Bouet, V.; Gabrielli, C.; Maurin, G.; and Perrot, H. J. Electrochem. Soc. 141 (1994): L103.
- 62 Huss, A.; Lim, P. K.; and Eckert, C. A. J. Phys. Chem. 86 (1982): 4224.
- 63 Martin, L.R. ; and Hill, M.V. Atm. Env. 21 (1987a): 1487.
- 64 Berglund, J.; and Elding, L. I. Atm. Env. 29 (1993): 1379.
- 65 Brandt, C.; and Van Eldik, R. Chemical Reviews. 95 (1995): 119.

- 66 Grgic, I.; Dovzan, A.; Bercic, G.; and Hudnik, V. J. J. Phys. Chem. 29 (1998): 315.
- 67 Robinson, R. A.; and Stokes, R. H. Electrolyte Solution. London: Butterworth, 1959.



สถาบันวิทยบริการ
จุฬาลงกรณ์มหาวิทยาลัย

BIOGRAPHY

Ms. Manida Teeratananon was born in 1976 in Udorn Thani, Thailand. She obtained diploma degree in analytical chemistry from Institute of Analytical Training School, Faculty of Science, Chulalongkorn University in 1997 and Bachelor degree in Chemical Engineering from Department of Chemical Technology, Faculty of Science, Chulalongkorn University in 2000. With the assistance of Thailand Research Fund and the French embassy of Thailand for the research financial support, she has continued studying Doctor degree at the same Department in 2000. She took her research works at ENSIACET, INP Toulouse, France in 2002 -2004.

The conference and publication involving her research works are the following

Teeratananon, M.; Pruksathorn, K.; Damronglerd, S.; Dupuy, F.; Hugues, V; Fenouillet, B.; and Duverneuil, P. Experimental investigation on the mechanism of zinc-nickel alloys electrodeposition. ASCON FBR 2004. Taipei, Taiwan, Nov. 21 – 24, 2004.

Teeratananon, M.; Saidi, K.; Fenouillet, B.; and Vergnes, H. Etude des depots d 'alliage nickel/zinc, Journees d' electrochimic. Poitiers, France, June 2003.

Teeratananon, M.; Damronglerd, S.; Pruksathorn, K.; Duverneuil, P.; and Hugues, V; Effect of applied current on kinetic and mass transport in an electrochemical batch reactor. 9 th APPChE Congress and CHEMECA 2002. Christchurch, New Zealand, Sep. 29 – Oct. 3, 2002.

Teeratananon, M.; Pruksathorn, K.; Damronglerd, S.; Dupuy, F.; Hugues, V; Fenouillet, B.; and Duverneuil, P. Experimental investigation of the current distribution in Mohler cell and Rotating Cylinder Hull cell, Science Asia (in print).

At present, 2004, she is working as a reliability engineer, in Tribology section, Western Digital BangPa-In (Thailand).